NAT'L INST. OF STAND & TECH R.I.C.
A11103 431446

NIST
PUBLICATIONS

UNITED STATES
DEPARTMENT OF COMMERCE
NATIONAL INSTITUTE OF STANDARDS
AND TECHNOLOGY

NIST Technical Note 1342

Measurement and Evaluation of a TEM / Reverberating Chamber

Myron L. Crawford
Mark T. Ma
John M. Ladbury
Bill F. Riddle

QC
100
.U5753
#1342
1990
C.2

NATIONAL INSTITUTE OF STANDARDS &
TECHNOLOGY
Research Information Center
Gaithersburg, MD 20899

DATE DUE

Demco, Inc. 38-293

NIST
QC100
.U5753
#1342
1990
c.2

Measurement and Evaluation of a TEM / Reverberating Chamber

Myron L. Crawford
Mark T. Ma
John M. Ladbury
Bill F. Riddle

Electromagnetic Fields Division
Center for Electronics and Electrical Engineering
National Engineering Laboratory
National Institute of Standards and Technology
Boulder, Colorado 80303-3328

Prepared for
Electromagnetic Environmental Effects Division
U.S. Army Electronic Proving Ground
Fort Huachuca, Arizona 85613-7110

U.S. DEPARTMENT OF COMMERCE, Robert A. Mosbacher, Secretary
NATIONAL INSTITUTE OF STANDARDS AND TECHNOLOGY, John W. Lyons, Director
Issued July 1990

National Institute of Standards and Technology Technical Note 1342
Natl. Inst. Stand. Technol., Tech. Note 1342, 116 pages (July 1990)
CODEN:NTNOEF

U.S. GOVERNMENT PRINTING OFFICE
WASHINGTON: 1990

For sale by the Superintendent of Documents, U.S. Government Printing Office, Washington, DC 20402-9325

CONTENTS

	Page
List of Figures and Tables	v
Abstract	1
1. Introduction and Background	1
2. Anticipated Advantages and Limitations	3
3. Chamber Design and Theoretical Considerations	4
3.1 General Considerations	4
3.2 USAEPG 1/10 Scaled TEM/Reverberating Chamber	6
3.3 Proposed Full-Size TEM/Reverberating Chamber	7
4. CW Evaluation of the 1/10 Scaled TEM/Reverberating Chamber	8
4.1 Measurement Approaches	8
4.1.1 TEM Mode	8
4.1.2 Reverberating Mode	8
4.2 NIST CW Evaluation System	9
4.3 CW Evaluation and Calibration Results	10
4.3.1 TEM Line and Antenna VSWR and Chamber Coupling Efficiency	10
4.3.2 Chamber Quality Factor	11
4.3.3 E-Field Amplitude Calibration	11
4.3.4 Effects of RF Absorber Loading and Multiple Driven Plates	13
4.3.5 Tuner Effectiveness	14
4.3.6 Test Zone E-field Uniformity	15
4.3.7 Test Results from 20 GHz to 40 GHz	16
4.3.8 Summary of CW Calibration and Evaluation Results	17
5. Pulsed RF/Time Domain Evaluation of the 1/10 Scaled TEM/Reverberating Chamber	18
5.1 Background	18
5.2 NIST Pulsed RF Evaluation System	18
5.3 Pulsed RF Evaluation Results	19
5.4 Comments on Pulsed RF Measurement Results	20
6. Projecting the 1/10 Scaled Chamber CW and Pulsed RF Measurement Results to a Full-Scale TEM/Reverberating Chamber	21
7. Performing EMC/V Measurements Using the TEM/Reverberating Chamber	22
7.1 Performing EMC/V Measurements Using Manual Operations	22
7.2 Automated EMC/V Measurements	25

CONTENTS (cont.)

7.2.1 TEM Mode Measurement Procedure ---------- 25
7.2.2 Reverberating Mode-Tuned Measurement Procedure ------- 25
7.2.3 Reverberating Mode-Stirred Measurement Procedure ----- 26
7.2.4 Comparison of TEM/Reverberating Chamber Measurement Results with Anechoic Chamber Tests - Some Examples -- 27

8. Summary and Conclusions ---------- 28

9. Acknowledgments ---------- 30

10. References ---------- 30

List of Figures and Tables

Figure 3.1 Cross sectional sketches of the USAEPG 1/10 scaled TEM/reverberating chamber ---------- 33

Figure 3.2 Photographs of the USAEPG 1/10 scaled TEM/reverberating chamber ---------- 34

Figure 3.3 Theoretical mode distribution for the 1/10 scaled TEM/reverberating chamber (1.31 m x 2.41 m x 3.87 m) ----- 35

Figure 3.4 Cross section view of a TEM cell for determining the field distribution ---------- 36

Figure 3.5 Cross sectional sketches of a proposed full scale TEM/ reverberating chamber (13.1 m x 24.1 m x 38.7 m) --------- 37

Figure 3.6 Theoretical mode distribution for the proposed full scale TEM/reverberating chamber (13.1 m x 24.1 m x 38.7 m) ----- 38

Figure 3.7 Theoretical mode distribution for a large TEM/reverberating chamber (16.2 m x 34.4 m x 38.7 m) ---------- 39

Figure 3.8 Theoretical quality factor of proposed full scale TEM/ reverberating chamber (13.1 m x 24.1 m x 38.7 m) assuming: (a) galvanized (zinc) steel and (b) enamel painted (cold rolled) steel ---------- 40

Table 3.1 Comparison of test fields in a galvanized (zinc finish) steel reverberating chamber of 3.7 m x 5.2 m x 9.8 m with that in an anechoic chamber at 3 m separation distance for same transmitted power. Test volume definition in anechoic chamber is (± 3 dB) ---------- 41

Table 3.2 Comparison of test fields in a galvanized steel reverberating chamber with that in an anechoic chamber for same transmitted power. Separation distances in anechoic chamber = 1 and 3 m ---------- 42

Table 3.3 Test volume for radiated fields in anechoic chamber at 1 m and 3 m separation distances with selected transmitting antenna gain. Test volume definition is based on half-power points of the radiation pattern ---------- 43

Table 3.4 Theoretical mode calculations of frequency and gap between adjoining modes for 1/10 scaled TEM/reverberating chamber, a = 1.31 m, b = 2.41 m, and d = 3.87 m ---------- 44

Table 3.5 Normalized electric-field components in the 1/10 scaled TEM cell with 100 Ω characteristic impedance, (a) back plate and (b) side plate ---------- 45

Table 3.6 Relative permeability of cold rolled 11 gauge steel to be used in construction of welded shielded enclosures as a function of frequency ---------- 46

Figure 4.1 Block diagram of the instrumentation used in the cw evaluation of the USAEPG 1/10 scaled TEM/reverberating chamber ---------- 47

Figure 4.2 Photograph of the NIST equipment used to evaluate the USAEPG 1/10 scaled TEM/reverberating chamber ---------- 48

Figure 4.3 Measured VSWR of (a) top plate, (b) back plate, and (c) side plate TEM line, from 1 to 2000 MHz, transmitting into the 1/10 scaled TEM/reverberating chamber ---------- 49

Figure 4.4 Measured composite VSWR of the top plate (0.03 to 1.0 GHz) line and the broadband horn antenna (1.0 to 18 GHz) transmitting into the 1/10 scaled TEM/ reverberating chamber ---------- 50

Figure 4.5 Measured coupling efficiency between the top plate line transmitting) and log periodic antenna (receiving, 0.1 to 1.0 GHz), and the broadband horn antennas (transmitting and receiving, 1.0 to 18 GHz) in the 1/10 scaled TEM/reverberating chamber ---------- 51

Figure 4.6 (a) Theoretical and experimental Q of the USAEPG 1/10 scaled chamber and (b) ratio of theoretical to experimental Q, 0.2 to 18 GHz ---------- 52

Figure 4.7 E-field components measured at the center of the 1/10 scaled chamber using a NIST isotropic (5 cm dipole) probe (position #3 in figure 4.14) with chamber excited by: (a) top plate, (b) back plate, and (c) side plate. Net input power is 1 W ---------- 53

Figure 4.8 Maximum and average E-field in the 1/10 scaled chamber measured with (a) calibrated 1 cm dipole probe (0.03 to 18 GHz), and (b) log-periodic receiving antenna (0.1 to 1 GHz) and broadband horn receiving antenna (1 to 18 GHz). Net transmitted power is 1 W ---------- 54

Figure 4.9 Input power required to generate a 20 V/m maximum E-field at the center of the 1/10 scaled chamber using: (a) back plate (Hor. Pol.), (b) top plate (Vert. Pol.), and (c) log periodic and broadband horn ---------- 55

Figure 4.10 Cross sectional sketches of the USAEPG 1/10 scaled TEM/reverberating chamber showing placement of 15 pieces 0.2 m x 0.6 m x 0.6 m rf absorber ---------- 56

Figure 4.11 E-field components measured at the center of the 1/10 scaled chamber using a NIST 5 cm dipole, isotropic, probe with the chamber excited by: (a) top plate, no absorber; (b) top plate, absorber loaded; (c) back plate, no absorber; (d) back plate, absorber loaded; (e) side plate, no absorber; (f) side plate, absorber loaded; (g) back and side plates driven simultaneously in phase, no absorber; and (h) all three plates driven simultaneously in phase, no absorber ---------- 57

Figure 4.12 E-fields calculated from receiving antenna power measurements in the 1/10 scaled chamber with 1 W net input power. Same transmitting and receiving antennas used as in figure 4.8 ---------- 59

Figure 4.13 Measured tuner effectiveness in the 1/10 scaled chamber using: (a) receiving antenna power measurements (same receiving antennas as figure 4.5), and (b) 1 cm dipole probe E-field measurements ---------- 60

Figure 4.14 Cross sectional sketch of the USAEPG 1/10 scaled TEM/reverberating chamber showing placement of isotropic probes for measuring spatial E-field uniformity --------- 61

Figure 4.15 Spatial distribution of the E-field components in the 1/10 scaled chamber measured with 7 NIST isotropic probes (5 cm dipoles) when transmitting 1 W net input power from top plate: (a) maximum and (b) average values 62

Figure 4.16 Smoothed average and maximum of measured E-field components in the 1/10 scaled chamber generated by the top plate with 1 W net input power, determined from data in figure 4.15 ---------- 64

Figure 4.17 Spatial distribution of E-field components in the 1/10 scaled chamber measurh 7 NIST isotropic probes (5 cm dipoles) when transmitting 1 W net input power from back plate: (a) maximum and (b) average values ----- 65

Figure 4.18 Smoothed average and maximum of measured E-field components in the 1/10 scaled chamber generated by the back plate with 1 W net input power, determined from data in figure 4.17 ---------- 67

Figure 4.19 Spatial distribution of E-field components in the 1/10 scaled chamber measured with 7 NIST isotropic probes (5 cm dipoles) when transmitting 1 W net input power from side plate: (a) maximum and (b) average values ----- 68

Figure 4.20 Smoothed average and maximum of measured E-field components in the 1/10 scaled chamber generated by the side plate with 1 W net input power, determined from data in figure 4.19 ---------- 70

Figure 4.21 Measured coupling efficiency (minimum loss) of the horn antennas (transmitting/receiving) placed inside the 1/10 scaled chamber at 20 to 40 GHz ---------- 71

Figure 4.22 Maximum E-fields in the 1/10 scaled chamber determined from power measurements of the receiving antenna, 20 to 40 GHz, with a net input power of 1 W ---------- 72

Figure 4.23 Calculated normalized propagation attenuation in air for 5 humidities ---------- 73

Table 4.1 Spatial variations in E-fields measured inside the 1/10 scaled TEM/reverberating chamber over test volume defined by probes shown in figure 4.14 ---------- 74

Table 4.2 Summary of operation characteristics of 1/10 scaled TEM/reverberating chamber ---------- 75

Figure 5.1 Block diagram of instrumentation used in pulsed rf evaluation of the 1/10 scaled TEM/reverberating chamber 76

Figure 5.2 Maximum values of transmitted (positive) and received (negative) rf pulse waveforms in the 1/10 scaled TEM/ reverberating chamber determined with increasing amounts of rf absorber loading at 0.9 GHz ---------- 77

Figure 5.3 Maximum values of transmitted and received rf pulse waveforms inside empty (no absorber) 1/10 scaled TEM/ reverberating chamber determined at selected frequencies. Rf input pulse width is 5 μs, duty cycle is 0.001 ------- 78

Figure 5.4 Maximum values of transmitted and received rf pulse waveforms inside 1/10 scaled TEM/reverberating chamber determined with: (a) no absorber, and (b) 1 piece of 20.3 cm X 61 cm X 61 cm (8" x 24" x 24") rf absorber at selected frequencies ---------- 79

Figure 5.5 Maximum and average values of received rf pulse waveforms inside the 1/10 scaled TEM/reverberating chamber determined by mode-tuned approach. Chamber empty (no absorber). Measurements were taken at 10 selected frequencies and 3 pulse widths ---------- 82

Figure 5.6 Time required for rf signal transmitted into the 1/10 scaled TEM/reverberating chamber to rise 63% of steady-state amplitude using: (a) no absorber, and (b) 1 piece of 20.3 cm X 61 cm X 61 cm rf absorber ---------- 86

Figure 5.7 Time required for rf signal transmitted into the 1/10 scaled TEM/reverberating chamber to rise 90% of steady-state amplitude using: (a) no absorber, and (b) 1 piece of 20.3 cm X 61 cm X 61 cm rf absorber ---------- 87

Figure 5.8 Estimated correction factors for amplitude response of rf test pulses in the 1/10 scaled TEM/reverberating chamber at selected frequencies as a function of input pulse width using: (a) no absorber, and (b) 1 piece of 20.3 cm X 61 cm X 61 cm rf absorber ---------- 88

Figure 5.9 Estimated correction factors for amplitude response of rf test pulses in the 1/10 scaled TEM/reverberating chamber at selected input pulse widths as a function of frequency using (a) no absorber, and (b) 1 piece of 20.3 cm X 61 cm X 61 cm rf absorber ---------- 90

Table 5.1 Summary of influences of rf absorber loading on loss, quality factor, and charge/decay time of the 1/10 scaled TEM/reverberating chamber at 0.9 GHz ---------- 91

Table 5.2 Comparison of measured and calculated charge/decay time of the 1/10 scaled TEM/reverberating chamber, determined from chamber average loss measurements (figure 4.5) and from data shown in figure 5.5 ---------- 92

Figure 6.1 Projected coupling efficiency (minimum loss) of 13.1 m x 24.1 m x 38.7 m TEM/reverberating chamber ---------- 93

Figure 6.2 Projected E-fields in 13.1 m X 24.1 m X 38.7 m TEM/reverberating chamber for 200 W input power determined from (a) projected chamber losses and Q factors, and (b) measurements made in RADC chamber and NSWC chamber -- 94

Figure 6.3 Projected charge time for 13.1 m X 24.1 m X 38.7 m TEM/reverberating chamber ---------- 95

Table 6.1 Summary/conclusions - 3 regions of operation - 13.1 m x 24.1 m x 38.7 m TEM/reverberating chamber (zinc coated) ---------- 96

Figure 7.1 Block diagram of swept frequency EM radiated immunity and shielding effectiveness measurement system using TEM/reverberating chamber ---------- 97

Figure 7.2 Block diagram of swept frequency EM radiated emissions and shielding effectiveness system using TEM/reverberating chamber ---------- 98

Figure 7.3 Measured SE data of 3 cm X 6 cm TEM cell with 15 mm circular aperture using 1/10 scaled TEM/reverberating chamber and swept frequency measurement system ---------- 99

Figure 7.4 Block diagram of automated susceptibility measurement system using the TEM/reverberating chamber in the TEM mode of operation ---------- 100

Figure 7.5 Block diagram of automated radiated susceptibility measurement system using the TEM/reverberating chamber in the transition and the reverberating modes of operation ---------- 101

Figure 7.6 Maximum responses of NIST 1 cm dipole probe to an E-field of 37 dBV/m generated in (a) the 1/10 scaled TEM/reverberating chamber, (b) NIST 2.74 m X 3.05 m X 4.57 m reverberating chamber, and (c) NIST 4.9 m X 6.7 m X 8.5 m anechoic chamber ---------- 102

Figure 7.7 Maximum powers received by a broadband (1 to 18 GHz) horn antenna in an E-field of 37 dBV/m using: (a) 1/10 scaled TEM/reverberating chamber, and (b) NIST anechoic chamber ---------- 103

Figure 7.8 Comparison of broadband horn antenna response in 1/10 scaled TEM/reverberating chamber with its response minus free-space gain measured in the NIST anechoic chamber ---------- 104

Figure 7.9 Comparison of SE of 3 cm X 6 cm TEM cell with 15 mm circular aperture: (a) theoretical calculations, (b) measured in RADC chamber, (c) measured in 1/10 scaled chamber with mode-tuned approach, and (d) measured in 1/10 scaled chamber with mode-stirred approach ---------- 104

MEASUREMENT AND EVALUATION OF A TEM/REVERBERATING CHAMBER

Myron L. Crawford
Mark T. Ma
John M. Ladbury
Bill F. Riddle

Electromagnetic Fields Division
National Institute of Standards and Technology
Boulder, CO 80303

This report summarizes the measurement and evaluation of a 1/10 scaled model TEM/reverberating chamber developed as a single, integrated facility for testing radiated electromagnetic compatibility / vulnerability (EMC/V) of large systems over the frequency range, 10 kHz to 40 GHz. The facility consists of a large shielded enclosure configured as a transverse electromagnetic (TEM), transmission line-driven, reverberating chamber. TEM mode test fields are generated at frequencies below multimode cutoff, and mode-stirred test fields are generated at frequencies above multimode cutoff. Both the chamber's cw and pulsed rf characteristics are measured and analyzed. The report also discusses the basis for such a development including the theoretical concepts, the advantages and limitations, the experimental approach for evaluating the operational parameters, and the procedures for using the chamber to perform EMC/V measurements. A full-scale chamber that will provide a test volume of 8 m x 16 m x 30 m is proposed. Some projections of the full-scale chamber's estimated characteristics and operational parameters are also given.

Key words: cw and pulsed rf testing; radiated EM compatability and vulnerability measurements; reverberating chamber; TEM cell

1. Introduction and Background

The ability to simulate an operating environment for accurately measuring the performance of electronic equipment is fundamental to ensuring the electromagnetic compatibility (EMC) of the equipment. In recent years, the Fields and Interference Metrology Group of the National Institute of Standards and Technology (NIST) in Boulder, CO, has been developing improved methods and facilities for EMC testing. Two such facilities are the transverse electromagnetic (TEM) cell and the reverberating (mode-stirred) chamber. Each has its advantages and limitations.

The TEM cell [1,2] is an expanded 50 Ω rectangular coaxial transmission line, with tapered sections at both ends, that operates ideally with only the TEM mode to generate the equivalent of a planar field. The cell's use is limited to frequencies below a few hundred megahertz, depending upon the size of the equipment under test (EUT) and hence the size of the cell. This

limitation is due to the requirement that only the fundamental TEM mode exist in the cell at frequencies for which tests are to be made.

The reverberating chamber [3,4,5,6] is a shielded room with one or more rotating stirrers to mix the fields transmitted from an antenna placed inside the chamber. The generated test field is determined statistically (maximum and average values) from the multimoded, complex fields. This technique has significant advantages for testing large EUTs efficiently and cost effectively. However, the method is restricted to frequencies above a few hundred megahertz, again depending upon the size of the test chamber. This limitation is a consequence of requiring the chamber to be electrically large enough that modes exist inside the chamber for adequate mode mixing and spatial averaging to ensure that relatively uniform fields will be generated for testing.

Combining these two measurement techniques into a single facility will allow EMC testing over the combined frequency range of the TEM cell and the mode-stirred chamber. This would result in significant cost and time savings with a possible improvement in measurement accuracy in performing essential EMC tests. A combined TEM/reverberating chamber will have three distinct regions of operation: (a) TEM, (b) transition, and (c) reverberating. The TEM region will cover the low frequency range near dc to the first multimode cutoff frequency. The transition region covers the range above the first multimode frequency, up through the frequencies for which the first few higher modes are excited in the chamber, but insufficient in number to provide adequate spatial averaging. The test field will be a combination of the TEM mode and a limited number of higher order modes that yield a complex field that is rather difficult to define both in polarization and amplitude. Techniques such as absorber loading to suppress the quality factors of the higher order modes, and/or field averaging over the volume using a matrix of isotropic E-field probes must be used to define the test field parameters. The reverberating region of operation will cover the higher frequency range for which sufficient modes exist to ensure adequate mode mixing and spatial averaging. This test field simulates a complex, real-world field environment.

This report summarizes the measurement and evaluation results of a particular chamber designed to determine how well a combined ("hybrid") TEM/reverberating chamber could be used to operate as a radiated EMC/V test facility. The chamber has the dimension of 1.31 m x 2.41 m x 3.87 m, which represents a 1/10 scaled model of the future full-size facility (13.1 m x 24.1 m x 38.7 m). Both the cw and pulsed rf characteristics of this chamber were evaluated. Anticipated advantages and limitations of this combined chamber are outlined in Section 2. A description of the chamber itself is given in section 3. Section 4 describes the system used for performing the continuous wave (cw) evaluation/calibration of the chamber and presents the results obtained. Section 5 describes the pulsed rf, time-domain evaluation systems and the associated measurement results. Section 6 provides some projections, based on the results contained in Sections 4 and 5 for the scaled chamber, of the characteristics for the large, full-scale TEM/reverberating chamber. Section 7 outlines the measurement procedures for performing EM susceptibility and shielding effectiveness tests with this chamber by both manual and automated operations. This section also gives sample results obtained using control standard EUTs for comparison with data

obtained in an anechoic chamber and other reverberating chambers to show correlation factors. Finally, Section 8 gives a summary and some conclusions derived from this study and from previous work in developing the TEM cell and reverberating chamber measurement techniques.

2. Anticipated Advantages and Limitations

Motivation for developing a TEM/reverberating chamber arises from its potential for realizing a number of significant advantages. These include:

a. Electrical isolation from the environment;

b. Accessibility (indoor test facility);

c. The ability to generate high test fields over a large volume efficiently. For example, 1 W of rf power applied to the transmitting antenna inside this 1/10 scaled chamber, operating in the reverberating mode at 10 GHz, generates approximately 100 V/m maximum test E-field;

d. Broad frequency coverage (10 kHz $\geq$ 40 GHz);

e. Cost effectiveness. The cost of a TEM/reverberating chamber is estimated to be less than half that of an equivalent anechoic chamber, primarily due to the cost of rf absorbers and fire-protection system costs associated with an anechoic chamber. Also, rf source power requirements are significantly less for a TEM/reverberating chamber than for an anechoic chamber as indicated in section 4. Test time for using the hybrid chamber is anticipated to be approximately 1/5 of that required when using an anechoic chamber to characterize the maximum response of an EUT;

f. Reciprocity (the TEM/reverberating chamber can be used for both immunity and EMI/TEMPEST emission testing);

g. No rotation of the EUT. This results from the three separate orthogonal plates designed for TEM mode operation and the inherent test field characteristics of the chamber operating in the reverberating mode;

h. Physical security, since the chamber is an enclosed facility; and

i. The potential broad application for cw and pulsed rf testing.

There are also disadvantages or limitations when using such a hybrid chamber. Some of these are:

a. Loss of directional or polarization characteristics of the EUT placed inside the chamber when operating in the reverberating mode;

b. Limitations of the test field to planar fields at lower frequencies (TEM mode of operation), and to complex multimode fields at higher frequencies (reverberating mode of operation);

c. Measurement of only the total power radiated from the EUT in the reverberating mode of operation as opposed to determining both the total power radiated and the directional characteristics of the emissions for TEM mode of operation;

d. Less response of an EUT measured in the reverberating mode than when measured inside an anechoic chamber (free-space), if the EUT is exposed to the same level of test field in each chamber. This reduction in response is proportional to the EUT's free-space directivity [5]. Hence, the susceptibility criteria determined for an EUT measured in a TEM/reverberating chamber operating in the reverberating mode must include an additional factor proportional to the EUT's estimated free-space maximum gain, if the results are to be correlated to the worst case free-space conditions; and

e. Relatively large measurement uncertainty (as great as ± 10 dB) for establishing the test field in the frequency range of the transition region between TEM mode of operation and reverberating mode of operation of the chamber.

3. Chamber Design and Theoretical Considerations

3.1 General Considerations

Factors which influence the chamber's electrical and operational characteristics include: (a) the size and materials used in the chamber's construction, (b) the characteristic impedance of the transmission lines used for TEM mode operation of the chamber, and (c) EUT's mechanical and electrical operational requirements.

The size, shape, and materials used in the chamber determine the test volume, quality factor, and the shielding effectiveness characteristics of the chamber. The size and shape also influence the frequency distribution, number of modes, and density of the modes that are excited inside the chamber. At low frequencies, only the fundamental or TEM mode can exist in the chamber. As the frequency increases, higher order modes may begin to propagate. The resonant frequencies of these modes can be determined by

$$f_{\ell np} = 150 \sqrt{(\ell/a)^2 + (n/b)^2 + (p/d)^2} , \qquad (1)$$

where ℓ, n, and p are integers, and $f_{\ell np}$ is in megahertz when the rectangular chamber's internal dimensions a, b, and d are expressed in meters. By carefully selecting the chamber dimensions, we can minimize redundant modes (modes occurring at the same frequency), resulting in a better mode distribution.

The quality factor of the resonant modes in the chamber determines the input power requirements for establishing test fields when the chamber is operated in the reverberating mode. The theoretical composite quality factor of a reverberating chamber is approximately [7, 8],

$$\tilde{Q} = \frac{3}{2}\,\frac{V}{S\delta_s\mu_r}\,\frac{1}{1+\frac{3\lambda}{16}\left(\frac{1}{a}+\frac{1}{b}+\frac{1}{d}\right)}\,, \qquad (2)$$

where V is the chamber's volume in m^3, S is the internal surface area in m^2, $\delta_s = \sqrt{2/(\omega\mu\sigma)}$ is the skin depth of the chamber wall in m, σ is the wall conductivity in S/m, $\mu = \mu_o\mu_r$ is the wall permeability in H/m, $\mu_o = 4\pi(10)^{-7}$ H/m is the free-space permeability, μ_r is the relative permeability, and λ is the wavelength in m. This composite $\tilde{Q}$ is determined by averaging the Q values of all possible modes within a small frequency interval around the frequency of interest [7]. The composite $\tilde{Q}$ estimated from (2) is considered an upper bound because it does not take into account losses other than that due to wall conductivity. In reality, other losses will also occur during the measurement, for example, due to leakage from the chamber, antenna support structures, and the chamber's wall coatings. An alternative means of determining the chamber's Q is also available by measuring the chamber's loss [9]. Chamber loss is determined experimentally by measuring the difference between the net input power, P_t, delivered to the chamber's transmitting antenna or transmission lines and the power available, P_r, at a reference antenna or an EUT. Both P_t and P_r are measured in the same units (W or mW).

If the energy were uniformly distributed over the volume of the chamber, an empirical value of the chamber's quality factor (Q') could be obtained using the following equation [9],

$$Q' \approx 16\,\pi^2\,\frac{V}{\lambda^3}\,\frac{P_r}{P_t}\,, \qquad (3)$$

where V and λ are as previously defined.

If a chamber factor, $K = \tilde{Q}/Q'$, is determined, the "equivalent" power density, P_d', in a reverberating chamber may be determined by: [5],

$$P_d' = \frac{4\pi P_r}{\lambda^2} \quad W/m^2\,. \qquad (4)$$

With the aid of (3), we can relate P_d' to the net input power, P_t, by

$$P_d' \approx \frac{3\lambda P_t}{8\pi\, KS\delta_s\,\mu_r} \quad W/m^2. \qquad (5)$$

As can be seen from (5), the material used in constructing the chamber as well as the chamber's dimensions influence the input power requirements for establishing a specified test field in the chamber. Typical K factors for reverberating chambers are in the range of 2 to 5.

Obviously, the electrical properties of the materials also influence the shielding characteristics of the chamber. Since the chamber is anticipated for use at frequencies as low as 10 kHz, steel with a relatively high permeability may be required to obtain adequate shielding from magnetic fields. If such metal is used, it may be advisable to treat it with zinc (i.e., galvanize it) or line the chamber with a metal such as aluminum or copper to improve the surface conductivity and hence the chamber's quality factor.

It is of interest to compare the power densities of test fields anticipated inside a reverberating chamber with that anticipated inside an anechoic chamber assuming the same available input power. The power density, P_d, generated inside an anechoic chamber, assuming far-field conditions, can be determined by

$$P_d = \frac{P_t G}{4\pi r^2} \quad W/m^2, \tag{6}$$

where G is the free-space, far-field gain of the transmitting antenna and r is the separation distance between the antenna and the test location in m. A comparison of the test fields given as the ratio, P_d'/P_d, obtained from (5) and (6) for a comparable size, zinc-finish, reverberating chamber of 3.7 m x 5.2 m x 9.8 m and an anechoic chamber is given in Table 3.1 at frequencies from 100 MHz to 500 MHz when the tuned dipoles are used. The table also gives the size of the test volume that falls within ± 3 dB region in the anechoic chamber at r = 3 m. The ratios, P_d'/P_d, for r = 1 m and 3 m obtained using open-ended waveguide and horn transmitting antennas in an anechoic chamber, at frequencies from 0.2 to 18 GHz, are given in Table 3.2. The test volume definitions for the radiated fields in the anechoic chamber as a function of antenna gain at 1 m and 3 m separation distances are given in Table 3.3. These tables demonstrate that significantly less power is required to generate the same maximum amplitude test fields in a reverberating chamber over large volumes than it is generated in an anechoic chamber over comparable volumes.

3.2 USAEPG 1/10 Scaled TEM/Reverberating Chamber

The 1/10 scaled chamber is the model of a proposed large TEM/reverberating chamber anticipated to be built at the USAEPG, Ft. Huachuca, AZ. It is a rectangular shielded enclosure, 1.31 m x 2.41 m x 3.87 m (4.3 ft x 7.9 ft x 12.7 ft) in size, constructed from sheet steel welded together at the edges. The interior finish is of flame-sprayed zinc. Cross-sectional drawings of the 1/10 scaled chamber are shown in figure 3.1. Photographs showing different views are shown in figure 3.2. Calculated resonant-mode frequencies for this scaled chamber using (1) are given in table 3.4. The theoretical mode distribution obtained from these data is shown in figure 3.3 in terms of the percentage frequency interval (gap) between adjoining modes as a function of frequency.

Three orthogonal plates are mounted in the chamber, each designed to operate as a 100 Ω characteristic impedance TEM transmission line terminated

in its characteristic impedance. One of the cross-sectional views along with the necessary equations [10] used for determining the electric-field distributions inside the chamber are given in figure 3.4.

The test volume in the chamber is the region centered beneath the top plate and the floor, and between the back and side plates and their corresponding front and end walls. The size of the usable test volume is determined by the mode of operation of the chamber. For TEM mode of operation (approximately from 10 kHz to 70 MHz), the maximum recommended test volume is from 1/2 to 1/3 the region between the plates and opposite walls. For reverberating mode of operation (from 300 MHz up), the test volume is the total region between the plates and opposite walls minus approximately 30 cm separation distance from the plates and walls (or 1/6 wavelength at frequencies above 300 MHz). For reverberating mode of operation, this corresponds to approximately 0.7 m x 1.6 m x 3.0 m for the 1/10 scaled chamber.

The theoretically estimated electric-field amplitude distribution inside the chamber, operating in the TEM mode, is given in table 3.5 for the back plate and side plates driven as TEM transmission lines. The electric-field amplitudes are given in terms of the orthogonal components, defined as x (tangential to the plate) and y (normal to the plate) relative to the plate of interest. The distribution inside each cross section is relative to the center value at $x = 0$ and $z = h_i/2$ (back plate) and $y = 0$ and $x = h_i/2$ (side plate). The theory used to obtain these estimates [10] is not valid for determining the field distribution for the top plate driven as a transmission line due to the large gap distance between the plate's sides to the chamber end walls. This field distribution was determined experimentally, as described in Section 4.

Two tuners are used for stirring or redistributing the reflected energy associated with modes excited inside the chamber for the reverberating mode of operation. The tuners consist of 4 rectangular blades, 0.2 m x 0.4 m in cross section, made from plastic foam covered with heavy ($\geq$ 25 mm) aluminum foil. The blades are mounted at offset angles (30 to 45^{o}) with respect to the steel drive shafts that are connected to precision stepping motors. Each tuner motor operates independently, under computer control, so that the tuner revolution rates and positions can be controlled individually or in combination.

The chamber is equipped with a bulkhead access panel located on the back and a 0.762 m high x 2.286 m wide access door located on the front side of the chamber.

3.3 Proposed Full-Size TEM/Reverberating Chamber

The proposed full-scale TEM/reverberating chamber will have the overall dimensions of 13.1 m x 24.1 m x 38.7 m as shown in figure 3.5. It has an approximate test volume of 8 m x 16 m x 30 m. There are two orthogonal plates (top and back), each designed to operate with 75 Ω characteristic impedance for the TEM mode of operation. The third (side) plate is deleted because of the large gradients expected in the field distribution as

evidenced in the scaled chamber results that were considered excessive. The reason for using 75 Ω instead of 100 Ω for the characteristic impedance is to improve the uniformity of the TEM field distribution in the test volume as compared to what was realized in the 1/10 scaled model. This will, however, reduce the field strength by an amount proportional to the square root of the ratio of the impedances $\sqrt{(100/75)}$ for the same input power to the transmission lines. As with the scaled model, the plates will be terminated in their characteristic impedances and driven independently from a high-power rf source when operated as TEM transmission lines. For the reverberating mode of operation, the percent gap between predicted modes for this proposed full-scale chamber is given in figure 3.6. Figure 3.7 gives the percent gap that would exist if the dimensions of the chamber were increased to 16.2 m x 34.4 m x 38.7 m. This larger chamber could be used, in the reverberating mode, at frequencies down to approximately 20 MHz as opposed to 30 MHz estimated for the chamber proposed in figure 3.6. The theoretical composite $\tilde{Q}$ for the full-scale chamber is estimated in figure 3.8 for both cold rolled steel and zinc finishes. The values of μ_r used in calculating the theoretical composite Q for a steel chamber are given in table 3.6. The value of μ_r for a galvanized steel (zinc coated) chamber is assumed to be 1. The conductivities (σ) used for steel and zinc are 0.4 x 10^7 S/m and 1.74 x 10^7 S/m, respectively. The zinc increases the Q by approximately the square root of the ratio of the conductivities of the two metals at frequencies where μ_r is 1.

4. CW Evaluation of the 1/10 Scaled TEM/Reverberating Chamber

4.1 Measurement Approaches

4.1.1 TEM Mode

For TEM mode of operation in the frequency range from 10 kHz to 70 MHz, two techniques are employed in determining and monitoring the E-field being generated in the chamber. The first technique uses measurements of the incident and reflected powers on the sidearms of a bidirectional coupler, the impedance of the TEM transmission lines, the separation distance between the plates and ground plane, and the location between the plates (anticipated placement of the EUT) to determine the E-field normal to the driven plate. The second technique is to place a calibrated isotropic E-field probe in the area where the field is to be measured. Using these two techniques gives a double check to help assure consistency and validity of measured data while providing a real-time display of the field strength as measurements are being made.

4.1.2 Reverberating Mode

For reverberating mode of operation at 300 MHz or higher frequencies, the chamber was evaluated using two different operational approaches referred to as mode-tuned and mode-stirred [5].

For the mode-tuned tests, the tuner is stepped at selected, uniform increments. The net input power supplied to the transmitting antenna, the

power received by a reference antenna, the field-measuring probe responses and the EUT response at each tuner position are measured and recorded. Corrections are then made for the changes in the transmitting antenna's input impedance as a function of tuner position and frequency. The measurement results are then normalized to a constant net input power value. The number of tuner steps used per revolution was 200 (increments of 1.8^{o}).

For the mode-stirred tests, the tuner was continuously rotated while sampling the power received by the reference antenna, the field probe response, and the EUT response at rates much faster than the tuner revolution rate. These measurements were made using a spectrum analyzer and "smart" voltmeters with diode detectors. The "smart" voltmeters are capable of data storage and calculation of various arithmetic functions. Large data samples (up to 9999) are obtained for a single tuner revolution. Tuner revolution rates are adjusted to meet the EUT output monitor, diode probe response time, and sampling-rate requirements of the instrumentation. Typical rates used were approximately 2 to 4 minutes per revolution. The input power was measured only at the beginning of each measurement cycle. For the cw tests, a calibrated bidirectional coupler was used to measure the net input power to the transmitting antenna.

The field level inside the chamber is determined using two techniques similar to TEM mode of operation. One technique uses a reference antenna to measure the power density of the field inside the chamber by use of (4) given in section 3.1. The other technique uses one or more calibrated probes to measure the E-field. These measurements are described in more detail later.

4.2 NIST CW Evaluation System

The block diagram of the system used in the cw evaluation is shown in figure 4.1. A photograph of the NIST equipment used to perform the chamber evaluations is shown in figure 4.2. The test field is established inside the chamber by means of an rf source connected to the appropriate transmitting antenna or plate. Placement of an EUT should fall within the test volume as defined in section 3.2 except, possibly, relative to the floor. The separation distance between the EUT and the floor may be less than 30 cm depending upon the intended EUT configuration relative to the ground plane. (For some applications, the EUT is mounted close to or directly on a ground plane. In these cases the EUT should be mounted the same in the chamber for test purposes.) Test leads and cables are routed to appropriate monitors, for example, outside the chamber through shielded feed-through connectors. Coaxial cables are used for rf signals, and high-resistance lines are used for dc signals. This is done to prevent leakage of the EM energy to the outside environment or into the instrumentation room. A 10-dB attenuator is used whenever possible between the receiving antenna and the 50 Ω power sensor or spectrum analyzer. This is done to minimize impedance mismatch with the receiving antenna and measurement system overload.

The transmitting and reference receiving antennas used for the cw tests are the top, back and side plate transmission lines (1.0 MHz to 1 GHz transmitting), a log periodic antenna (0.2 to 1.0 GHz receiving), and

broadband horn antennas (1.0 to 18.0 GHz transmitting and receiving). A reference receiving antenna is not used at frequencies below 200 MHz. For these frequencies the field was determined only using calibrated probes.

4.3 CW Evaluation and Calibration Results

4.3.1 TEM Line and Antenna VSWR and Chamber Coupling Efficiency

The efficiency with which energy can be injected into or coupled out of the chamber by the transmitting transmission lines or antennas and the receiving antennas is determined by: (a) the VSWR of the lines or antennas [that is, the impedance match between the rf source and the transmitting line or antenna (load) or between the receiving antenna (acting as the source) and its output detector (load)], and (b) the ability of the lines or antennas to couple energy into or out of the particular modes (TEM or higher order modes) that exist at the test frequencies of interest. For the reverberating mode of operation, rotating the tuner changes the characteristics of the field inside the chamber, which in turn influences the effective in-situ VSWR of the antennas. Hence the net input power to the chamber and the received power detected by the reference antenna vary as a function of tuner position. That is, the impedance matches between the rf source and transmitting antenna, and between the receiving antenna and its termination, affect the power transfer between the two antennas. This can result in errors in determining the amplitude of the field inside the chamber if no correction is made. The equation for calculating the magnitude of the error caused by the impedance mismatch is

$$P_f = \begin{array}{l}\text{fraction of maximum}\\ \text{available power absorbed}\\ \text{by the load}\end{array} = \frac{(1 - |\Gamma_S|^2)(1 - |\Gamma_L|^2)}{|1 - \Gamma_S\Gamma_L|^2}, \qquad (7)$$

where Γ_S and Γ_L denote the complex reflection coefficients for the sources and loads respectively as defined above. Their magnitudes, $|\Gamma_S|$ and $|\Gamma_L|$, can be obtained from the appropriate VSWR by the expression,

$$\Gamma_i = (VSWR_i - 1)/(VSWR_i + 1), \quad i = S \text{ or } L.$$

The VSWRs of the transmission lines (plates) and the broadband ridged horn antennas used to excite the chamber are shown in figures 4.3 and 4.4. Figure 4.3 gives the VSWRs of the top, back and side plates; and figure 4.4 is the composite VSWR of the top plate (1.0 MHz - 1.0 GHz) and the broadband ridged horn antenna (1.0 - 18 GHz) in the transmission mode. The receiving antenna's (log periodic, 0.2 - 1.0 GHz, and broadband ridged horn, 1.0 - 18 GHz) VSWRs are similar to figure 4.4. The figures show the maximum, average, and minimum VSWR obtained by rotating the tuner through a complete revolution (360°). Large variations and high values of VSWR exist, especially at the lower frequencies. At higher frequencies (> 2.0 GHz) the VSWRs' variations become less and their values are lower, approaching the free-space VSWR of the antennas. At frequencies below approximately 200 MHz, the VSWR of the lines is unaffected by the tuner rotation. At

frequencies above approximately 10 MHz the high VSWR results from moding effects in the chamber and line impedance mismatch.

The coupling efficiency of the chamber is defined as the ratio of the net input power delivered to the transmitting plate or antenna to the power available at a 50 Ω matched terminals of the receiving antenna. These ratios, called the chamber loss, are given in figure 4.5. The curves show the average and minimum losses measured by the mode-tuned approach, using the top plate (0.1 - 1.0 GHz) and broadband ridged horn (1.0 - 18 GHz) antennas transmitting, with a log periodic (0.1 - 1.0 GHz) and broadband ridged horn (1.0 - 18 GHz) antennas receiving. Impedance mismatch between the receiving antenna and power detector used to measure the received power is not accounted for in these measurements. The magnitude of the error (uncertainty) resulting from this is discussed in [2, 5, 11] and is included in table 4.2.

4.3.2 Chamber Quality Factor

The chamber's quality factor, Q, influences the operation of the chamber in a number of ways for the reverberating region of operation. Examples are tuner effectiveness, rf input power requirements and the accuracy with which test field levels can be established inside the chamber. Chamber Q also influences the time required for the chamber to charge up to a steady-state condition after the input signal is applied. This affects the chamber's response characteristics for pulsed rf testing, as is discussed later.

Results obtained by using (2) to calculate the composite $\tilde{Q}$ with the relative permeability values given in table 3.6, and by using the chamber minimum loss data shown in figure 4.5 together with (3) to determine the experimental Q' are shown in figure 4.6. Figure 4.6 (a) gives the theoretical and experimental Q for the chamber, and figure 4.6 (b) gives the ratio of theoretical to experimental Q. The * and + points indicate the data determined from calculations and experimental measurements, and the solid lines are estimated curve fits. At the higher frequencies the ratio approaches roughly 2.4. This indicates that at frequencies where (2) and (3) are valid, there are relatively small losses other than the loss in the chamber walls and in the transmitting and receiving plates or antennas (antenna efficiencies).

The value of 2.4 is determined from using the conductivity of steel, instead of zinc, in (2) as expected for the zinc flame-spray finish in the chamber. Apparently, the flame-spray finish is too rough compared to the skin depth thickness, giving either the effect of a greatly increased surface area or increased loss, thus making the effective finish equivalent to cold rolled steel. Apparently, this type of finish will not give the desired improvement in Q as anticipated for the higher conductivity zinc over steel.

4.3.3 E-Field Amplitude Calibration

The E-field strength in the chamber can be determined either from measurements of the input power to the transmission lines (TEM operation) or

from the power received at the terminal of the receiving antennas (reverberating operation). It can also be determined by measuring the E-field with calibrated probes.

For low frequencies (TEM region of operation), the electric field can be calculated by using the expression,

$$E \approx \frac{\sqrt{P_i R}}{b} \quad , \qquad V/m \tag{8}$$

where b is the separation distance between the plate and the opposite wall or floor in m, P_i is the net input power to the line in W, and R is the transmission line's impedance ($\approx 100\ \Omega$).

For high frequencies (reverberating region of operation), an equivalent electric field in the chamber may be calculated using the expression,

$$\bar{E}_a = \sqrt{\eta\ \bar{P}_d'} \approx \frac{4\pi}{\lambda} \sqrt{30\ \bar{P}_r} \quad , \quad V/m \tag{9}$$

where η is the average wave impedance of the chamber (377 Ω), $\bar{P}_d'$ is the equivalent power density in W/m^2, in the enclosure, λ is the wavelength in m, and $\bar{P}_r$ is the measured average received power in W. The validity of (9) has been verified and discussed in [5].

Results of the measured electric fields in the chamber for 1 W net input power are shown in figures 4.7 and 4.8. Figure 4.7 gives the average and maximum electric field components, obtained with a calibrated, 3-orthogonal-dipole probe placed at the center of the test zone, with the chamber excited by one of the three transmission line plates. The x, y, and z components are the horizontal longitudinal (end to end), the vertical (top to bottom), and the horizontal transverse (front to back), respectively. In addition, the total magnitude (RSS value of the three components) is also included in figure 4.7 as marked by T. Figure 4.8 gives the maximum and average electric fields determined from received power measurements together with (9) and from measurements that used a calibrated 1 cm dipole probe. For these measurements the chamber was excited using the top plate at frequencies from 0.03 to 1.0 GHz and using a broadband ridged horn antenna at frequencies from 1.0 GHz to 18 GHz. For both figures, the tuners were rotated through one complete cycle (360^o).

Three distinct regions of operation are noted for this scaled chamber. At frequencies below approximately 70 MHz the field is singly moded (TEM mode) and the tuner rotation has little or no effect upon the field's amplitude. Hence, the maximum and average E-field are the same. Also, the dominant component, the one that is polarization-matched with the TEM mode E-field, is evident. The amplitude of the component corresponds to the calculated value determined from measuring the net input power and (8). At frequencies between approximately 70 MHz and 300 MHz, the chamber undergoes

a transition region where higher order modes exist in addition to the TEM mode but in insufficient numbers for the chamber to reverberate properly. Large variations in the field strength exist in this region. At frequencies above approximately 300 MHz, sufficient modes are generated so that the chamber is reverberating effectively. In this region the effect of Q on the resonant modes is evident and the tuner is effective in redistributing the fields within the chamber. Thus the maximum amplitude of the field is substantially higher than that for the TEM mode of operation (as great as 25 dB) for the same net input power of 1 W, and the polarization properties of the components are lost. Note that the amplitudes of the three components in figure 4.7 in this frequency region are approximately the same, and that the total magnitude (RSS value) is about 4.8 dB higher than each individual component.

The 3 orthogonal dipole probes and the 1 cm single dipole probe used to measure the fields in figures 4.7 and 4.8 were calibrated in a planar field using a TEM cell [12] at frequencies up to 500 MHz and in an anechoic chamber at frequencies from 500 MHz to 18 GHz [13]. The assumption is made that the average field over the aperture of the probe inside the reverberating chamber will approximate the planar field used to calibrate the probe. This is reasonable, at least at frequencies for which the probe is electrically small. Also, the open-space far-field gain of an electrically small dipole is small (1.76 dB). Thus, the probe-measured fields should be equivalent, within approximately 1.76 dB, to the E-fields determined using a receiving antenna. This is true if the polarization properties of the probe and receiving antenna are effectively eliminated in the chamber. The variations in the fields determined by using received power measurements and by using the probes (figure 4.8) are typical of the random variations in the data used to determine the field strength inside reverberating chambers. The agreement between the two methods is considered reasonable.

Using the results of figures 4.7 and 4.8, we can calculate the input power requirements for establishing a given field level in the chamber. An example is shown in figure 4.9, which gives the net input power required to generate a 20 V/m field in the 1/10 scaled chamber using the top and back plates and a combination of log periodic and ridged horn antennas.

4.3.4 Effects of RF Absorber Loading and Multiple Driven Plates

Tests were made to determine the effect of lowering the Q in the chamber by adding rf absorbing materials, or of driving more than one plate simultaneously, upon the field in the test zone. The transition region of operation is of particular interest.

Fifteen pieces of 0.2 m x 0.6 m x 0.6 m pyramidal rf absorber were placed inside the chamber as shown in figure 4.10. Measurements were then made using a 5 cm dipole, isotropic probe placed at the center of the test zone similar to the measurement for figure 4.7 with each of the plates driven with 1 W net input power. The results are shown as (b), (d), and (f) of figure 4.11 for the frequency range, 30 to 300 MHz (includes the entire transition region of operation). Results of driving all the plates and just the back and side plates, simultaneously from the same source, without absorber loading, are also shown in figure 4.11 as (h) and (g). These are

compared to the results obtained in figure 4.7, which are reproduced in figure 4.11 for the 30 to 300 MHz region, as (a), (c) and (e).

A comparison of (a) with (b), (c) with (d), and (e) with (f) shows the effect of the absorber loading, lowering both the amplitude and the variation in the amplitude of the measured E-field components. The absorber's effect is most pronounced at the higher frequencies where the absorber is most effective in lowering the Q of higher order mode resonances. Thus, use of absorber would be helpful in reducing the variation in the E-field and hence the uncertainty in determining the amplitude of the test field. However, this must be balanced against the reduction in the field level and the cost and inconvenience of placing the absorber in the chamber. At frequencies above 300 MHz, the absorber would have to be removed from the chamber for proper operation of the chamber in the reverberating region.

Comparisons of figure 4.11 (a) [top plate, no absorber] with (h) [all plates, no absorber] and (c) [back plate, no absorber] with (g) [back and side plates, no absorber] indicate similar field levels and variations in the components. Apparently, little is gained by multiple excitation of the plates.

4.3.5 Tuner Effectiveness

Proper operation of the chamber in the reverberating mode is dependent upon the effectiveness of the tuner to obtain randomness in the distribution of the test field inside the chamber. To achieve this the tuners must be electrically large and shaped or oriented to distribute energy equally into all chamber resonant modes as much as possible. A test to determine how well the tuners are functioning is to measure the ratio of the maximum to minimum E-field in the test volume in the chamber as a function of tuner position. This is done by either measuring the ratio of the received power at the terminals of the receiving antenna or by measuring the electric field using a calibrated probe, relative to a constant net input power to the transmitting antenna. A large ratio (greater than 20 dB) indicates that the tuner is effective in redistributing the scattered fields inside the chamber.

Measurement results for the scaled chamber are given in figures 4.12 and 4.13. Figure 4.12 gives the maximum, average, and minimum E-field based on the receiving antenna power measurements for a complete revolution of the tuners as a function of frequency. Figure 4.13(a) is the ratio of the maximum to minimum E-field, or the tuner effectiveness, determined from figure 4.12, and figure 4.13(b) is the corresponding tuner effectiveness determined from E-field measurements made using a calibrated 1 cm dipole probe. The measurements were obtained by using the same transmitting and receiving antennas as noted in figure 4.5. This ratio is also influenced, in addition to the tuner size and shape, by the chamber Q. For example, placing rf absorber and/or an EUT inside the chamber will lower the chamber's Q, referred to as the loading effect. A minimum ratio of 20 dB is recommended to assure proper operation of the chamber [5]. As seen in figure 4.13, a tuner effectiveness of approximately 30 dB is achieved at frequencies above about 300 MHz for the 1/10 scaled chamber.

4.3.6 Test Zone E-Field Uniformity

Tests were made to determine the E-field uniformity in the chamber as a function of spatial position and frequency. Seven small NIST isotropic probes [14, 15, 16], designed to operate at frequencies up to 2 GHz, were placed at various locations inside the chamber (positions 1, 2, 3, 4, 5, 6, 8; no position 7 was designated) as shown in figure 4.14. Each probe has three orthogonally oriented dipoles which are aligned with the three axes of the chamber, earlier called the horizontal longitudinal (E_x), vertical (E_y), and horizontal transverse (E_z). Measurements were made of the field strength of each orthogonal component at the seven locations for each tuner position (200 steps of 1.8°) for frequencies from 1 to 2000 MHz. These data were normalized for a net input power of 1 W applied at the input terminals of the transmission lines or transmitting antennas. The maximum and average values for each component and the RSS value were then determined from the complete data sets. The results of these measurements obtained when driving the chamber with the top, back, and side plates are shown in figures 4.15 thru 4.20. Figures 4.15, 4.17, and 4.19 give the individual data obtained for all seven probes. Figures 4.16, 4.18 and 4.20 give the averaged values determined from the 7 individual data sets of figures 4.15, 4.17, and 4.19. Again, the three regions of operation are apparent. The spread in the data shows spatial field variations inside the chamber at the indicated frequencies. Note that the dominant components match with the TEM mode E-field polarization for each driven plate in the TEM mode of frequency region (below 70 MHz). For example, the E_y component is dominant for the top plate; E_z is dominant for the back plate; and E_x is dominant for the side plate. These results are in agreement with figure 4.7, as expected. Gradients in the E-fields between the plates are significant. This is due to the placement of the plates close to the top, back, and side walls as necessary for a clear test volume. The vertical E-field difference for the top plate, figure 4.15, over 1/2 the vertical separation distance (positions 2 to 3 and 3 to 4), is approximately 12 dB (± 6 dB). The corresponding values of E_y, at positions 5 and 8 (off the edges of the plate) are significantly lower (≈15 dB) than at the positions directly under the plate. The E_y values at positions 1 and 6 are approximately the same as at position 3, indicating the field is relatively uniform along the length of the plate.

The horizontal transverse component, E_z, for the back plate (figure 4.17) has a total difference in magnitude of approximately 20 dB (± 10 dB from positions 1 to 3 and from positions 3 to 6). This is in good agreement with the theoretically predicted values shown in table 3.5. Again, E_z along the plate, positions 5, 3, and 8 are approximately equal. The E_z values at positions 2 and 4 off the edges of the plate are lower than at position 3 by approximately 2 to 5 dB. The field distributions across the width and along the length of the back plate are reasonably uniform in the described test volume. The cross polarized component, E_y, however, is almost as strong as the dominant E_z.

The horizontal longitudinal component, E_x, for the side plate (figure 4.19) has a difference in magnitude between positions 5 and 3 of approximately 14 dB (± 7 dB). The difference in E_x between positions 3 and 8 could not be measured due to insufficient probe sensitivity and rf input power. We presume, from the results shown in table 3.5, that this difference is approximately the same as for positions 5 and 3. The theoretically predicted difference from table 3.5 is 18 dB. Variations in E_y along the length and across the width of the side plate are relatively small, essentially in agreement with table 3.5. However, because of the excessively large differences along the length of the chamber associated with rf applied to the side plate, use of the side plate to generate TEM fields is not recommended; and for this reason, a similar plate is not to be included in the design for the full-size chamber.

At frequencies above approximately 300 MHz, the differences between the averaged maximum and average amplitudes approach about 8 dB in figures 4.16, 4.18, and 4.20, typical of reverberating operation of the chamber. This is another indication that the chamber is operating properly in the reverberating mode at these frequencies.

The amplitudes of the field components in figures 4.15, 4.17, and 4.19, at frequencies above 300 MHz, are approximately the same. The total magnitude or RSS value of the average field in these figures is approximately 4.8 dB (a ratio of $\sqrt{3}$) greater than the individual components. This will occur if $E_x \approx E_y \approx E_z$, and indicates that the field components are randomly polarized in the chamber. The total magnitudes of the maximum amplitudes in these figures, however, are only about 3 dB greater than the individual components. This indicates that the components' maximum values are not completely independent of each other. This is similar to the results obtained for other reverberating chambers and appears to be inherent in the measurement method. The implication is that if multiple receptors are used (for example an isotropic probe whose output is a function of all three orthogonal dipoles) in establishing the test field amplitude inside a reverberating chamber, the results will be biased by either 3 dB for maximum response data or 4.8 dB for average response data.

A summary of the spatial field distribution obtained from figures 4.15, 4.17, and 4.19 are given in Table 4.1. As mentioned earlier, the E-field amplitude in the chamber is influenced by the chamber's Q. Inserting the 7 probes into the chamber with their lossy transmission lines lowers the chamber's Q and hence the field strength in the chamber compared to what would be present without the loading effect of the multi-probe system.

4.3.7 Test Results from 20 GHz to 40 GHz

Measurements were also made to determine the chamber's coupling efficiency (loss) in the frequency range from 20 GHz to 40 GHz. The method of measurement and the definition of coupling efficiency are the same as those described in sections 4.3.5 and 4.3.1 except that appropriate waveguide hardware and instrumentation were used. The results are shown in figure 4.21. Using these results and $K \approx 2.4$ in (5), we can predict the E-field to be generated in the chamber by a net input power of 1 W. These

results are shown in figure 4.22. Each figure gives the results of two sets of measurements, one made at NIST in Boulder, CO, and the other at a later date at USAEPG in Sierra Vista, AZ. The second set of measurements was made at USAEPG because of the large departure in the first data (between 24 GHz and 26 GHz) from expected results. The initial reaction to the first set of data was to question their validity. However, after some research, it was realized that the data were correct and the differences were due to water-vapor absorption in the frequency range between 20 GHz and 26 GHz as shown in figure 4.23. The curves in figure 4.23 give the calculated normalized propagation attenuation/kilometer in air for 5 relative humidities (RH) [17, 18]. The propagation attenuation is also influenced, to a lesser degree, by temperature and barometric pressure. A check of the weather conditions on the day the measurements were made at NIST verified that the relative humidity was high, accounting for the large loss between 24 GHz to 26 GHz. The relative humidity in Sierra Vista, in contrast, is much lower, about 20 %. These results imply the need to control the environment inside the chamber, especially for measurement at frequencies above 20 GHz.

4.3.8 Summary of CW Calibration and Evaluation Results

Results of the CW calibration and evaluation of the 1/10 scaled chamber indicate three distinct frequency regions of operation. The TEM mode region extends from 10 kHz to approximately 70 MHz, slightly lower in frequency than where the first higher order mode becomes resonant. Test fields established in this region simulate planar fields with the E-field normal to the driven plate and the magnetic field tangential around the plate. Large differences in the fields exist in the test volume between the plates and ground due to the close proximity of the plates to one of the chamber's inside surfaces. These changes in E-field amplitude vary from ± 6 dBV/m about the center location for the top plate, ± 10 dBV/m about the center postion for the back plate, and up to ± 14 dBV/m about the center position for the side plate, for the volume occupying 1/2 the distance between the plates and outside walls or floor. The accuracy with which the E-field within this unperturbed volume can be established is estimated to be approximately ± 2 dB. Input power requirements to establish 200 V/m test field are determined by the plate driven. For vertical polarization (top plate), about 640 W are required. For horizontal transverse polarization (back plate), about 4000 W are required. Use of the side plate is not recommended.

The second frequency region, referred to as the transition region, extends from approximately 70 MHz to 300 MHz. The test fields are a combination of TEM plus an increasing number of higher order modes, as a function of increasing frequency. Thus the field is no longer a simple equivalent plane-wave simulation, but now includes higher order mode components which combine with the TEM mode to produce a more complex field. For this reason, the amplitude determination of the test field has errors that can be as large as ± 10 dB. (See figures 4.11 and 4.17 for example.) The input power required to generate 200 V/m using the top plate is about 200 W at 70 MHz decreasing to about 20 W at 300 MHz. Polarization of the test field changes from vertical E-field at 70 MHz to undefined (reverberating field) at 300 MHz. The input power required to generate 200 V/m using the back plate is about about 1500 W, decreasing to about 20 W at

300 MHz. Polarization of this test field changes from horizontal transverse at 70 MHz to undefined (reverberating field) at 300 MHz.

The third (reverberating) region extends from approximately 300 MHz to 40 GHz or possibly greater. The test fields are complex multimoded fields simulating a near-field environment. The uncertainty of determining the maximum or average amplitude of the test field varies from an estimated ± 8 dB at 300 MHz down to ± 4 dB at frequencies above 2 GHz. The input power required to generate a maximum test field of 200 V/m varies from about 20 W at 300 MHz decreasing to about 3 W at 2 GHz, then increasing again to about 6 W at 18 GHz. (See figure 4.9 for reference). This discussion is summarized in table 4.2.

5. Pulsed RF/Time-Domain Evaluation of the 1/10 Scaled TEM/Reverberating Chamber

5.1 Background

Parameters of EMI signals that can contribute to upset in electronic equipment include: (a) total energy, (b) peak amplitude, and (c) transient characteristics. All these parameters are different inside a reverberating chamber than in free space. Their characterization inside a reverberating chamber, particularly for pulsed rf fields, provides information required for making necessary analysis to determine correction factors as a function of the input pulse parameters. The term "pulsed rf" refers to pulse-modulated cw with characteristics similar to a pulsed radar signal. It also provides insight into the inherent limitations associated with using this complex environment for pulsed rf EMS/V testing. Obviously, these parameters are influenced by the chamber's Q factor, since the time required for a pulsed wave's amplitude to rise to its steady-state value inside the chamber and to decay to zero after the input signal is removed is a function of the chamber's Q. These charge and decay times can be reduced by artificially lowering the chamber's Q, for example, by inserting small amounts of rf absorber. However, this reduces the accuracy of determining the test field amplitude. Results of work to evaluate the response characteristics of the chamber when excited by pulsed rf of various pulse widths and frequencies, and with the chamber loaded with a small amount of absorber, are presented and discussed in this section.

5.2 NIST Pulsed RF Evaluation System

A block diagram of the system used for the pulsed rf evaluation measurements of the chamber is given in figure 5.1. A test field is established inside the chamber by means of a pulsed rf source connected to a broadband ridged horn antenna. The input signal is monitored by a calibrated diode detector connected to the side arm of a calibrated directional coupler. The output of this detector is connected to one channel of the transient digitizing oscilloscope. The field established inside the chamber is monitored by a broadband ridged-horn receiving antenna and calibrated diode detector connected to the second channel of the same oscilloscope. The receiving antenna is similar to the antenna used for transmitting the signal. As in the cw tests, the tuner is rotated to redistribute the rf energy inside the chamber.

The mode-tuned approach was used when it was necessary to optimize the measurement accuracy and to obtain complete statistical information for evaluating the time-domain response characteristics of the signal detected by the receiving antenna. The mode-stirred approach was used for relative measurements with the digitizing oscilloscope placed in its maximum-hold mode of operation. Mode stirring is much faster than the mode tuning and results in much larger data sampling; however, it provides only maximum values. The mode-stirred approach was used to analyze relative information such as charge and decay time and to determine correction factors applied to the test field amplitude when input pulse widths are too short for the chamber to charge up to its steady-state or cw-response values. The digitizing oscilloscope used is capable of measuring signals with rise times of approximately 30 ps, at a sampling rate of 50 kHz, with sample sizes up to 1024 per scan.

5.3 Pulsed RF Evaluation Results

Measurements were made, using the mode-stirred approach, to determine the effect of lowering the reverberating chamber's Q on the charge/decay time of the pulsed rf field excited inside the chamber. Varying amounts of pyramidal rf absorber were placed in the center of the chamber's test zone resting upright (cones up) on the floor. Measurements were first made at 900 MHz (the lowest pulsed rf test frequency), since the response time is the longest at this frequency. Results of these measurements are given in figure 5.2. The graphs of each figure have two traces. The upper trace is an envelope of the input pulses applied to the chamber transmitting antenna. It represents the "painted" envelope derived from all the input pulses during one complete rotation of the tuner. The signal shown is the reduced voltage values measured on the side arm of the directional coupler using a diode detector connected to one channel of the digitizing oscilloscope. The lower trace is the time-domain envelope of the pulses received by the chamber's reference receiving antenna and measured with a second diode detector connected to the second channel of the digitizing oscilloscope. The polarity of this pulse has been reversed to separate the two traces. The diode detectors have built-in 50 Ω load resistors for impedance matching to 50 Ω. The spread in the top trace (input signal) is due to variations in signal amplitude caused by variations in antenna VSWR (input mismatch) as a function of tuner position. The magnitude of this variation is frequency dependent, decreasing as the frequency increases as shown in figure 5.3. Figure 5.2 (a) was obtained with the chamber empty (no absorber). Figures 5.2 (b)-(h) are for increasing amounts of absorber starting with 1 piece of 7.6 cm thick, 61 cm x 61 cm rf absorber, ending with 8 pieces of 30.5 cm thick, 61 cm x 61 cm rf absorber. The effects on both the amplitude and response time are obvious. Figures 5.3 and 5.4 show similar results but at selected frequencies up to 18 GHz. Figure 5.3 gives the maximum received rf pulse waveforms for the empty chamber (with no absorber) excited with 5 μs wide rf pulses. These measurements were used for determining the chamber rise/decay time as a function of frequency, assuming that the input pulse width is wide enough to allow the field in the chamber to charge up to its steady state value. Figure 5.4 shows the effect of a single piece of absorber to reduce the chamber's Q on the maximum received pulse waveform. The input pulse width for these tests was 1 μs.

It is interesting to compare the chamber's response time calculated from the experimentally determined, average Q values, with the measured response time. The response time is approximately $2Q/\omega$ for the signal to rise or decay to 63 % (1 - 1/e) of the steady-state amplitude. These results are shown in tables 5.1 and 5.2. Table 5.1 gives the measured minimum chamber losses, the estimated Q factors, and the measured charge/decay times determined at 900 MHz for varying amounts of absorber. The measured rise/decay times were extracted from the results shown in figure 5.2. Table 5.2 gives the measured average chamber losses, the associated calculated Q factors, the predicted charge-decay times, and the measured charge-decay times at the selected frequencies when the chamber is empty. The calculated and measured response times differ somewhat, but are still within the margin of error expected for these type of measurements.

Mode tuning was used to accurately determine: (a) the ratio of the received pulse amplitude versus input pulse amplitude as a function of time after the input pulse is turned on, and (b) the time required for the chamber to charge up to its steady-state amplitude and then to decay to zero after the pulse is turned off. These measurements were made with the chamber empty (no absorber). Results of these measurements are given in figure 5.5 for three input pulse widths, 1 μs, 3 μs and 10 μs, and for the same 10 frequencies. Each graph shows two curves, one for the maximum and one for the average received signals. By examining these data at the selected frequencies, we can determine the approximate charge-decay times as a function of frequency. These results are shown in figure 5.6. Similar results showing the time required for the received signal to rise to 90 percent of the maximum amplitude are given in figure 5.7. The implication of figures 5.6 and 5.7 is that the input pulse width, at the frequencies of interest, should be equal to or longer than the values shown by the curves for the pulsed rf test field amplitude to reach 63 or 90 percent of the maximum steady-state amplitude. The steady-state amplitude is achieved if the input pulse width is sufficient for the chamber to charge up to 100 percent, or to its maximum output for a given input pulse amplitude.

If the transmitted input pulse width is shorter than the charge time of the chamber, an error will result in terms of establishing a known peak amplitude of the test signal in the chamber. An estimate of a correction factor to apply for this condition can be found by calculating the ratio of the received signal amplitude to the steady-state transmitted signal amplitude as a function of time after turning on the transmitted pulse. Figure 5.8 gives these results, determined from the data of figures 5.4 and 5.5 with the mode-stirred approach. The data are projected down to input pulse widths of 0.1 μs. There is a significant reduction in the correction by loading the chamber with even a small amount of rf absorber. Figure 5.9 shows another way to display the data given in figure 5.8. The correction factors are given, for discrete input pulse widths, as a function of frequency rather than for discrete frequencies as a function of input pulse width. The symbol, *, indicates the actual data extracted from figure 5.8, and the solid curves are the smoothed approximations for these data.

5.4 Comments on Pulsed RF Measurement Results

Mode-tuned data are generally considered to be more accurate than mode-stirred data for absolute measurements of chamber losses and test field

levels. This is so because the measurements are taken for each of the (stopped) tuner positions and sampled at each instant of time during the pulse, so that a maximum value (or minimum or average) can be extracted from the total data taken. Each pulse is digitized at 512 samples in time, for each of the 200 angular positions of the tuner during a complete revolution. Then corrections are made to each measurement for cable loss, coupling ratio of the directional coupler, attenuator calibrations, and diode detector readings according to previous calibration of power response versus signal frequency and indicated voltage levels. Mode-stirred data cannot be corrected in the same manner; hence, only representative maximum values are obtained. However, results derived from mode-stirred data usually have better definition and are thought to be more accurate for determining relative parameters such as the charge time and test field amplitude correction factors. This is because larger data sampling approaching continuous sampling as a function of tuner position is possible, compared to the limited (200 tuner position) sampling for the mode-tuned approach.

For part of the data, the maximum amplitude of the pulsed rf field strength, when measured immediately after the pulse turn-on, appears to be slightly greater than the steady-state value. This overshoot is thought to be due to the imperfect leading edge of the pulse produced by the pin diode switch in the pulse source. The overall trend, however, is for the shorter pulses to have a smaller value of peak detected voltage. This is because the on-time is not sufficient for the EM energy in the reverberating chamber to reach its steady-state value. Thus, data were taken for a range of pulse widths to determine the correction factor to be applied when using the chamber to take EMS/V data for very short radar pulses.

6. Projecting the 1/10 Scaled Chamber CW and Pulsed RF Measurement Results to a Full-Scale TEM/Reverberating Chamber

The theoretical projected composite quality factor for a full size chamber (13.1 m x 24.1 m x 38.7 m) is given in figure 3.8. The K factor, defined as the ratio of the theoretically determined composite $\tilde{Q}$ by (2) to the experimentally determined Q' by (3), for the 1/10 scaled chamber, is shown in figure 4.6 (b). This factor approaches a constant value of approximately 2.4. This value is consistent with K factors determined for other reverberating chambers of different sizes but with similar materials. Thus, assuming the same K factor for the full-scale chamber, we can project the minimum loss for the full-size chamber. These results are shown in figure 6.1 for both steel and galvanized steel. The shape of the curve for steel, at frequencies below 1 GHz, is due to the frequency dependence of the permeability of steel as was indicated in table 3.6.

The results of figure 6.1 can be used to predict the E-field in the full-size chamber by using (9) from Section 4.3.3 and the definition of loss (Loss $= P_r/P_t$). These results are shown for steel and zinc coated steel in figure 6.2 (a) when the input power is 200 W. The curves for aluminum and copper were calculated from the zinc data in accordance with the theory that the power density in the chamber is proportional to the square root of the conductivity of the metals used for the wall surface. Thus, aluminum and

copper surfaces should result in approximately 1.54 dB and 2.63 dB higher fields, respectively, than the zinc surface of the same chamber size.

Figure 6.2 (b) gives the projected E-field to be generated in the full-size chamber by an input power of 200 W, based on the data obtained for a 3.69 m x 5.18 m x 9.79 m galvanized steel chamber located at RADC, Griffiss AFB, NY, and for a 3.51 m x 5.18 m x 10.82 m welded-steel chamber located at the Naval Surface Weapons Center (NSWC), Dahlgren, VA. A comparison of the appropriate curves indicates excellent agreement for the steel-chamber data [figures 6.2 (a) and (b)] but only limited agreement for zinc. Differences are due to the assumption that the chamber surface is of pure zinc. In reality, however, the actual chamber coating is not pure zinc.

Figure 6.3 gives the projected charge time for the full-scale, empty, chamber (no absorber loading). These results are based on the theoretical determination of Q for steel and zinc chambers and an assumed K-factor of 2.4 for reduction in Q, which is further reduced by approximately 10 dB to give an equivalent average chamber.

The projected operational characteristics for the full-scale chamber are summarized in table 6.1. Again three regions of operation are expected as defined earlier. The results are scaled by a factor of 10 from table 4.2 except for the input power requirements for a given E field.

7. Performing EMC/V Measurements Using the TEM/Reverberating Chamber

7.1 Performing EMC/V Measurements With Manual Operations

An especially useful application of the TEM/reverberating chamber is to perform shielding effectiveness (SE) measurements. A block diagram of a simple, manually operated system, which does not require the use of a computer controller, is shown in figure 7.1. The system uses a sweep oscillator and spectrum analyzer to cover approximately octave bandwidths in the frequency range of interest. Two measurement approaches are required depending upon the region of operation (TEM or reverberating mode).

For cable/connector SE measurements, in the TEM mode region of operation, a reference cable is placed in the chamber oriented to give maximum coupling to the magnetic field of the TEM mode. This cable typically consists of a 72 Ω unshielded parallel wire configured, as nearly identical as possible, to the cable/connector under test (CUT). Reference measurements are made by establishing the test field in the chamber at the frequencies of interest and recording the power coupled to the output of the reference cable in channel A of the analyzer. The net input power for these measurements is recorded on the Y_1 channel of the xy recorder using the time base output for the x axis. The time base is set the same as the oscillator sweep rate and is triggered at the same time the oscillator starts its sweep. The CUT is then placed in the same location and orientation as the reference cable and the test field is reestablished at the same test frequencies. The power coupled to the output of the CUT is recorded in channel B of the analyzer at the same time the net input power is recorded on channel Y_2 of the xy recorder. Impedance mismatch errors are corrected by using (7) as described in section 4.3.1. The SE is then determined by

$$SE = 10 \log \frac{P_{CUT}\, P_{i\ (ref)}}{P_{ref}\, P_{i\ (CUT)}} \quad , \tag{10}$$

where P_{CUT} is the power coupled to the CUT; $P_{i\ (CUT)}$ is the net input power applied to the chamber when measuring P_{CUT}; P_{ref} is the power coupled to the reference cable: and $P_{i\ (ref)}$ is the net input power applied to the chamber when measuring P_{ref}.

Measurements are made in the reverberating region of operation in much the same manner as for TEM mode of operation. The exceptions are that now the tuner(s) are rotated at revolution rates fast (about 1/s) compared with the sweep oscillator sweep speed (100 s/sweep). The spectrum analyzer is set up to measure in its maximum hold mode and tc scan the same frequency band as the sweeper at fast scan rates (20-30 ms/scan). Resolution and video bandwidths compatible with the scan rate, dynamic range requirements are selected to ensure that the analyzer is operating in calibration. If the SE is anticipated to be high (> 40 dB), a calibrated attenuator is used between the output of the reference antenna and the analyzer. The reference antenna replaces the reference cable at frequencies in the reverberating mode region of operation.

The steps for performing the measurements proceed as follows: First, connect the reference antenna to the analyzer and measure its received power in dBmW for the fields established in the chamber by the power applied to the transmitting antenna or plate. Take a sweep and store the measurement results in one of the channels, for example channel A, of the analyzer while also recording the net input power on channel Y_1 of the xy recorder. Next, connect the output from the CUT up to the analyzer and repeat the measurement, being sure the net input power remains the same or is measured and recorded on channel Y_2 of the xy recorder. It may require up to 3 or 4 sweeps to fill in the maximum received power across the frequency band. Store the results in dBmW in the analyzer's second channel, for example channel B. Then subtract channel B from A and add the calibrated attenuator factor in dB, if used, to get the SE in dB. This assumes that the cable lengths between the reference antenna and the CUT to the analyzer are the same. If limited sweeps are made, use the envelope of the CUT data to subtract from the reference data so that the minimum SE values are obtained. Using this procedure will ensure adaquate accuracy without requiring long sweep times or a large number of repeated sweeps. (Normally it is not necessary to wait for a maximum recording at all frequencies.) These data give nearly continuous frequency coverage measurements of SE. Measurements of EUT response to determine the susceptibility or shielding effectiveness of enclosures proceed in much the same manner as above.

For some applications, it may be advisable to determine the shielding factor (SF) of the EUT. This is defined as the ratio of the EUT's response expressed in power to the test field's power density,

$$SF = 10 \log (P_{EUT}/P_d') \quad , \quad dB/m^2 \tag{11}$$

where P_{EUT} is the power coupled to the EUT in W, and P_d' is the power density inside the chamber in W/m^2. The SF is similar in concept to the well known antenna factor used in antenna calibrations.

An alternate approach to these measurements is shown in figure 7.2. This block diagram gives the setup for measuring radiated emissions or SE by driving the CUT in the radiating mode or by measuring the radiated emissions from the EUT. (For radiated emission measurements, the EUT is not connected to the rf source, but, rather, becomes the source itself.) For SE measurements, mismatch errors caused by large VSWRs of the CUT are minimized by using the bidirectional coupler to measure the net input power to the EUT and to the chamber's transmitting antenna, while measuring the power received by the reference antenna for each case. Use of a bidirectional coupler to measure the net input power gives the equivalent of an impedance match source for the measurements. For the case of cable, the SE is then determined by

$$SE = 10 \log \frac{P_{n(CUT)} \; P_{ref(t)}}{P_{n(t)} \quad P_{ref(CUT)}} \quad , \text{dB} \qquad (12)$$

where $P_{n(CUT)}$ is the net input power to the the cable; $P_{ref(CUT)}$ is the power received by the reference antenna when power is applied to the CUT; $P_{n(t)}$ is the net input power to the chamber's transmitting antenna or plate; and $P_{ref(t)}$ is the power received by the reference antenna when power is applied to the chamber's transmitting antenna.

For the case of an EUT in general, the power radiated from it excites the chamber and is coupled to the reference antenna. This coupled power is measured on one channel of the analyzer. The EUT is then turned off and power is applied to the chamber's transmitting antenna or one of the plates. The output power from the oscillator is adjusted to give approximately the same coupled power to the reference antenna. This may require the use of a calibrated attenuator between the reference antenna and analyzer to keep from reducing the oscillator output power too low. These measurements are recorded on another channel of the analyzer. The radiated power from the EUT is then determined by:

$$P_{rad(EUT)} = P_{n(t)} \frac{P_{ref(EUT)}}{P_{ref(t)}} \quad . \quad W \qquad (13)$$

where $P_{ref(EUT)}$ is the power received by the reference antenna when the EUT radiates.

An example of SE data obtained using the block diagram of figure 7.1 is given in figure 7.3. The EUT is a TEM cell having a cross-section area of 3 cm x 6 cm with a 15 mm circular aperture. This EUT is a control standard device developed at NIST for SE measurement standardization. Two traces are shown in figure 7.3. The top trace is the measurement of the reference

antenna received power recorded, in dBmW, on channel A of the analyzer. The bottom trace is the received power coupled to the EUT recorded, in dBmW, on channel B of the analyzer. A 10 dB attenuator was used between the reference antenna and analyzer in performing this measurement. This 10 dB must be added to the difference, $P_{ref} - P_{EUT}$, in calculating the SE of the EUT.

7.2 Automated EMC/V Measurements

7.2.1 TEM Mode Measurement Procedures

Detailed step-by-step measurement procedures using TEM cells for EMC measurements are given in [1]. Measurements using the combined chamber in the TEM mode region of operation follow the same steps. These consist of:

(a) Determining the EUT test parameter requirements in terms of test field amplitude, waveshape, modulation, frequency range and interval, exposure polarization, exposure time requirements, and EUT performance degradation criteria;

(b) Placing the EUT inside the cell in one of two locations for testing. The first location is close to the ground plane to minimize exposure of the EUT's input/output, power, and monitor leads to the field generated inside the cell. The second position is midway between the plate and ground plane. This position provides greater field exposure to the EUT's leads and hence gives an indication of how energy is coupled to the EUT;

(c) Accessing the EUT as required for operation and performance monitoring. The EUT input/output and ac power leads should be as nearly the same as in its intended use. Leads should be the same length, if possible, and be terminated into their equivalent operational impedances so as to simulate the EUT in its operational configuration. Care must be taken in routing the leads including monitor leads (if not transparent to the rf field) inside the chamber for obtaining the most meaningful, repeatable results. Placement of the leads, wiring harnesses, etc., should be recorded for future reference so that if repeat measurements are required, the leads can be placed as nearly identical to the original tests as possible. Fiber optics or high-resistance lines should be used for monitoring the operation of the EUT if possible. Such leads minimize coupling to and distortion of the test fields;

(d) Connecting the measurement system as shown in figure 7.4; and

(e) Applying power to the chamber's TEM lines with the EUT in operation and recording the EUT's monitor responses as a function of the test field level, modulation parameters, polarization, and frequency to determine immunity.

7.2.2 Reverberating Mode-Tuned Measurement Procedure

A detailed step-by-step measurement procedure and flow diagram for performing automated radiated susceptibility tests using a reverberating

chamber is contained in [5]. The procedure is the same for the combined chamber used in the reverberating region of operation. It is summarized briefly as follows:

(a) Determine the testing requirements for the EUT as referred to in section 7.2.1 item (a) above;

(b) Place the EUT inside the chamber and access it for operation and monitoring;

(c) Connect the measurement system as shown in figure 7.5;

(d) Input the measurement and calibration parameters into the computer. These include frequency ranges and increments for the tests, number of tuner steps to be used, signal generator output levels to generate the required test field amplitudes, EUT output level maximum limit to prevent damage, EUT response time, and cables, directional couplers, and sensors calibration factors; and

(e) Perform the measurements in automated sequence starting at the lowest frequency and level, increasing the frequency in increments at a constant exposure level and then increasing the levels until the maximum test level is achieved or the EUT maximum allowable response is reached. Correct the measurement data using the appropriate calibration factors previously put into the computer. (This can occur simultaneously with making and recording the measurements.) The optimum technique for obtaining mode-tuned data is to step or increment the frequencies at each tuner position before stepping the tuner to its next position. When the tuner is stepped, it should be allowed to stabilize while power meters, voltmeter, monitors, etc., are being zeroed and residual offsets measured. Obviously the rf is turned off while this is done. The rf power is then turned on; the test field is established; the measurements are made at each frequency; and the data are corrected (with respect to a given input power) and stored. The corrected data are then configured at the end of the run, after the tuner has been stepped through all positions to complete one revolution (360°) and compiled by frequency. Various calculations of averages are then made and the data are presented in the final form.

7.2.3 Reverberating Mode-Stirred Measurement Procedure

Although the mode-stirred measurement approach begins in a similar manner to the mode-tuned described above, the automated measurement sequence of events is somewhat different, and hence some parameters necessary for performing the measurements differ from the mode-tuned approach. The procedure is summarized briefly as follows, after determining the EUT test parameters:

(a) Place the EUT inside the chamber and access it for operation and monitoring;

(b) Connect the measurement system as shown in figure 7.5;

(c) Input the measurement and calibration parameters into the computer. These include the frequency ranges and increments, the signal generator

output levels, range and increments, the EUT output level minimum and maximum response limits, the EUT response time, the cables, directional couplers, and sensors calibration factors, and the tuners rotation rates;

(d) Perform the measurements using the automated sequence, which includes setting the generator to its first frequency, starting the tuners in motion, and monitoring the EUT response(s) while slowly increasing the test fields. When the EUT minimum response is exceeded or the maximum test field is reached, the tuners are stopped; the system is initialized with the monitor voltmeters; and the spectrum analyzer is set up to start taking data when triggered. The rf power is turned on, the net input power is measured and the tuners are placed into motion as the voltmeters and spectrum analyzer are triggered into performing their measurements;

(e) Make calculations of averages and corrections for calibration factor while the measurement proceeds. The results are then compiled at the end of each frequency run after one complete revolution of the tuner and stored in memory for presentation at the conclusion of the measurements. If the maximum EUT response is reached during the measurement, the generator output is reduced by an interval of 1 dB and the measurement is repeated starting with a complete new initalization and a full 360° revolution of the tuners. This ensures accurate results without damaging the EUT.

7.2.4 Comparison of TEM/Reverberating Chamber Measurement Results with Anechoic Chamber Tests - Some Examples

Comparisons of the EUT response obtained using a reverberating chamber with anechoic chamber data are typically made in terms of maximum or peak values. The main reason for this is that the EUT's worst-case performance or susceptibility is normally what is desired. An additional practical consideration is that it is very difficult to obtain a true average EUT response from anechoic chamber data. Even determining the EUT's peak response in an anechoic chamber may require considerable effort involving complete pattern measurements.

The benefit of making this type of comparison is to obtain a "correlation factor" between results obtained in the TEM/reverberating chamber and those obtained in an anechoic chamber. This was done for three reference standard EUTs. These were: (a) a 1 cm dipole probe, (b) a small broadband horn antenna similar to what is used at frequencies from 0.8 to 18 GHz as the transmitting and receiving antennas in the chamber, and (c) a small TEM cell with 3 cm x 6 cm cross section and a 15 mm diameter circular aperture. The measurements were performed in a combination of facilities including the RADC's small 1.41 m x 1.57 m x 1.75 m aluminum reverberating chamber located at Griffiss AFB, NY; the NIST 2.74 m x 3.05 m x 4.57 m steel reverberating chamber located in Boulder, CO; the USAEPG 1/10 scaled 1.31 m x 2.41 m x 3.87 m TEM/reverberating chamber located presently at Ft. Huachuca, AZ; and the NIST 4.9 m x 6.7 m x 8.5 m anechoic chamber located in Boulder, CO.

The maximum responses obtained using the 1 cm dipole probe measured in the 1/10 scaled TEM/reverberating chamber, the NIST reverberating chamber, and the NIST anechoic chamber are given in figure 7.6. The probe response in the anechoic chamber is greater than its response in the reverberating

chamber and TEM/reverberating chamber by an average of about 2 dB. This is expected, since 2 dB corresponds approximately to the free-space gain of an electrically small dipole. Thus, the correlation factor between the reverberating chambers' and the anechoic chamber's results is the free-space gain of the EUT [5].

Measured maximum responses of a broadband horn antenna obtained using the 1/10 scaled TEM/reverberating chamber and the NIST anechoic chamber are shown in figure 7.7. The horn was aligned on the boresight (main beam) of the transmitting antenna for the anechoic chamber measurements to obtain the maximum response. As expected, the horn response is greater in the anechoic chamber than in the TEM/reverberating chamber by approximately its free-space gain. This is shown in figure 7.8 where the horn's calibrated free-space gain has been subtracted from its measured maximum response. Clearly, the results are in general agreement.

Figure 7.9 shows a comparison of the shielding effectiveness of a small apertured TEM cell obtained from theoretical calculations, from measurements made using the RADC small reverberating chamber, and from measurements made using the 1/10 scaled TEM/reverberating chamber. Both mode-tuned and mode-stirred approaches were considered using the scaled TEM/reverberating chamber. The RADC chamber measurements were performed using the mode-tuned approach. The mode-tuned results for the two chambers are in good agreement, but are greater by a few decibels at the higher frequencies than the theoretically determined values (straight line). The mode-stirred data agree better with the theoretically determined values. The limited number of tuner positions (200) used for the mode-tuned measurement may explain the higher SE results, since a limited sample at higher frequencies does not allow a true measurement of the peak response of the EUT. In general, however, the results agree within predicted measurement uncertainties.

8. Summary and Conclusions

The designed hybrid chamber has three distinct regions of operation: (a) TEM mode, (b) transition, and (c) mode-stirred. For the 1/10 scale chamber, the TEM region covers the frequency range from approximately 10 kHz to 70 MHz; the transition region covers the frequencies from 70 MHz to about 300 MHz; and the mode-stirred region covers the frequency range from 300 MHz to $\geq$ 40 GHz. In the transition region, the first few higher order modes are excited inside the chamber, but in insufficient number for the chamber to reverberate properly. Thus, the test field is a combination of the TEM mode and a limited number of higher order modes that yield a complex field that is difficult to accurately determine both in polarization and amplitude. Techniques such as absorber loading, to suppress the Q of the higher order modes, and test field averaging over the test volume, using multiple probes, may be helpful in reducing errors in establishing the test field and in defining the test field parameters.

Test fields are excited in the chamber at frequencies up to approximately 1 GHz by using the transmission lines. At frequencies above approximately 1 GHz, ridged horn antennas are used. The parallel plate lines should be unterminated (open circuit) with the bulkhead feed-through connectors capped to prevent rf leakage to outside the chamber when they are

not in use. Other important characteristics may be summarized as follows, together with some recommendations:

(a) Spatial variations of the maximum and average electric fields in the test volume of the chamber are given in table 4.1 at a few selected discrete frequencies. These data were obtained using the NIST multiprobe system and the mode-tuned approach with 200 tuner increments per revolution at frequencies from 0.03 to 2 GHz. The limitation for determining the spatial E-field variation depends on the increasing mode density and hence field complexity in the chamber as a function of increasing frequency. The spatial E-field variations should decrease as frequency increases above 2 GHz to less than the result of ± 2 dB shown in the table for 2 GHz.

(b) Expected field levels to be generated in the three frequency regions by a given input power are presented in table 4.2, together with estimated uncertainties.

(c) The maximum E-field established inside the chamber at frequencies above 300 MHz is about 7 to 8 dB greater than the average E-field. This is consistent with the previous results obtained for other reverberating chambers such as the RADC large chamber, the Naval Surface Weapons Center (NSWC) chamber, and the NIST reverberating chamber.

(d) Reference standard EUT responses determined in this scaled chamber are approximately the same for the same EUT at the same field levels as using RADC, NSWC and NIST reverberating chambers.

(e) The directional characteristics of an antenna or EUT placed inside this hybrid chamber operated in the reverberating region of frequencies are lost, resulting in an equivalent gain of 0 dB in the highly complex field environment.

(f) The correlation factor between free-space (anechoic chamber) and reverberating chamber measurement results for the same EUT is the free-space (far-field) gain of the EUT. This implies that susceptibility criteria determined for an EUT using a reverberating chamber should include an additional factor proportional to the EUT's open-field estimated gain as a function of frequency.

(g) If the chamber is used for pulsed rf EMS/V testing, and the input pulse widths are shorter than the chamber's charge time, an error will result in establishing a known maximum amplitude of the test signal. An estimate of the correction factors to apply for shorter pulses is given in figures 5.8 and 5.9.

(h) The use of rf absorbing material inside the chamber significantly reduces the Q and charge time of the chamber, and hence should be considered as an effective means to improve the fidelity of the test pulse waveform to be applied to the chamber. However, care must be exercised to ensure that the absorber would not excessively reduce the Q so that the reference antenna received power drops by more than 6 dB, or the tuner effectiveness is reduced to less than 20 dB.

(i) The use of rf absorbers also reduces the amplitude and variations in the E-field generated in the transitional frequency region, and thus the uncertainly in establishing the test field level, at perhaps the expense of increased rf input power requirements.

(j) The mode-tuned approach is recommended for use at frequencies from 70 MHz to 2 GHz with at least 200 tuner positions per revolution, if absolute levels of the test field are required. The mode-stirred approach is recommended for use at frequencies above 2 GHz for absolute measurements (with more than 3000 samples per revolution for frequencies between 2 to 4 GHz, and more than 5000 samples per revolution for frequencies above 4 GHz). The mode-stirred approach is also recommended for all frequencies above 300 MHz if only relative measurements are made.

(k) Antennas for transmitting rf energy into the chamber and for measuring the test E-field should not be used outside their specified frequency range. For example the 0.8 to 18 GHz ridged-horn antennas should not be used outside their specified band.

(ℓ) Additional work is needed to verify experimentally the correction factors shown in figures 5.8 and 5.9. This could be accomplished by comparing the measured responses of a well-characterized EUT to cw and pulsed rf fields as a function of frequency and pulse widths using both an anechoic chamber and the TEM/reverberating chamber.

(m) If corrections are not made for mismatches of the transmitting and receiving antenna, absolute amplitude measurements of the test field inside the chamber will be lower than the actual values. This will cause an error in determining the EUT response, which will also be too low. Experiences in performing this type of measurements indicate that these errors may be as great as 5 dB when VSWRs exceed 15 to 1.

(n) The average wave impedance in the reverberating region of operation, when the maximum response of an EUT is measured, appears to be higher than 377 Ω. This is especially true for frequencies lower than 2 GHz. This means that if a wave impedance of 377 Ω is assumed when determining the maximum amplitude of an exposure field, there will be a systematic error resulting in too low a calculated E-field, and thus also in too high an EUT response. If the field strength is determined by using a calibrated E-field probe, there is still some uncertainty, since the environment in which the probe is calibrated is different than the reverberating chamber environment.

9. Acknowledgments

Work described in this report was sponsored by the U. S. Army Electronic Proving Ground, Ft. Huachuca, AZ, with Robert Weeks as project officer. The authors acknowledge his assistance in making this project possible. In addition, the authors express their appreciation to Motohisa Kanda for his support and to J. W. Adams for his helpful comments.

10. References

[1] Crawford, M. L. Generation of standard EM fields using TEM transmission cells. IEEE Trans. on Electromag. Compat. EMC-16 (no.4):189-195; 1974, November.

[2] Crawford, M. L.; Workman, J. L. Using a TEM cell for EMC measurements of electronic equipment. NBS Tech. Note 1013; Revised 1981 July.

[3] Corona, P.; Latmiral, G.; Paolini, E.; Piccioli, L. Performance of a reverberation enclosure for power measurements in the microwave range. 2nd Symp. Tech Exhibition on EMC; 1977; Montreux, Switzerland.

[4] Bean, J.L.; Hall, R.A. Electromagnetic susceptibility measurements using a mode-stirred chamber. IEEE Int. Symp. on EMC; 1978 June; Atlanta, GA.

[5] Crawford, M.L.; Koepke, G.H. Design, evaluation and use of a reverberation chamber for performing electromagnetic susceptibility/vulnerability measurements. NBS Tech. Note 1092; 1986 April.

[6] Ma, M.T.; Kanda, M.; Crawford, M.L.; Larsen, E.B. A review of electromagnetic compatibility/interference measurement methodologies. Proc. of IEEE; Vol. 73, No. 3; 1985 March.

[7] Liu, B. H.; Chang, D. C.; Ma, M. T. Eigenmodes and the composite quality factor of a reverberating chamber. NBS Tech note 1066; 1983 August.

[8] Dunn, J. M. Local, high-frequency analysis of the fields in a mode-stirred chamber. IEEE Trans. on Electromag. Compat. EMC-32 (no. 1): 53-58; 1990 February.

[9] Corona, P.; Latmiral, G.; Paolini, E. Performance and analysis of reverberating enclosures with variable geometry. IEEE Trans. on EMC; EMC-22 (no. 1): 2-5; 1980 February.

[10] Wilson, P. F. On slot-coupled waveguide and transmission line structures. Ph.D. Dissertation, Dept. of Electrical Engineering, Univ. of Colorado, Boulder; 1983.

[11] Crawford, M. L.; Koepke, G. H.; Ladbury, J. M. EMR test facilities - Evaluation of reverberating chamber located at RADC, Griffiss AFB, Rome, NY. NBSIR 87-3080; 1987 December.

[12] Crawford, M. L. Generation of standard EM fields for calibration of power density meters: 20 kHz to 1000 MHz. NBSIR 75-804; 1975 January.

[13] Bowman, R. R. Calibration techniques for electromagnetic hazard meters: 500 MHz to 20 GHz. NBSIR 75-805; 1976 April.

[14] Larsen, E. B.; Ries, F.X. Design and calibration of the NBS isotropic electric-field monitor [EFM-5], 0.2 to 1000 MHz. NBS. Tech. Note 1033; 1981 March.

[15] Kanda, M.; Driver, L.D. An isotropic electric-field probe with tapered resistive dipoles for broad-band use, 100 kHz to 18 GHz. IEEE Trans. on Microwave Theory and Tech. MTT-35 (no. 2); 1987 February.

[16] Bensema, W.D.; Reeve, G.R.; Koepke, G.H. A multisensor automated EM field measurement system. Proc. IEEE IMTC; 1985; Tampa, FL.

[17] Liebe, H. J. An updated model for millimeter wave propagation in moist air. Radio Science 20 (no. 5): 1069-1089; 1985 May.

[18] Liebe, H. J.; Layton, D. H. Millimeter-wave properties of the atmosphere: Laboratory studies and propagation modeling. NTIA Report 87-224; 1987 October.

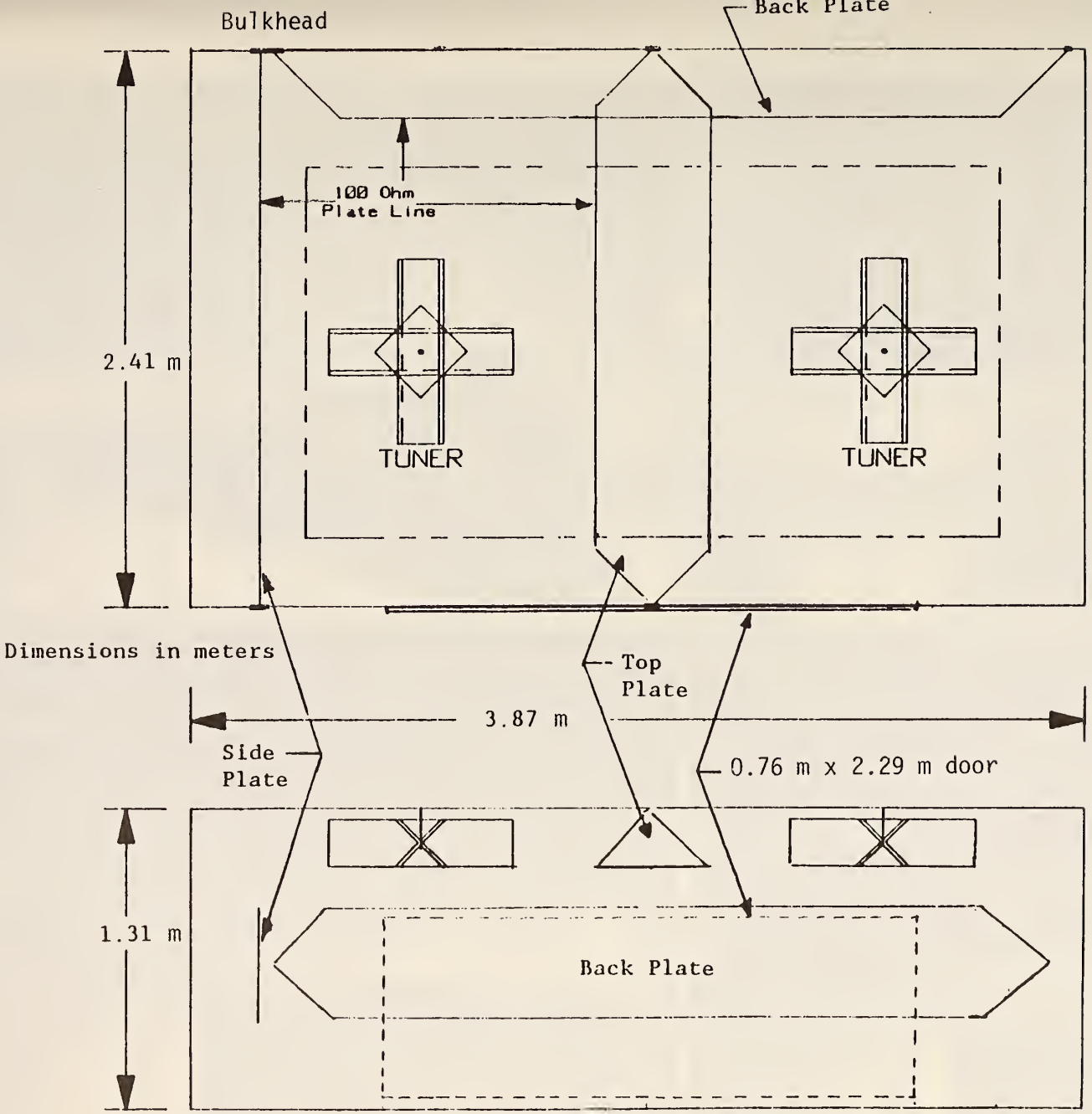

Figure 3.1 Cross sectional sketches of the USAEPG 1/10 scaled TEM/reverberating chamber.

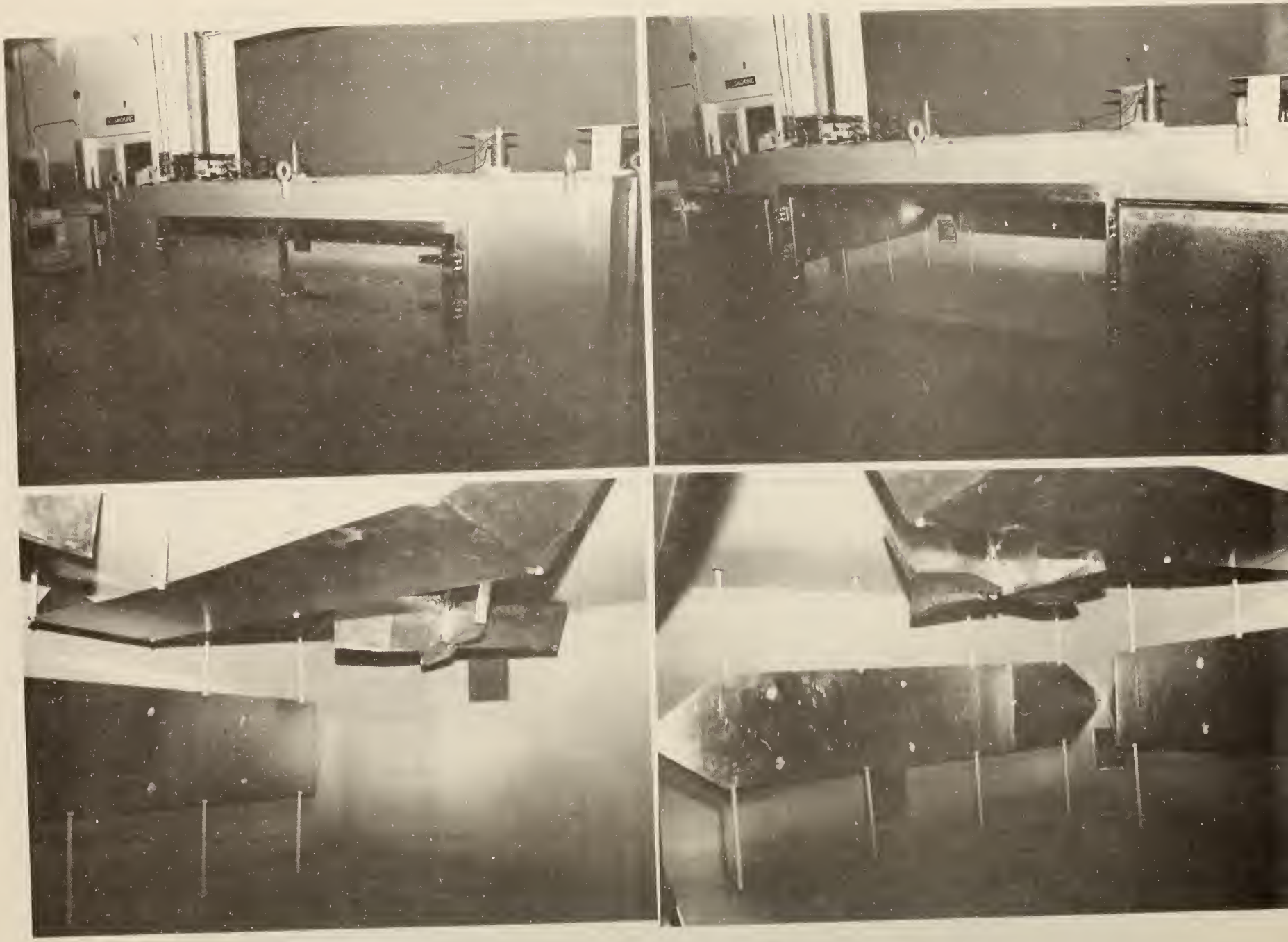

Figure 3.2 Photographs of the USAEPG 1/10 scaled TEM/Reverberating chamber.

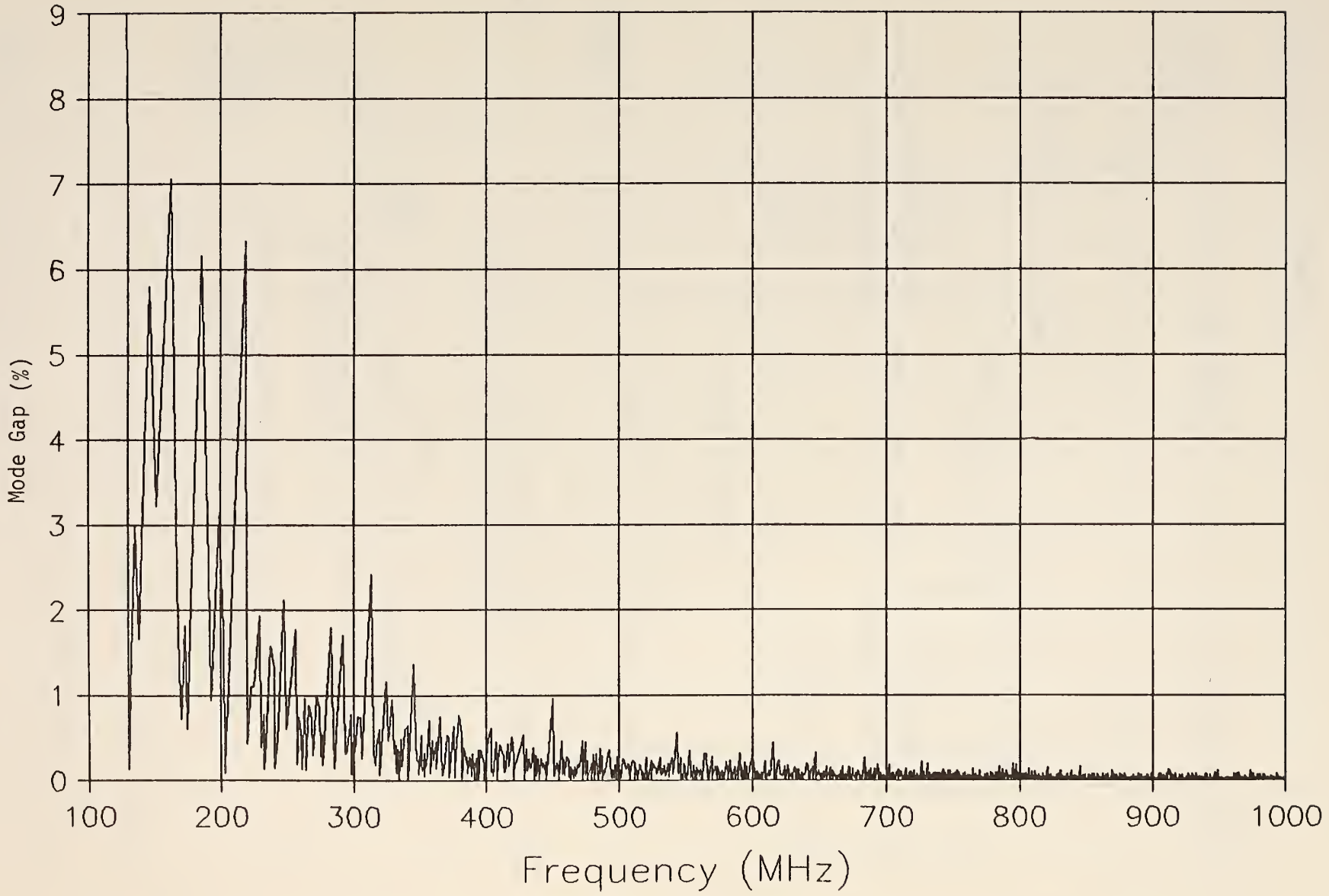

Figure 3.3 Theoretical mode distribution for the 1/10 scaled TEM/reverberating chamber (1.31 m x 2.41 m x 3.87 m).

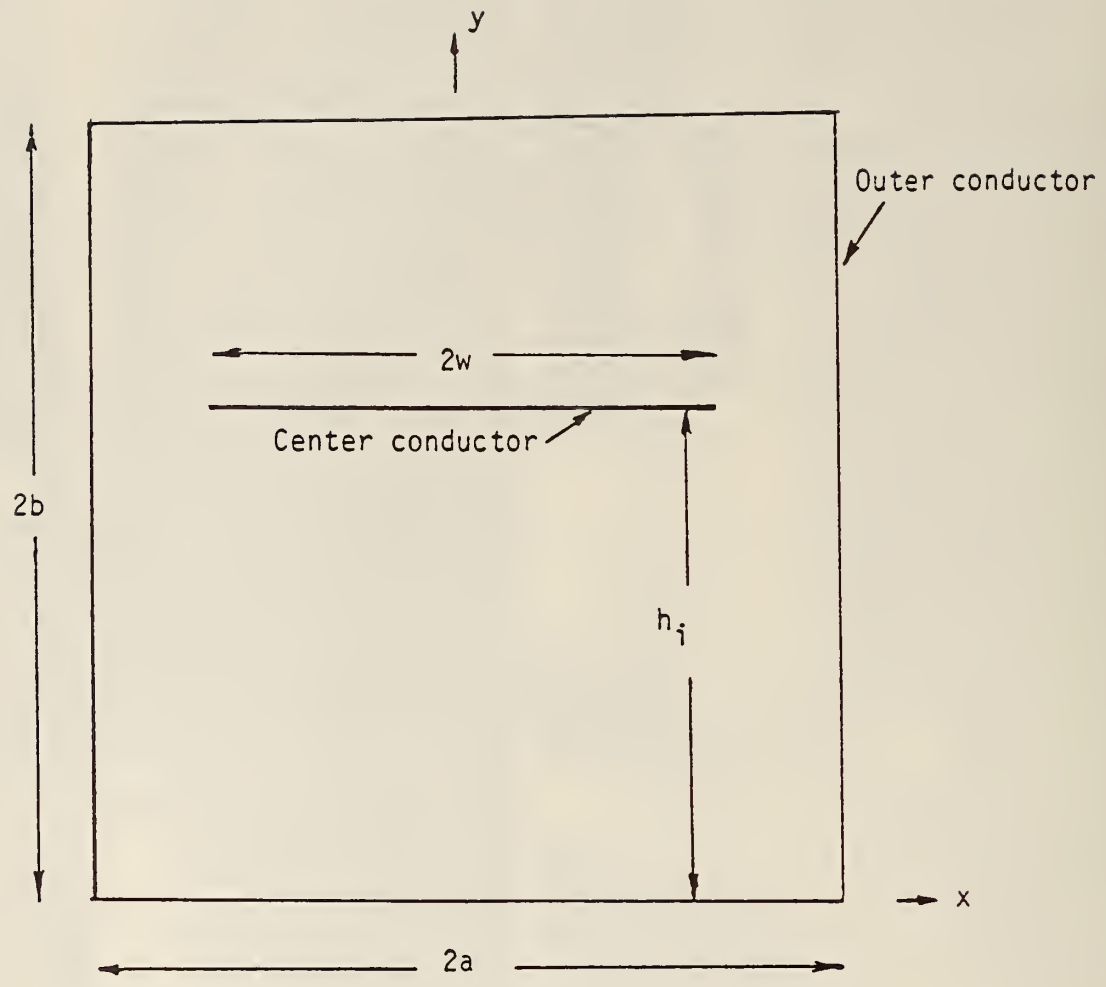

Figure 3.4 Cross-sectional view of a TEM cell for determining the field distribution.

$$E_y = \sum_{m_o} \sin(m\pi/2) \cos(m\pi x/2a) \left[J_0(g') + J_2(g') + \ldots\right] \frac{\cosh \frac{m\pi}{2a} (h_i - y)}{\sinh \frac{m\pi}{2a} h_i}$$

$$E_x = \sum_{m_o} \sin(m\pi/2) \sin(m\pi x/2a) \left[J_0(g') + J_2(g') + \ldots\right] \frac{\sinh \frac{m\pi}{2a} (h_i - y)}{\sinh \frac{m\pi}{2a} h_i}$$

where $m_o = 1, 3, 5, \ldots$

and

$$g' = m\pi g/2a, \quad g = a - w.$$

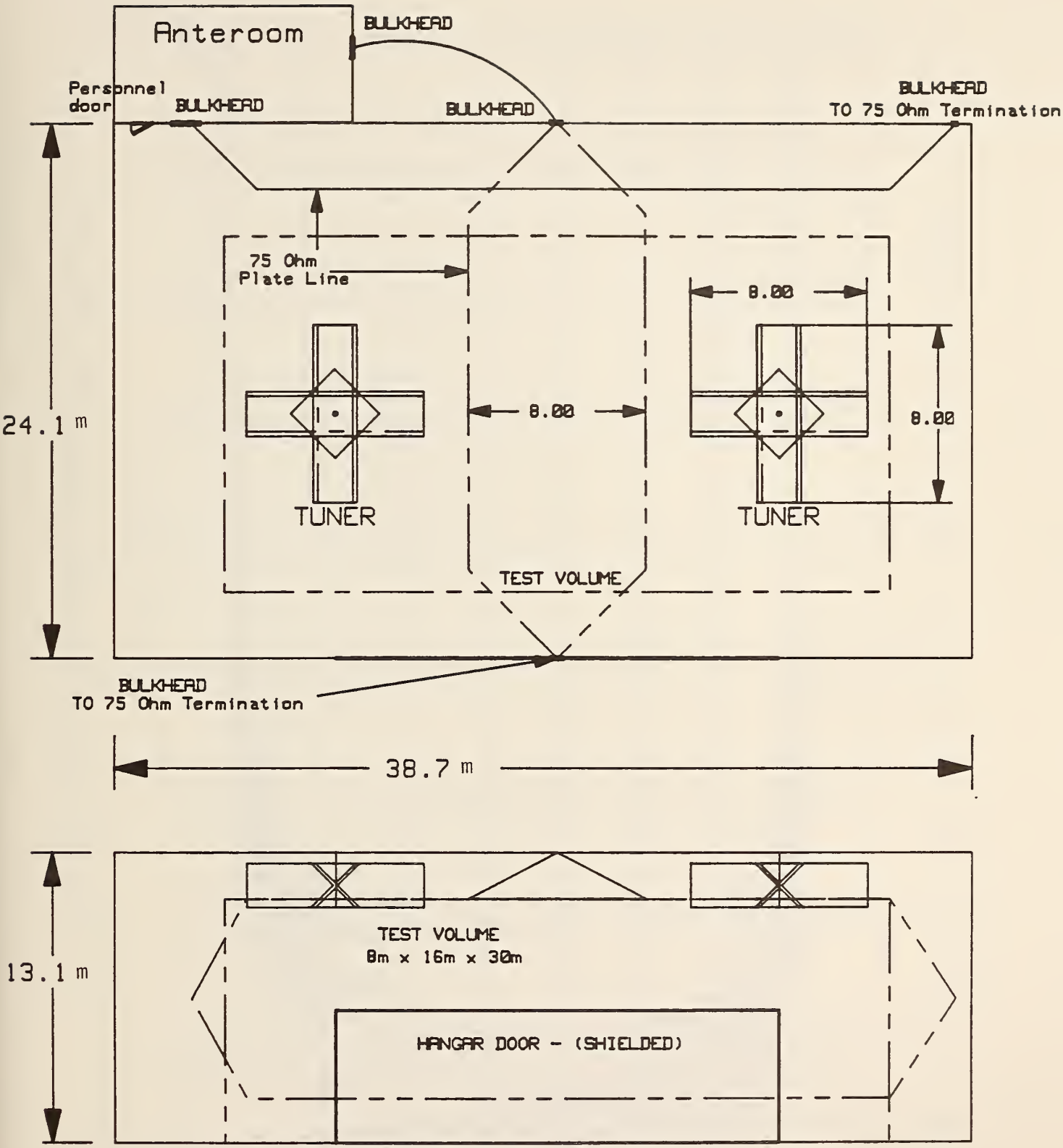

Figure 3.5 Cross-sectional sketches of a proposed full scale TEM/reverberating chamber (13.1 m x 24.1 m x 38.7 m).

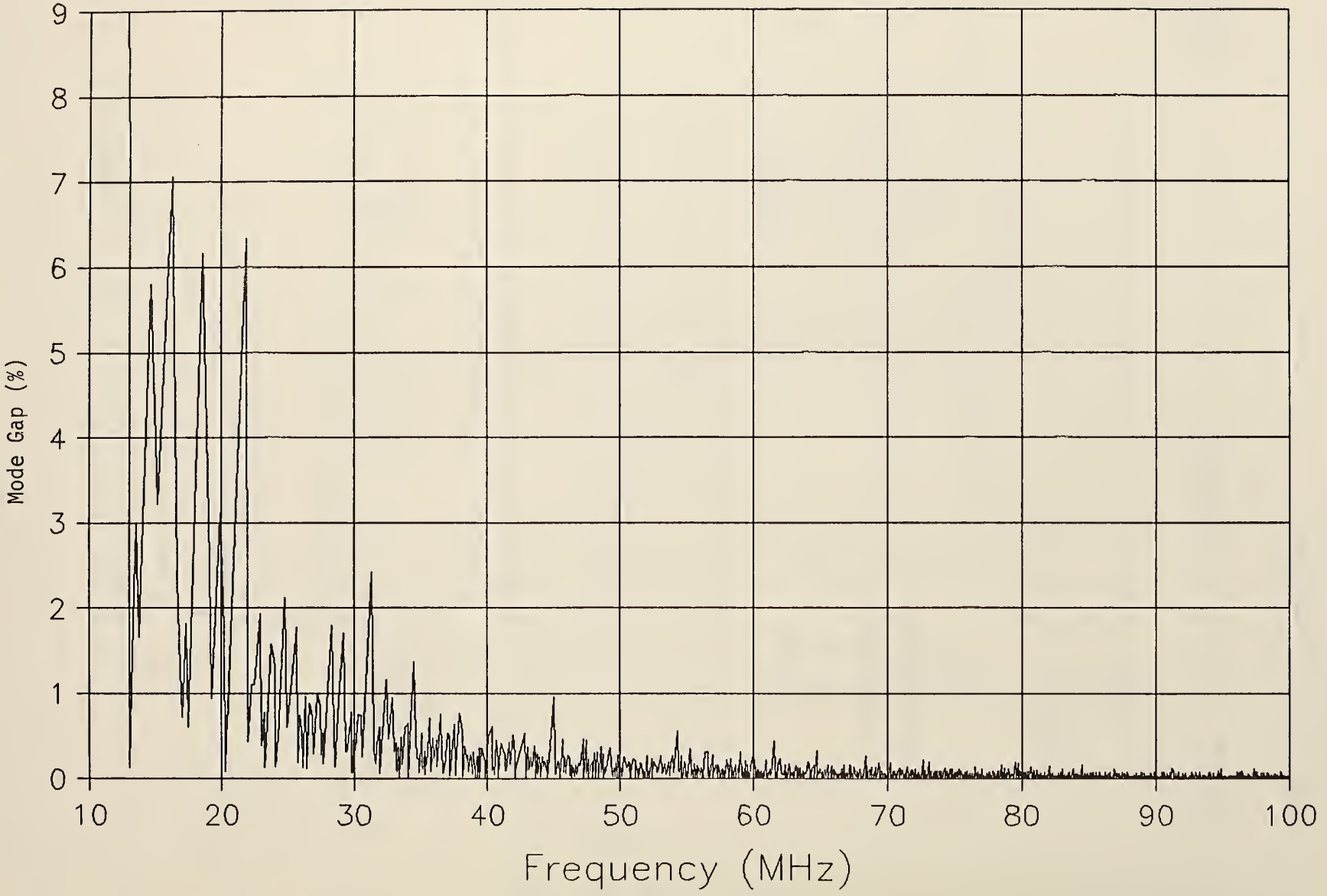

Figure 3.6 Theoretical mode distribution for the proposed full scale TEM/reverberating chamber (13.1 m x 24.1 m x 38.7 m).

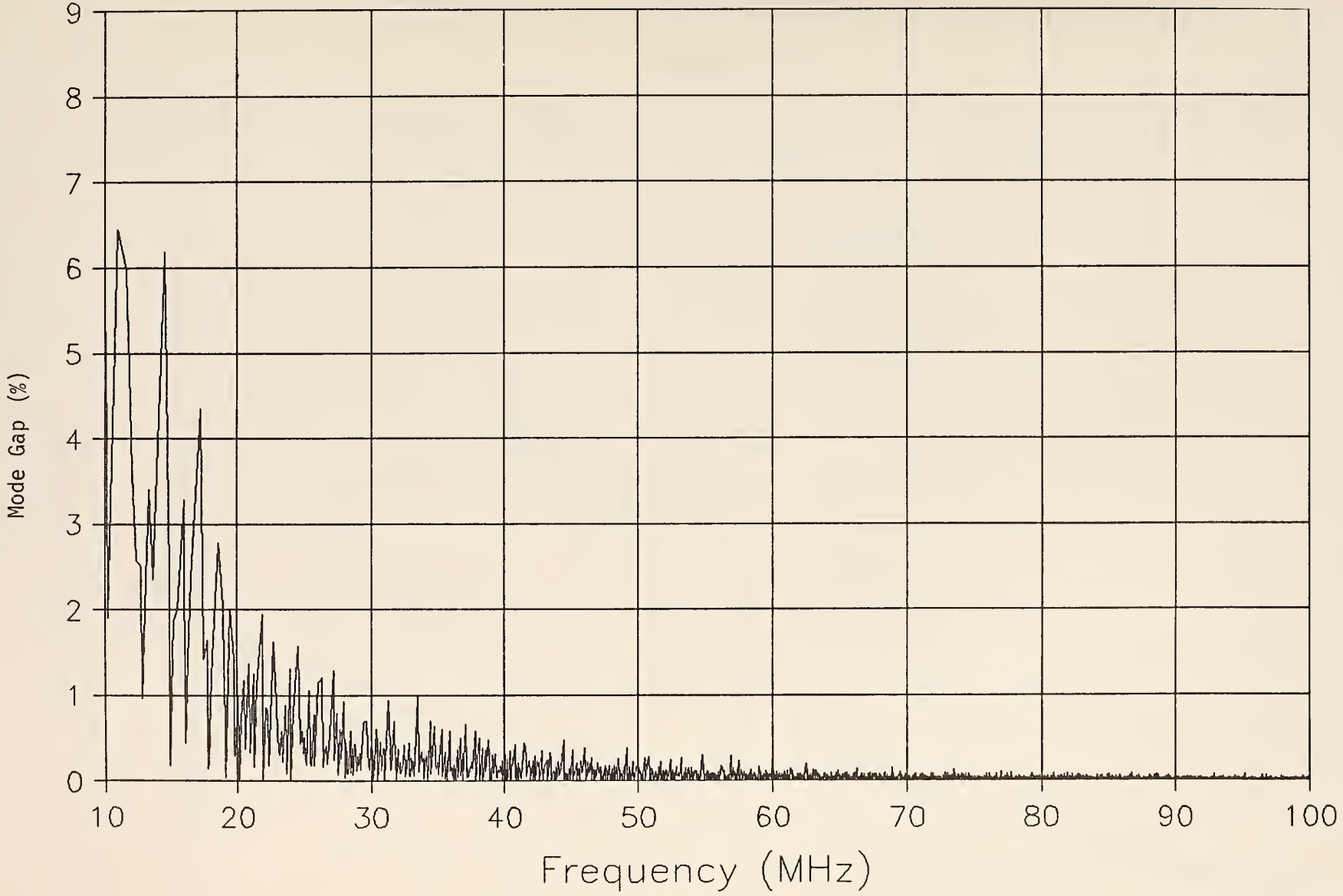

Figure 3.7 Theoretical mode distribution for a large TEM/reverberating chamber (16.2 m x 34.4 m x 38.7 m).

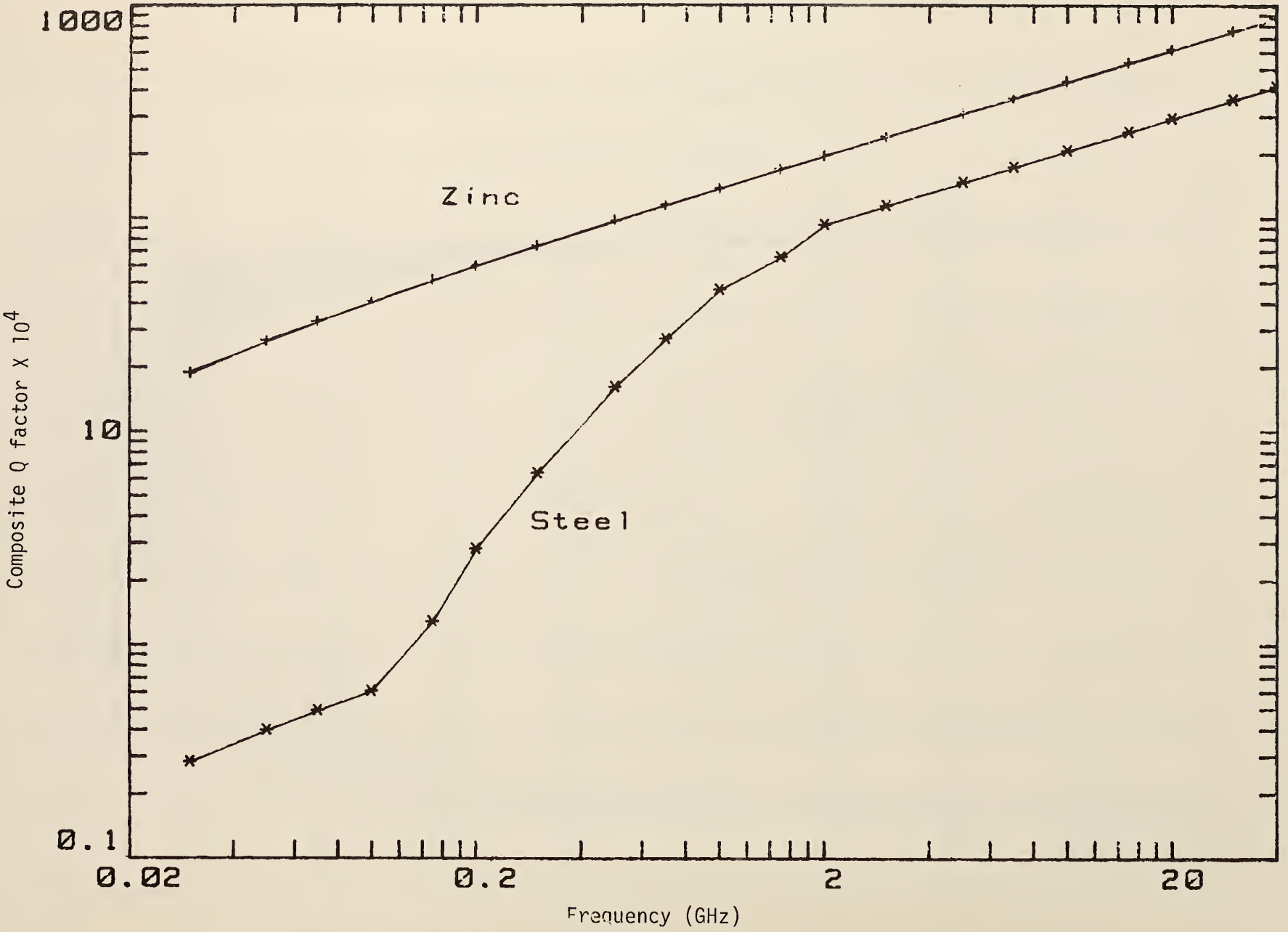

Figure 3.8 Theoretical quality factor of proposed full scale TEM/reverberating chamber (13.1 m x 24.1 m x 38.7 m) assuming: (a) galvanized (zinc) steel and (b) enammel painted (cold rolled) steel.

Table 3.1 Comparison of test fields in a galvanized (zinc finish) steel reverberating chamber of 3.7 m x 5.2 m x 9.8 m with that in an anechoic chamber at 3 m separation distance for same transmitted power. Test volume definition in anechoic chamber is (± 3 dB).

Frequency, MHz	P'_d/P_d, dB	Dimensions, m
100	20.5	X = ± 3.08 Y = ± 1.49 Z_1 = 3 + 1.33 Z_2 = 3 - 0.94
200	25.3	X = ± 3.01 Y = ± 1.44 Z_1 = 3 + 1.25 Z_2 = 3 - 0.89
300	27.9	X = ± 3.00 Y = ± 1.43 Z_1 = 3 + 1.24 Z_2 = 3 - 0.88
500	30.5	X = ± 3.00 Y = ± 1.42 Z_1 = 3 + 1.24 Z_2 = 3 - 0.88

Table 3.2 Comparison of test fields in a galvanized steel reverberating chamber with that in an anechoic chamber for same transmitted power. Separation distances in anechoic chamber = 1 and 3 m.

Frequency GHz	Antenna Gain dB	1 Meter P'_d/P_d , dB	3 Meters P'_d/P_d , dB
0.2	7	13.2	22.8
0.5	9	13.3	22.8
1.0	12	11.2	20.8
2.0	15	8.2	17.8
4.0	15	7.2	16.8
8.0	15	6.2	15.8
12.0	15	5.2	14.8
18.0	15	4.2	13.8

Table 3.3 Test volume for radiated fields in anechoic chamber at 1 m and 3 m separation distances with selected transmitting antenna gain. Test volume definition is based on half-power points of the radiation pattern.

Frequency GHz	Nominal Antenna Gain dB	Half-power beamwidth E-plane degree	Half-power beamwidth H-plane degree	Test Volume Definition R = 1 m Max. dimension of EUT, m $2D^2/\lambda$	Test Volume Definition R = 1 m Max. dimension of EUT, m D^2/λ	Test Volume Definition R = 1 m Dimensions m	Test Volume Definition R = 3 m Max. dimension of EUT, m $2D^2/\lambda$	Test Volume Definition R = 3 m Max. dimension of EUT, m D^2/λ	Test Volume Definition R = 3 m Dimensions m
0.2	7.0	102	64	0.87	1.23	X = ±0.62 Y = ±1.23 Z_1 =1+0.41 Z_2=1-0.29	1.50	2.12	X =±1.87 Y =±3.70 Z_1 =3+1.24 Z_2=3-0.88
1.0	15.0	30	27	0.39	0.55	X =±0.24 Y =±0.27 Z_1=1+0.41 Z_2=1-0.29	0.87	0.95	X =±0.72 Y =±0.80 Z_1=3+1.24 Z_2=3-0.88
12.0	21.0	12	13	0.11	0.16	X =±0.11 Y =±0.11 Z_1=1+0.41 Z_2=1-0.29	0.19	0.27	X =±0.34 Y =±0.32 Z_1=3+1.24 Z_2=3-0.88

Table 3.4 Theoretical mode calculations of frequency and gap between adjoining modes for 1/10 scaled TEM/reverberating chamber, a = 1.31 m, b = 2.41 m, and d = 3.87 m.

Mode #	Indices	Frequency MHz	Gap Size MHz
1	011	73.36	73.36
2	012	99.43	26.07
3	101	120.80	21.37
4	110	130.27	9.47
5	021	130.47	0.20
6	013	131.89	1.42
7	111	135.92	4.03
8	102	138.19	2.28
9	022	146.72	8.53
10	112	151.58	4.86
11	103	163.11	11.53
12	014	167.05	3.94
13	120	169.15	2.10
14	023	170.40	1.24
15	121	173.53	3.14
16	113	174.60	1.07
17	122	186.06	11.46
18	031	190.85	4.79
19	104	192.65	1.80
20	024	198.86	6.21
21	032	202.31	3.45
22	114	202.47	0.17
23	015	203.52	1.04
24	123	205.25	1.73
25	130	219.12	13.87
26	033	220.08	0.96
27	131	222.52	2.44
28	105	225.01	2.49
29	124	229.43	4.42
30	025	230.35	0.92
31	201	232.09	1.74
32	132	232.42	0.33
33	115	233.47	1.05
34	210	237.16	3.69
35	211	240.30	3.14
36	016	240.70	0.39
37	202	241.60	0.90
38	034	242.79	1.19
39	133	248.05	5.26
40	212	249.50	1.45

$z = h_i$	0.0000	1.6635	8.9016	12.7450	13.9815	$z = h_i$	7.7370	12.9909	12.9181	7.4847	0.0000
$3h_i/4$	0.0000	1.7044	2.4606	3.0752	3.6098	$3h_i/4$	3.4774	3.0767	2.5595	1.8392	0.0000
$h_i/2$	0.0000	0.4961	0.7037	0.8619	0.9967	$h_i/2$	1.0000	0.8673	0.7092	0.5023	0.0000
$h_i/4$	0.0000	0.1301	0.0184	0.0225	0.0260	$h_i/4$	0.3052	0.2643	0.2158	0.1526	0.0000
0	0.0000	0.0000	0.0000	0.0000	0.0000	0	0.1596	0.1382	0.1128	0.0798	0.0000
	$y = 0$	$y = a/3$	$y = a/2$	$y=2a/3$	$y = a$		$y = 0$	$y = a/3$	$y = a/2$	$y=2a/3$	$y = a$
	Normalized y components						Normalized z components				

(a) Back Plate (yz plane)

$x = h_i$	0.0000	9.9611	50.0956	71.3390	83.3118	$x = h_i$	47.4000	72.7475	73.1891	43.4334	0.0000
$3h_i/4$	0.0000	4.2225	5.9913	7.3620	8.5287	$3h_i/4$	8.4730	7.3619	6.0307	4.2783	0.0000
$h_i/2$	0.0000	0.5000	0.7071	0.8660	1.0000	$h_i/2$	1.0000	0.8660	0.7071	0.5000	0.0000
$h_i/4$	0.0000	0.0580	0.0820	0.1004	0.1159	$h_i/4$	0.1192	0.1032	0.0843	0.0596	0.0000
0	0.0000	0.0000	0.0000	0.0000	0.0000	0	0.0277	0.0240	0.0196	0.0138	0.0000
	$y = 0$	$y = a/3$	$y = a/2$	$y=2a/3$	$y = a$		$y = 0$	$y = a/3$	$y = a/2$	$y=2a/3$	$y = a$
	Normalized y component						Normalized x component				

(b) Side Plate (yx plane)

Table 3.5 Normalized electric-field components in the 1/10 scaled TEM cell with 100 Ω characteristic impedance, (a) back plate and (b) side plate.

Table 3.6 Relative permeability of cold rolled 11 gauge steel to be used in construction of welded shielded enclosures as a function of frequency.

Frequency (GHz)	Relative Permeability
0.03	1000
0.05	1000
0.10	1000
0.15	350
0.20	100
0.30	30
0.50	8
0.70	4
1.00	2
1.50	1.5
2.00	1
> 2.00	1

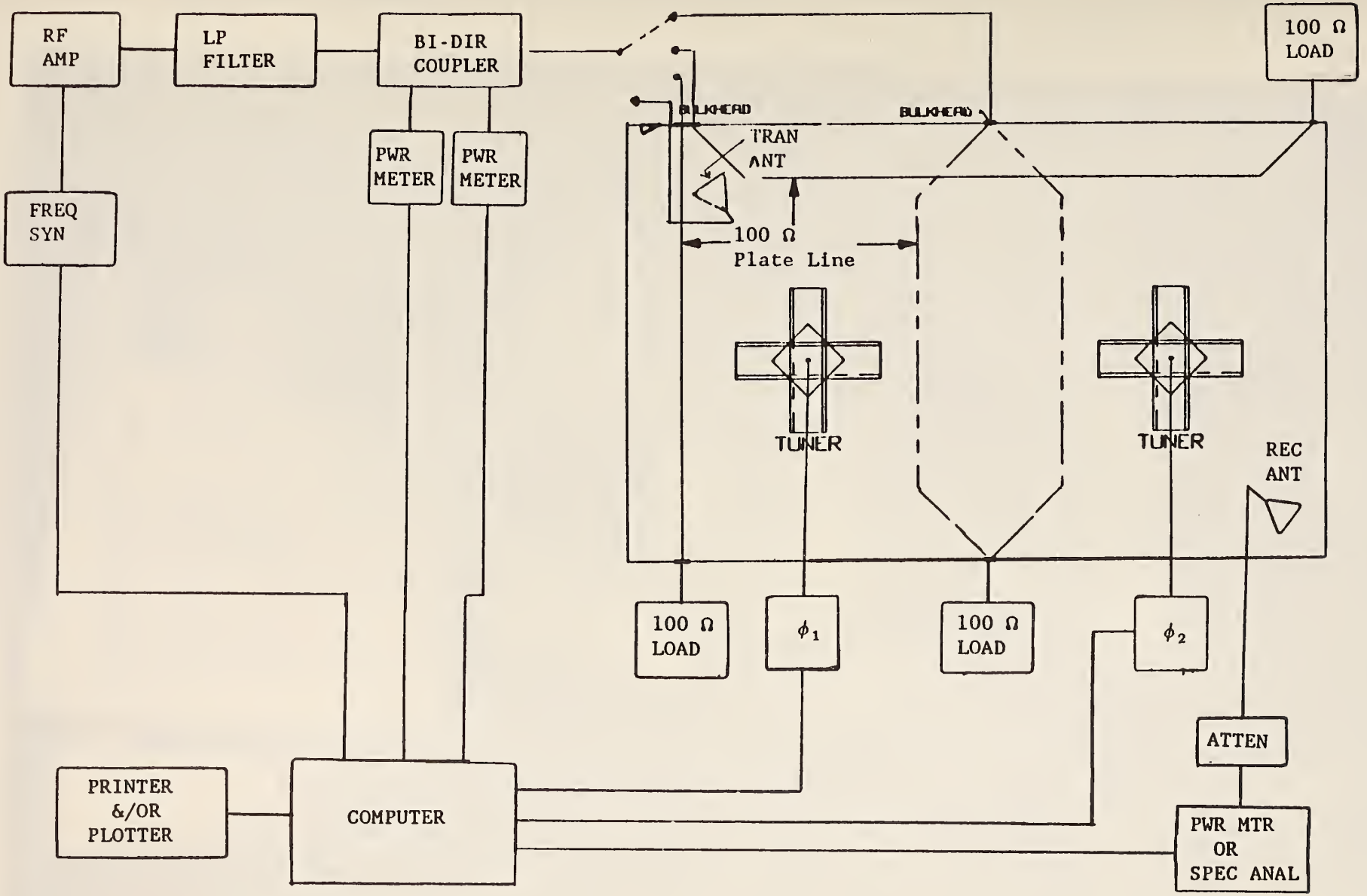

Figure 4.1 Block diagram of the instrumentation used in the cw evaluation of the USAEPG 1/10 scaled TEM/reverberating chamber.

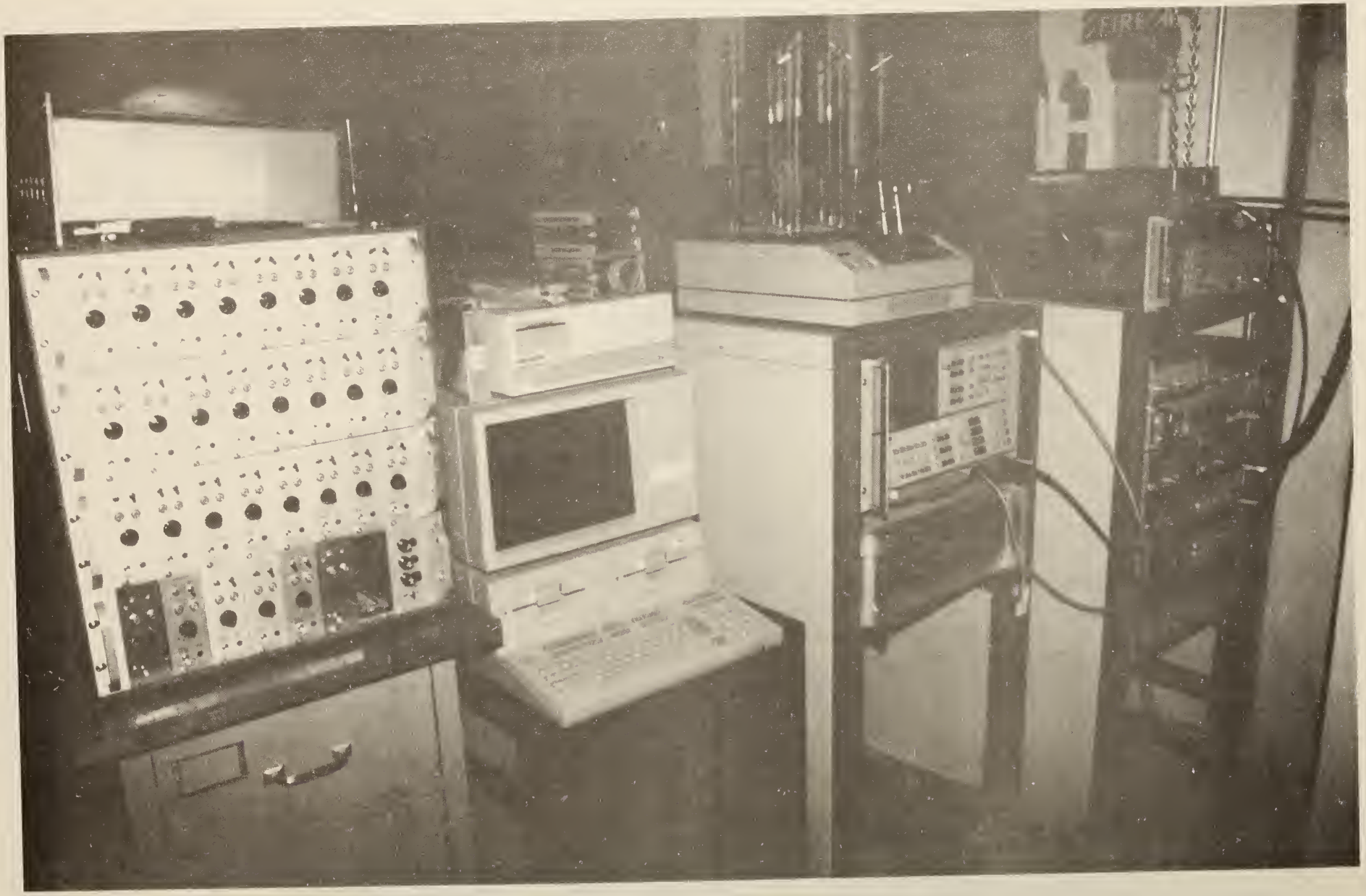

Figure 4.2 Photograph of the NIST equipment used to evaluate the USAEPG 1/10 scale TEM/reverberating chamber.

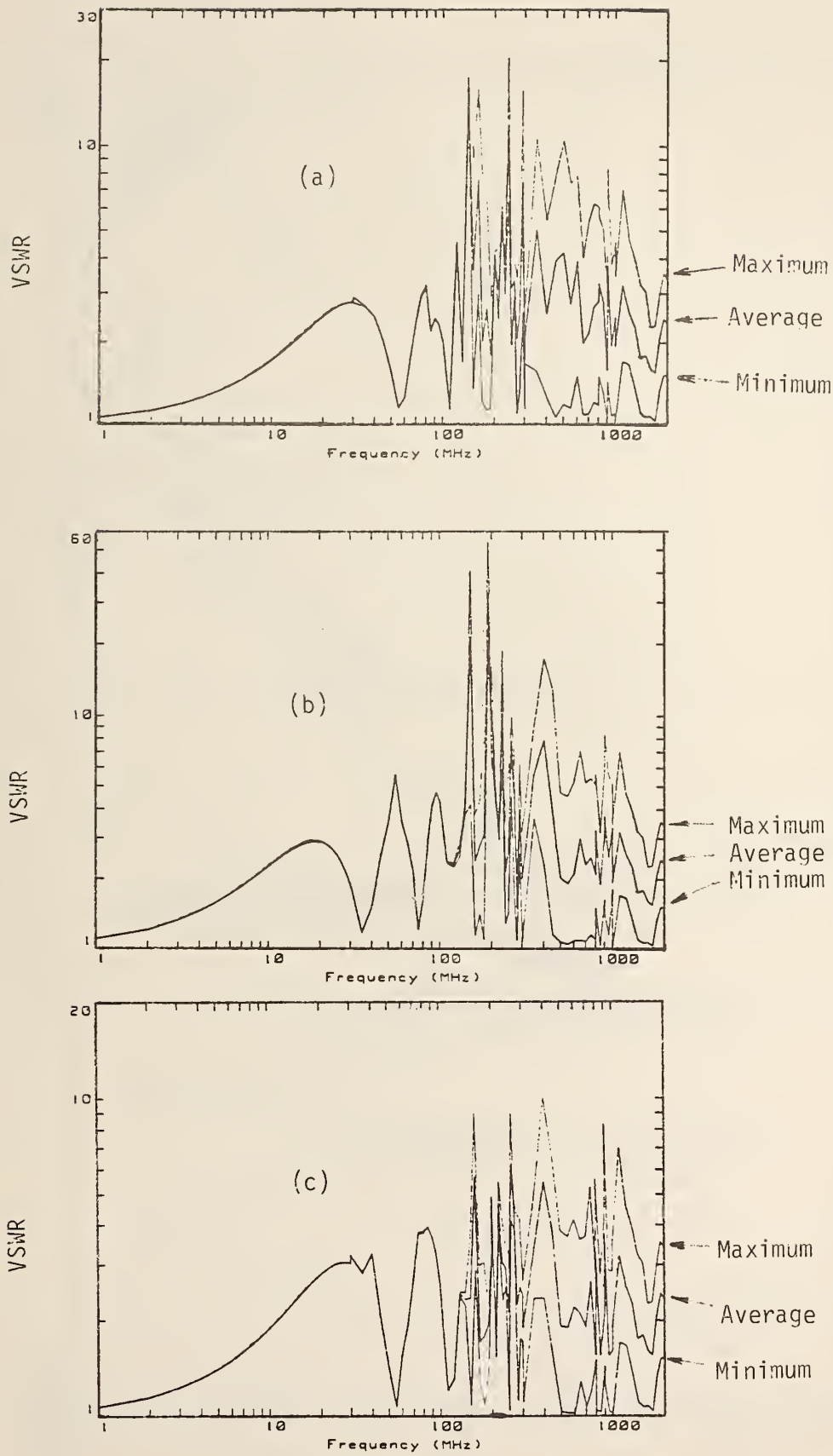

Figure 4.3 Measured VSWR of (a) top plate, (b) back plate, and (c) side plate TEM line, from 1 to 2000 MHz, transmitting into the 1/10 scaled TEM/reverberating chamber.

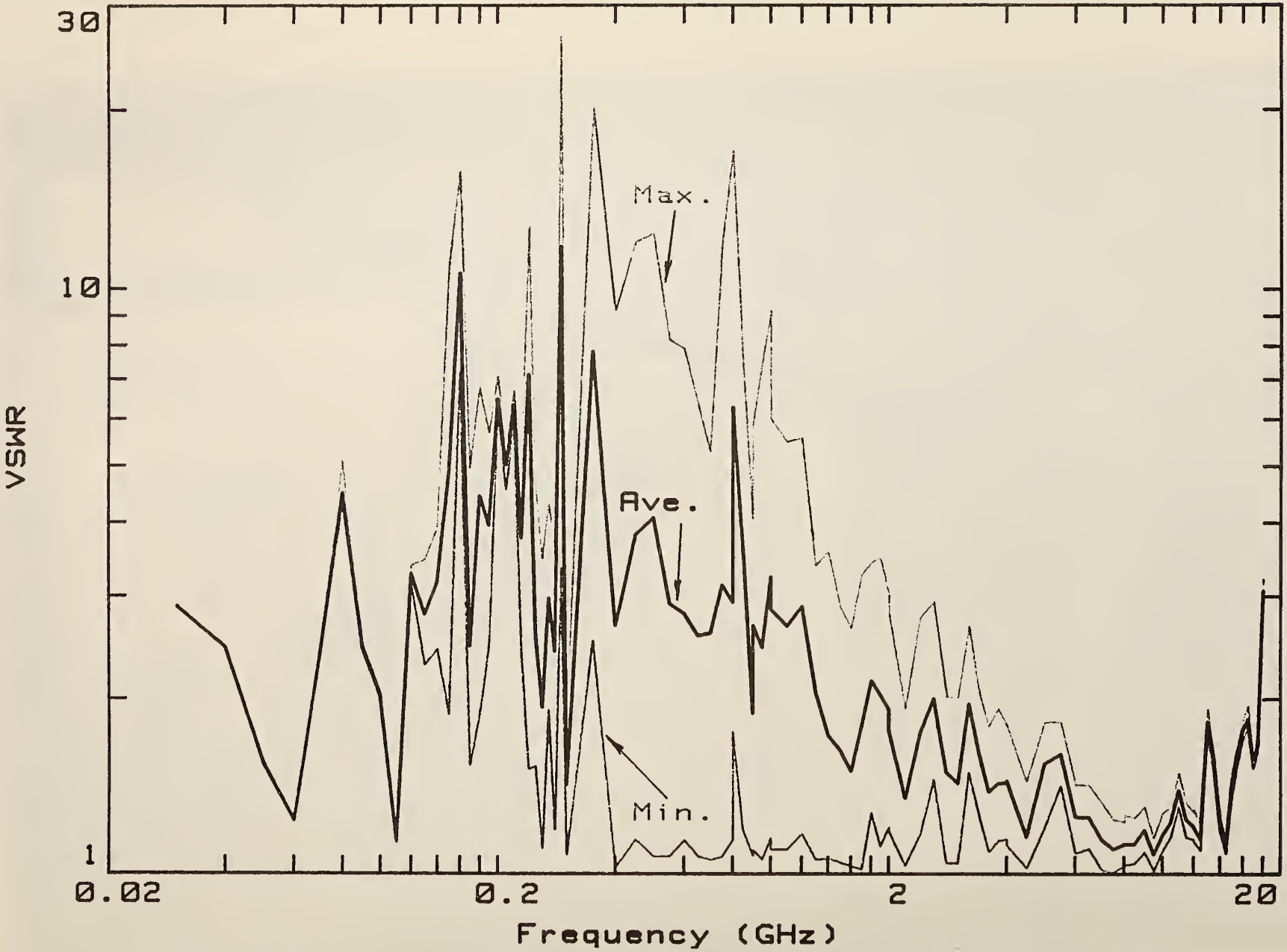

Figure 4.4 Measured composite VSWR of the top plate (0.03 to 1.0 GHz) line and the broadband horn antenna (1.0 to 18.0 GHz) transmitting into the 1/10 scaled TEM/reverberating chamber.

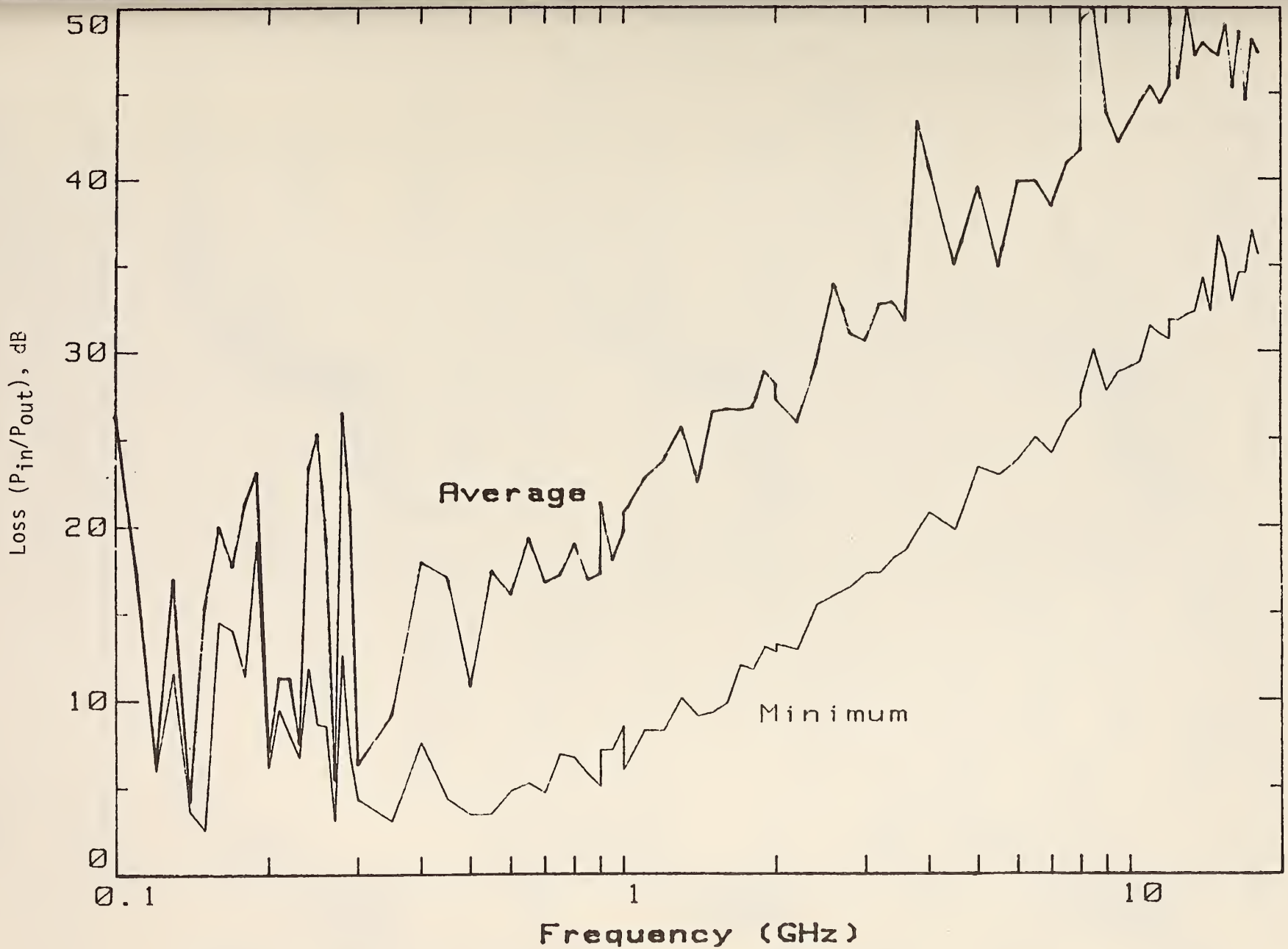

Figure 4.5 Measured coupling efficiency between the top plate line (transmitting) and log periodic antenna (receiving, 0.1 to 1.0 GHz), and the broadband horn antennas (transmitting and receiving, 1.0 to 18.0 GHz) in the 1/10 scaled TEM/reverberating chamber.

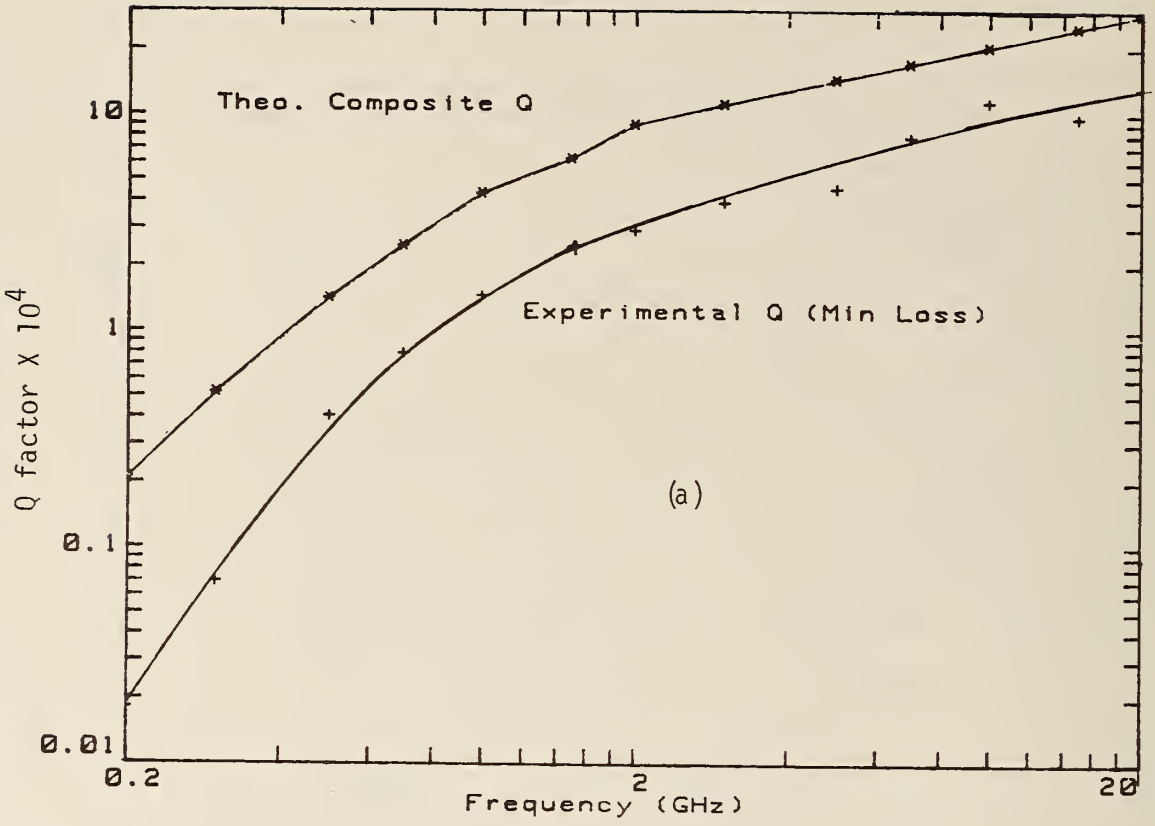

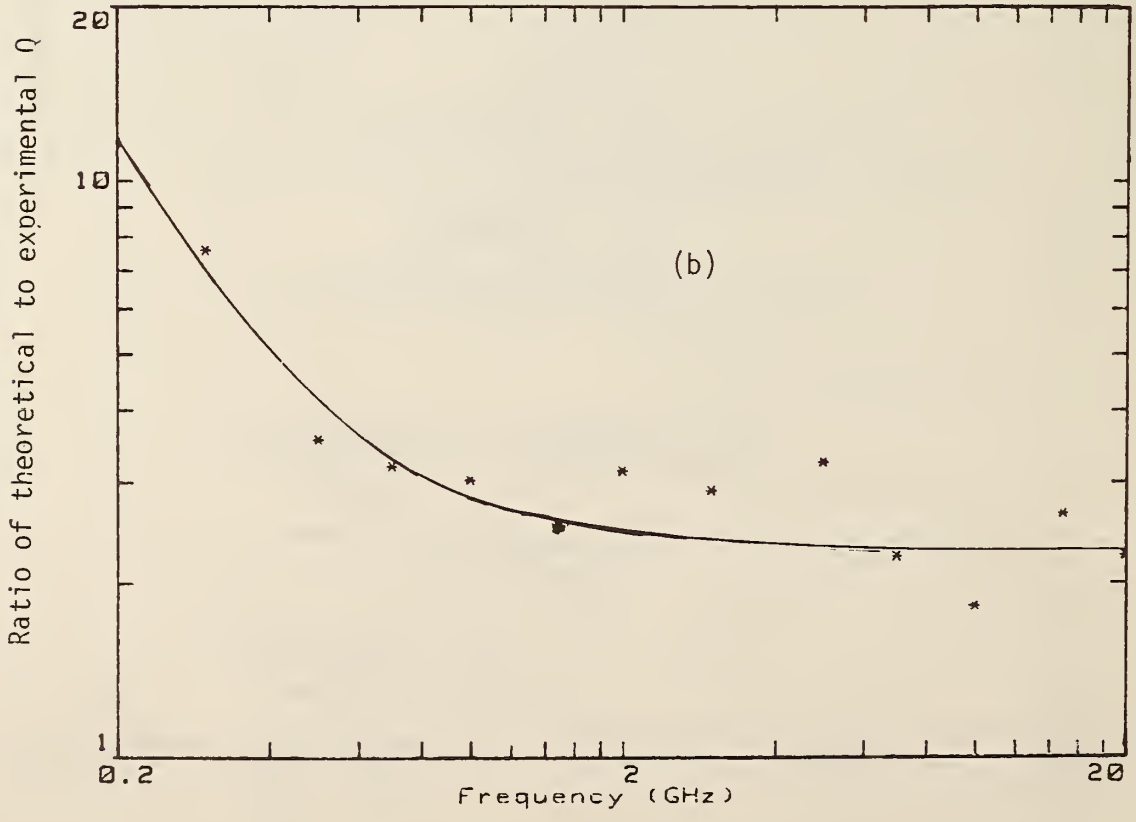

Figure 4.6 (a) Theoretical and experimental Q of the USAEPG 1/10 scaled chamber and (b) ratio of theoretical to experimental Q , 0.2 to 18 GHz .

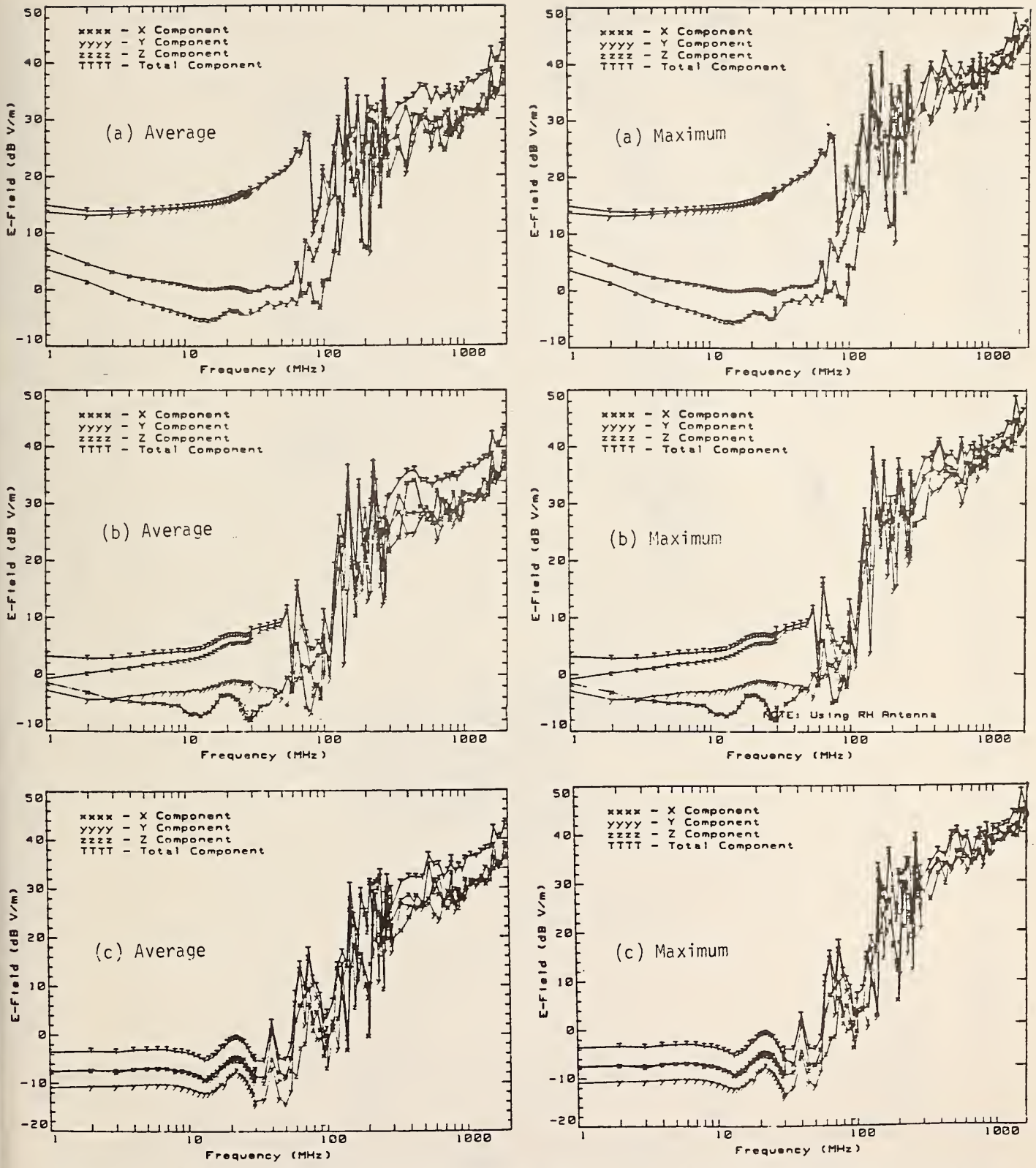

Figure 4.7 E-field components measured at the center of the 1/10 scaled chamber using a NIST isotropic (5 cm dipole) probe (position #3 in figure 4.14) with chamber excited by: (a) top plate, (b) back plate, and (c) side plate. Net input power is 1 W.

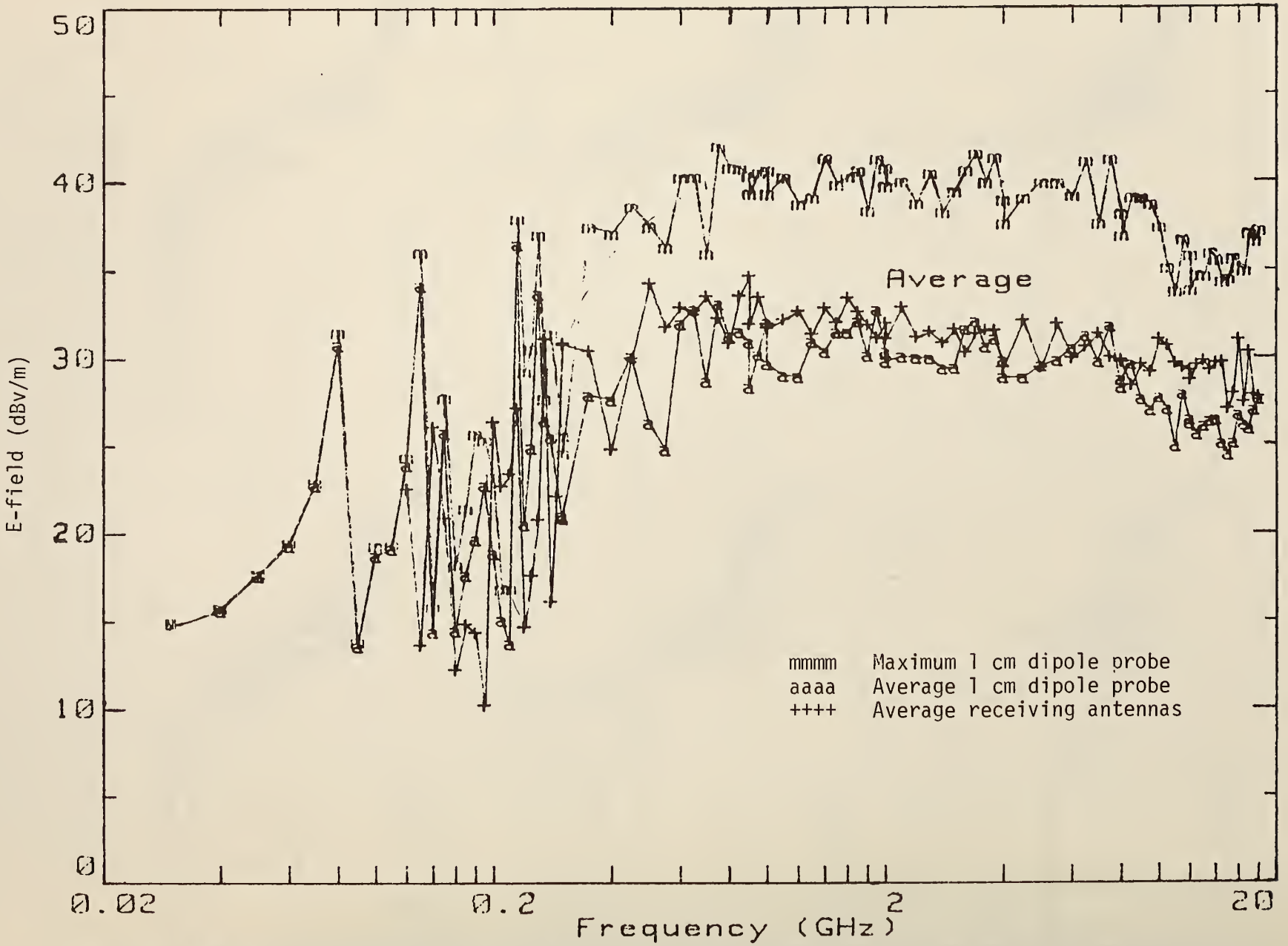

Figure 4.8 Maximum and average E-field in the 1/10 scaled chamber measured with (a) calibrated 1 cm dipole probe (0.03 to 18 GHz), and (b) log-periodic receiving antenna (0.1 to 1 GHz) and boradband horn receiving antenna (1 to 18 GHz). Net transmitted power is 1 W.

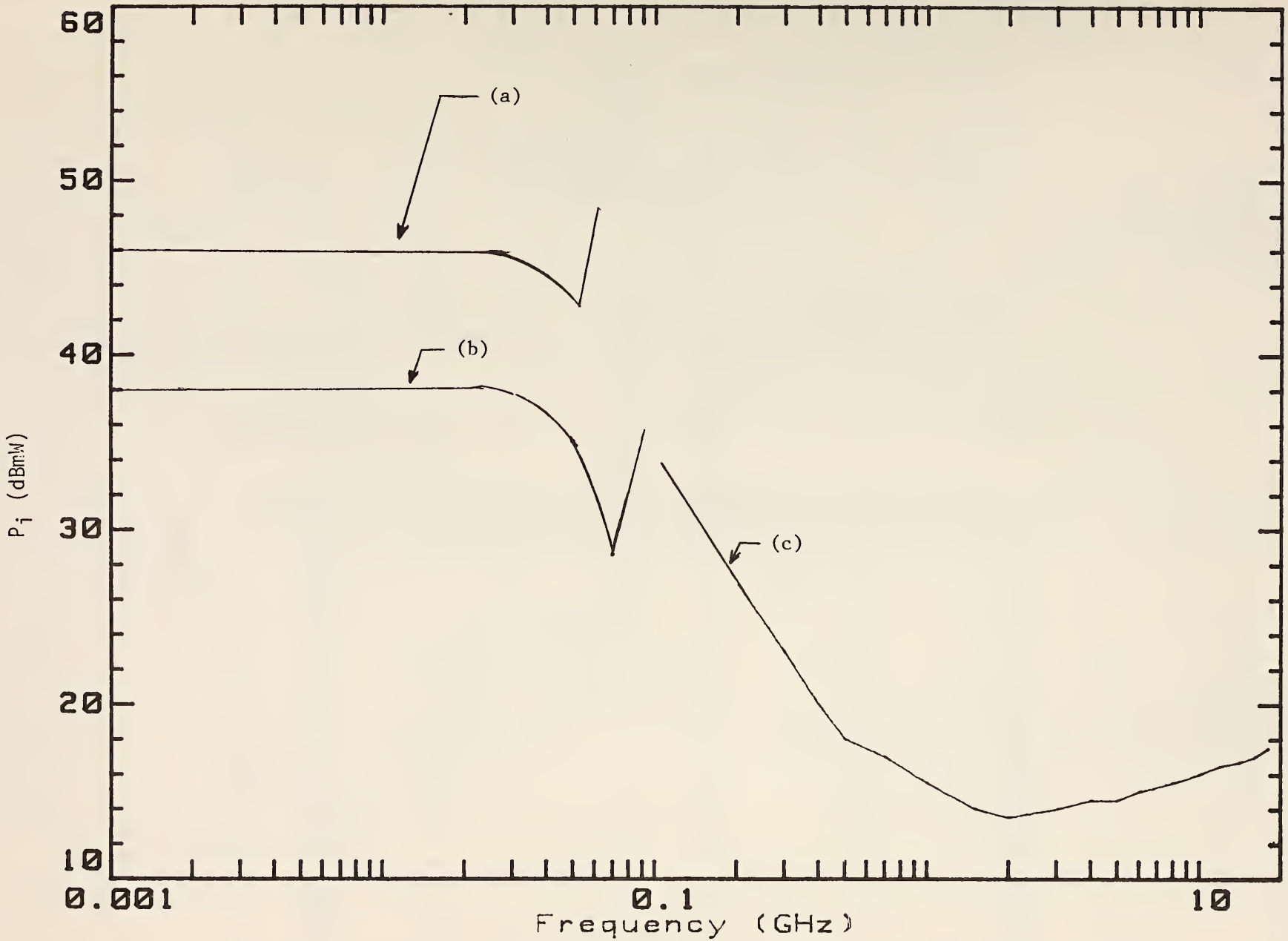

Figure 4.9 Input power required to generate a 20 V/m maximum E-field at the center of the 1/10 scaled chamber using: (a) back plate (Hor. Pol.), (b) top plate (Vert. Pol.), and (c) log periodic and broadband horn.

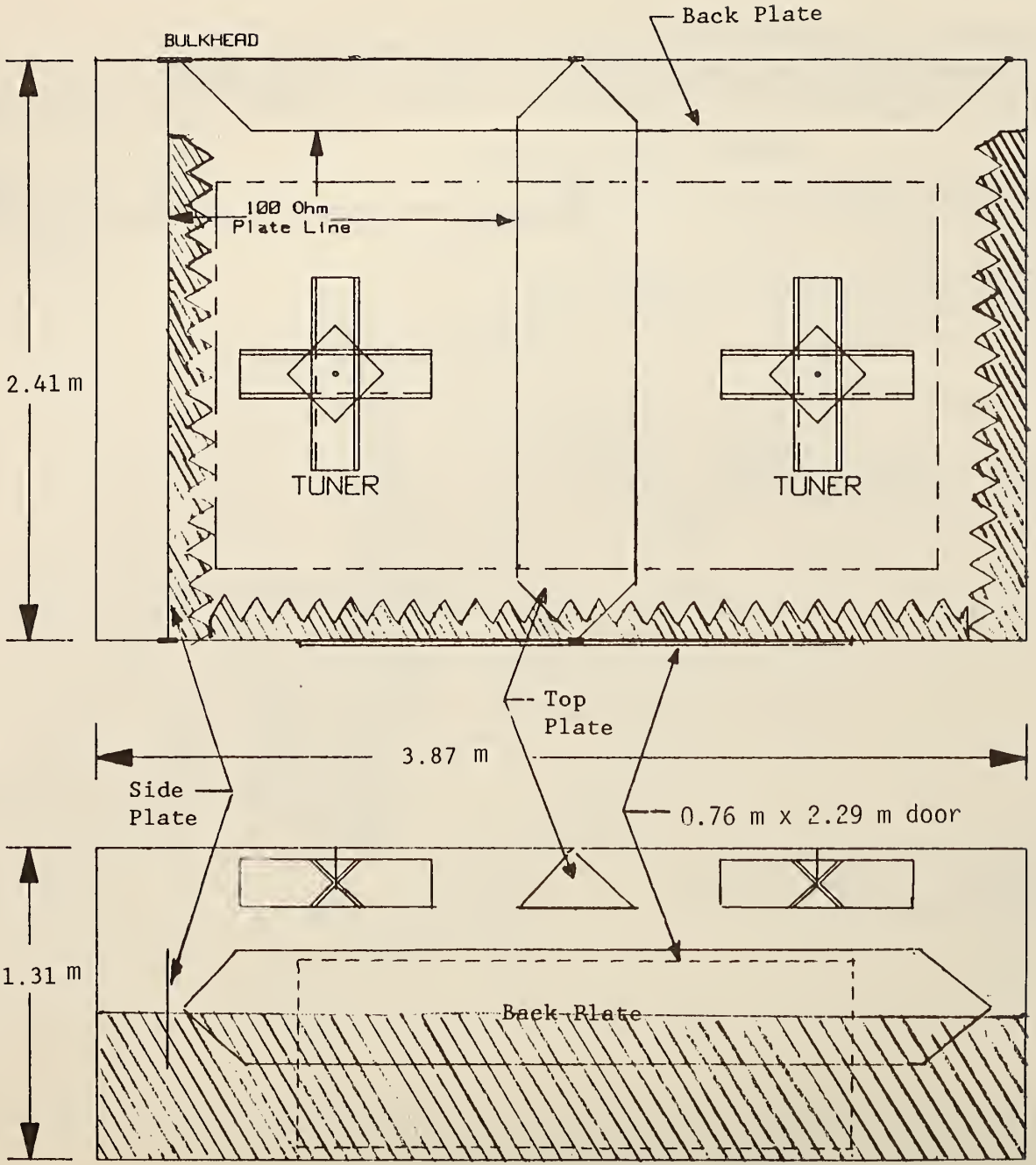

Figure 4.10 Cross sectional sketches of the USAEPG 1/10 scaled TEM/reverberating chamber showing placement of 15 pieces 0.2 m x 0.6 m x 0.6 m rf absorber.

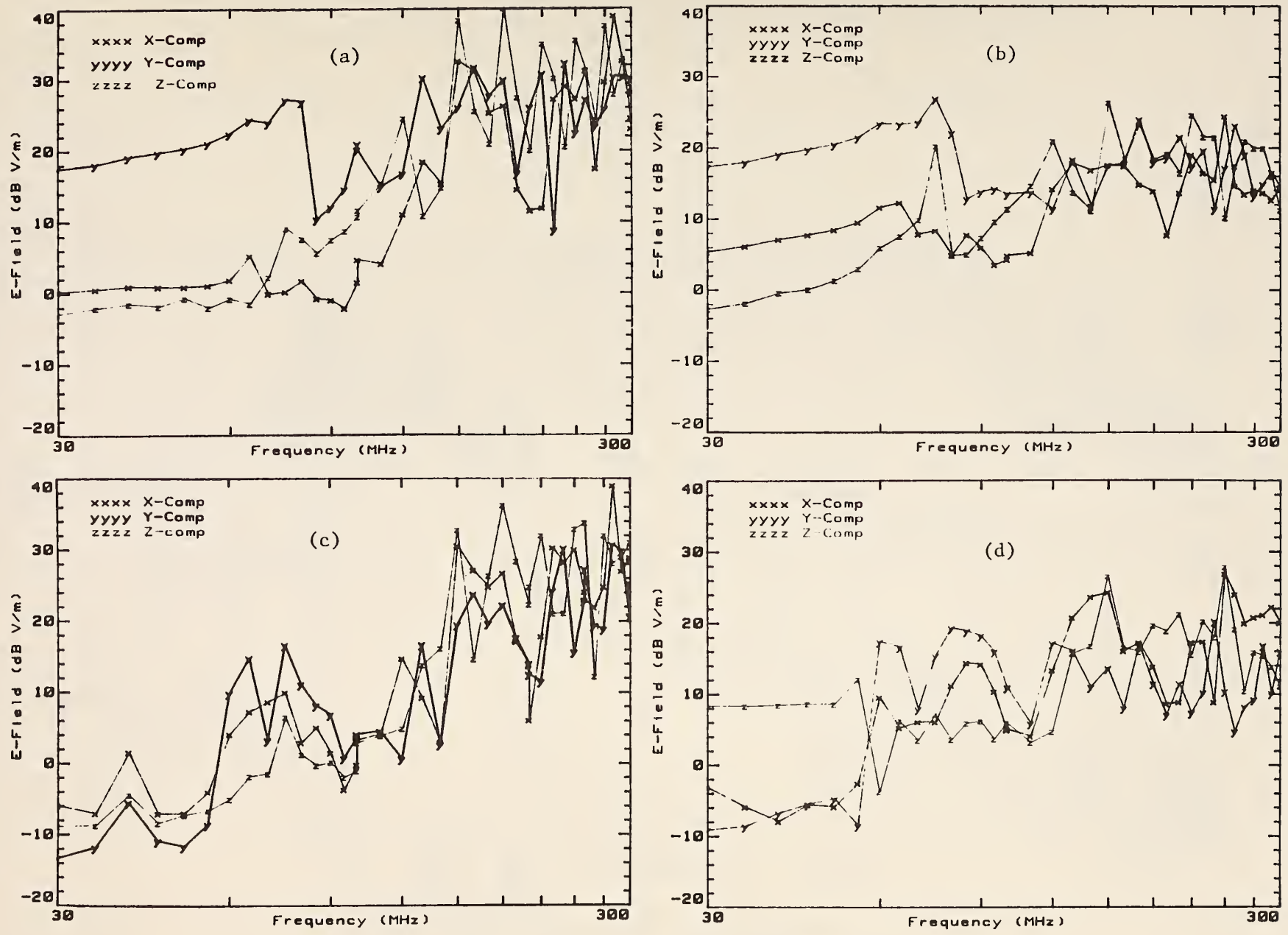

Figure 4.11 Sheet 1 of 2.

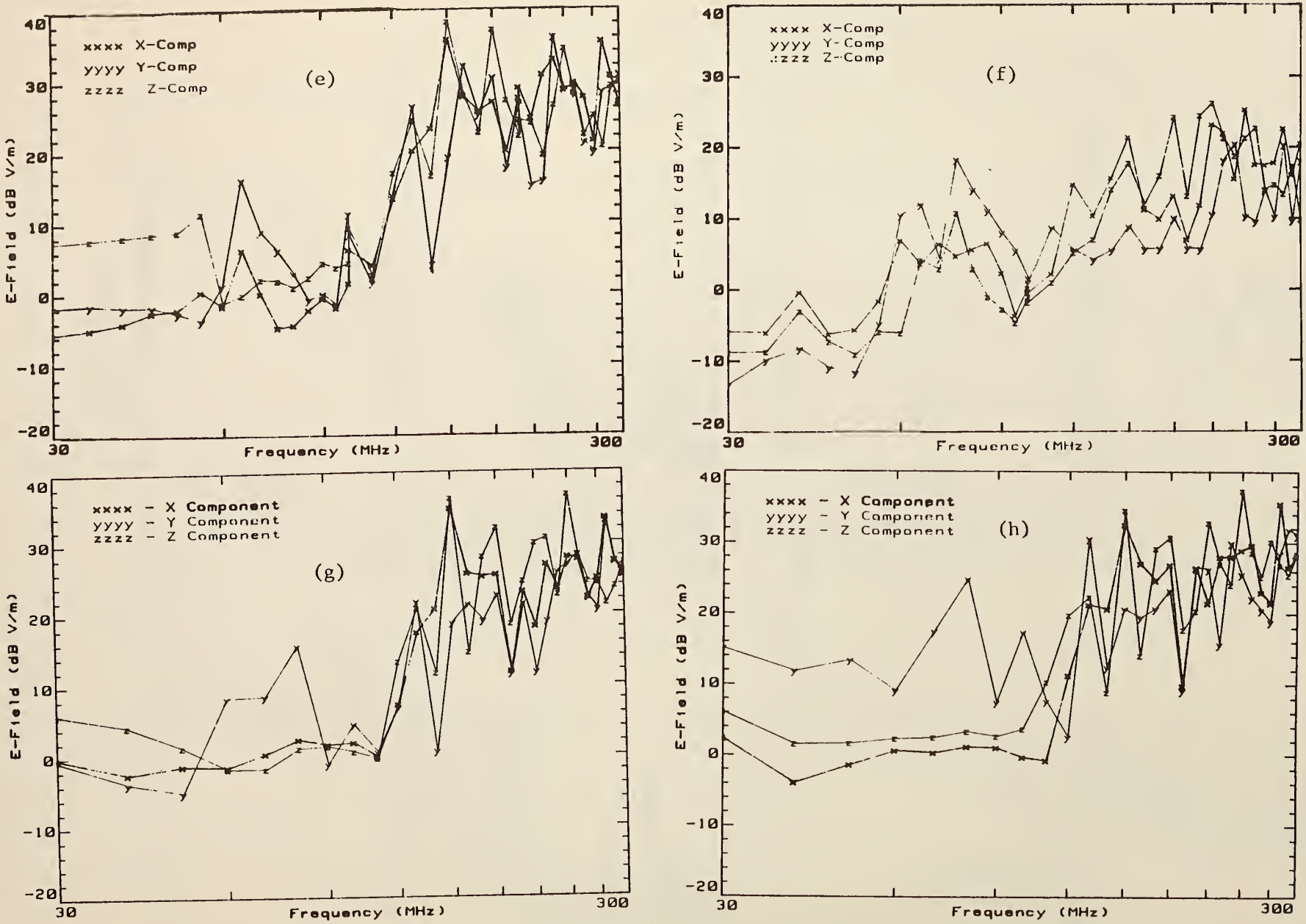

Figure 4.11 Sheet 2 of 2

Figure 4.11 E-field components measured at the center of the 1/10 scaled chamber using a NIST 5 cm dipole, isotropic, probe with the chamber excited by: (a) top plate, no absorber; (b) top plate, absorber loaded; (c) back plate, no absorber; (d) back plate, absorber loaded; (e) side plate, no absorber; (f) side plate, absorber loaded; (g) back and side plates driven simultaneously in phase, no absorber; and (h) all three plates driven simultaneously in phase, no absorber.

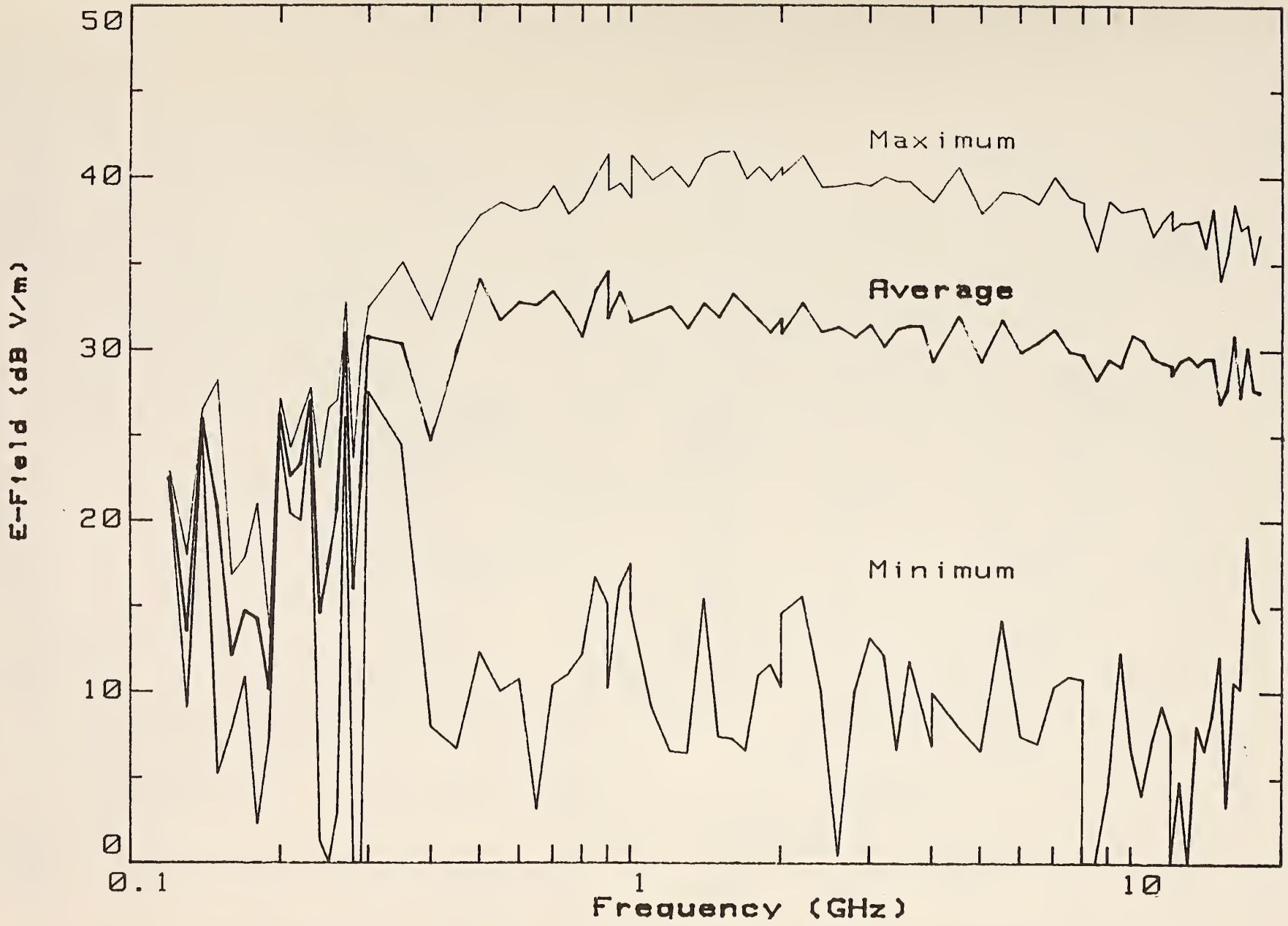

Figure 4.12 E fields calculated from receiving antenna power measurements in the 1/10 scaled chamber with 1 W net input power. Same transmitting and receiving antennas used as in figure 4.8.

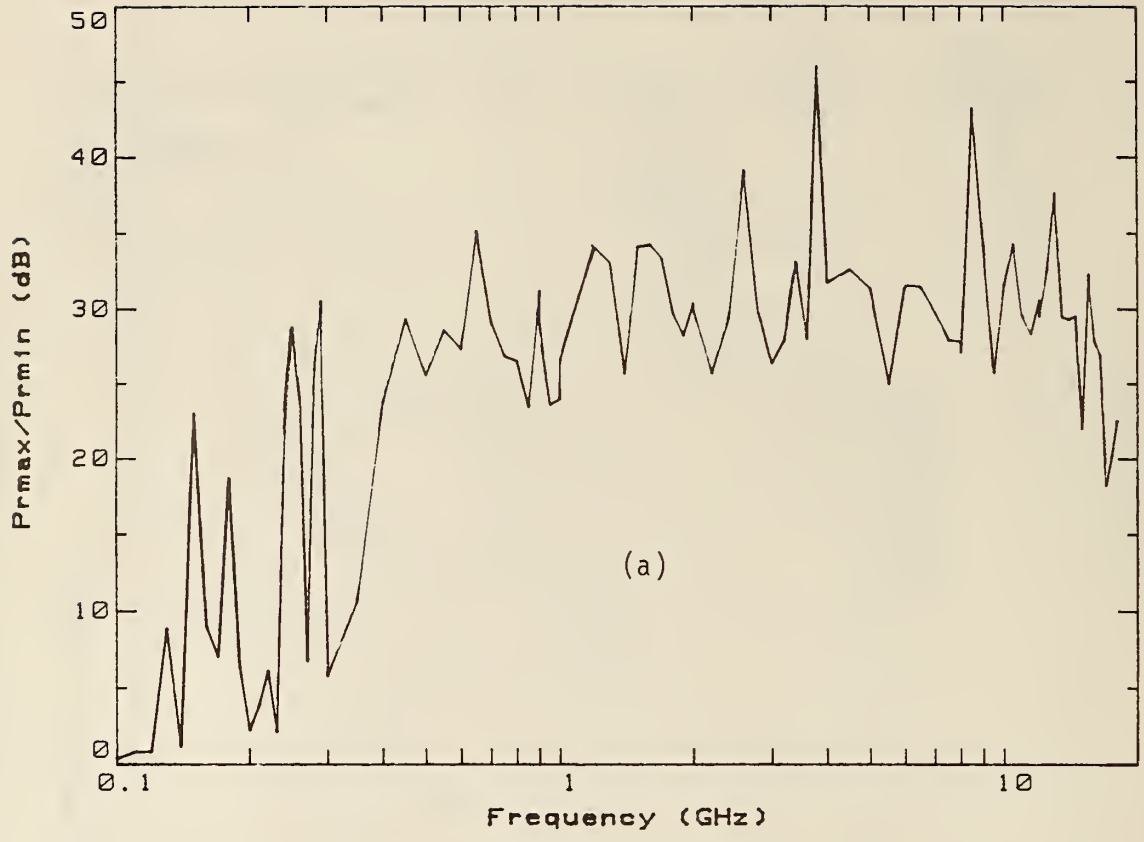

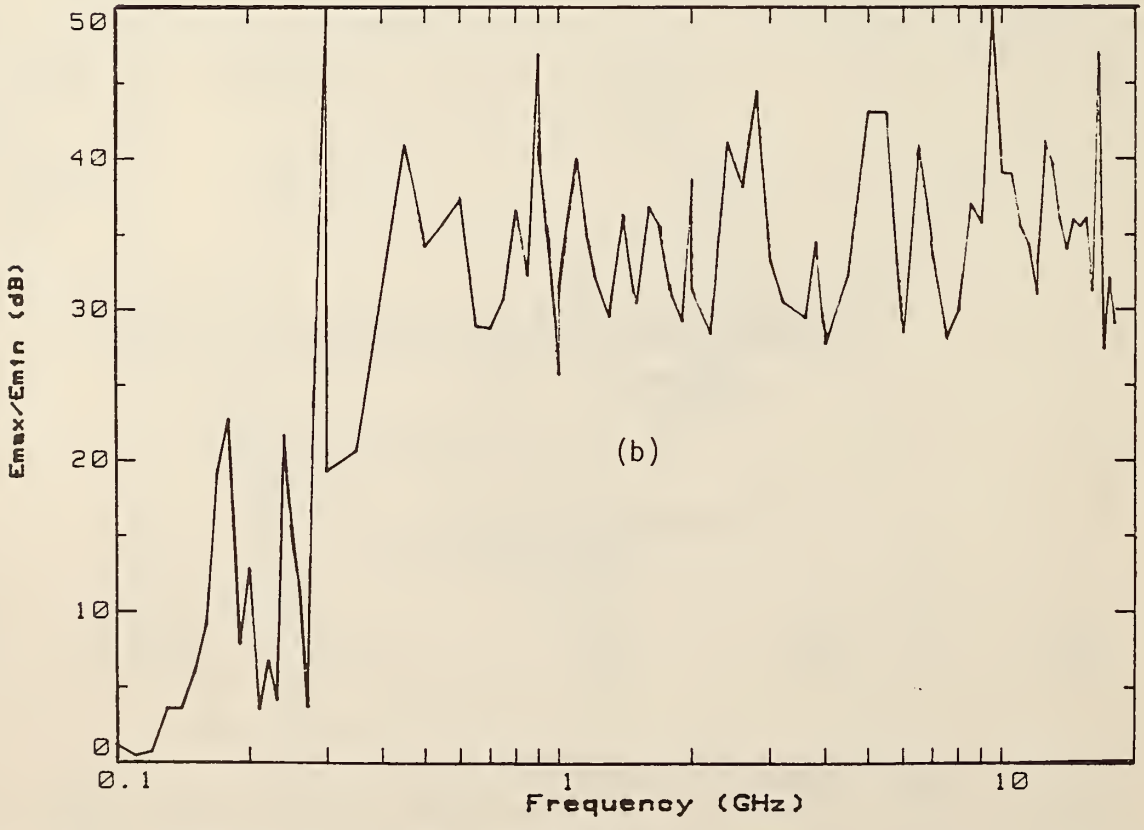

Figure 4.13 Measured tuner effectiveness in the 1/10 scaled chamber using: (a) receiving antenna power measurements (same receiving antennas as figure 4.5), and (b) 1 cm dipole probe E-field measurements.

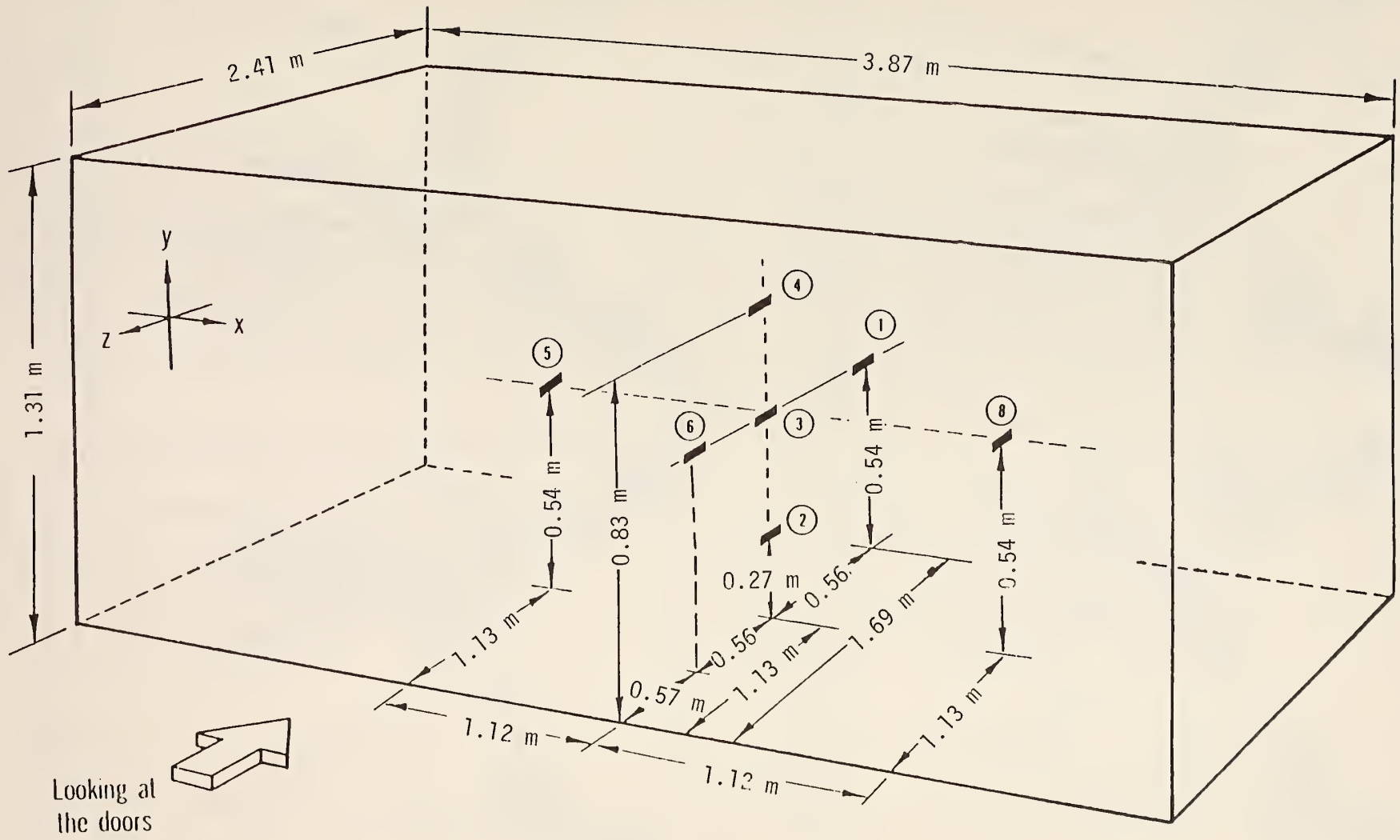

Figure 4.14 Cross sectional sketch of the USAEPG 1/10 scaled TEM/reverberating chamber showing placement of isotropic probes for measuring spatial E-field uniformity.

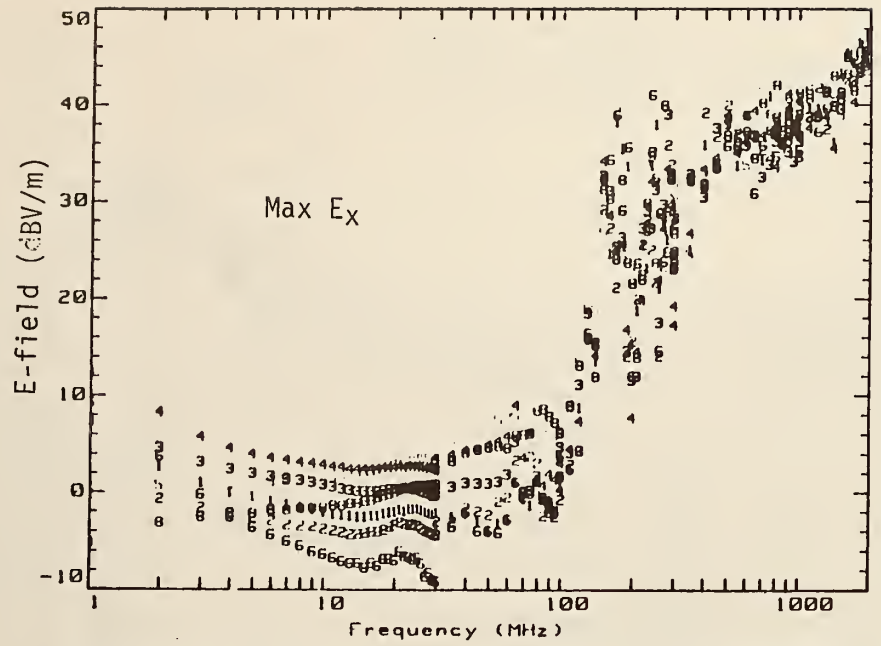
Max E_x
E-field (dBV/m)
Frequency (MHz)

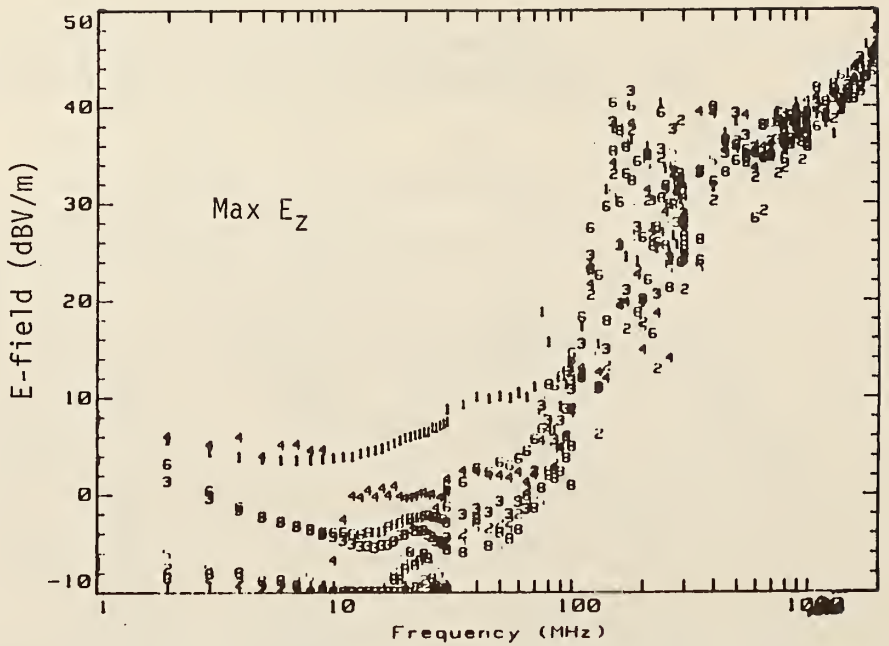
Max E_z
E-field (dBV/m)
Frequency (MHz)

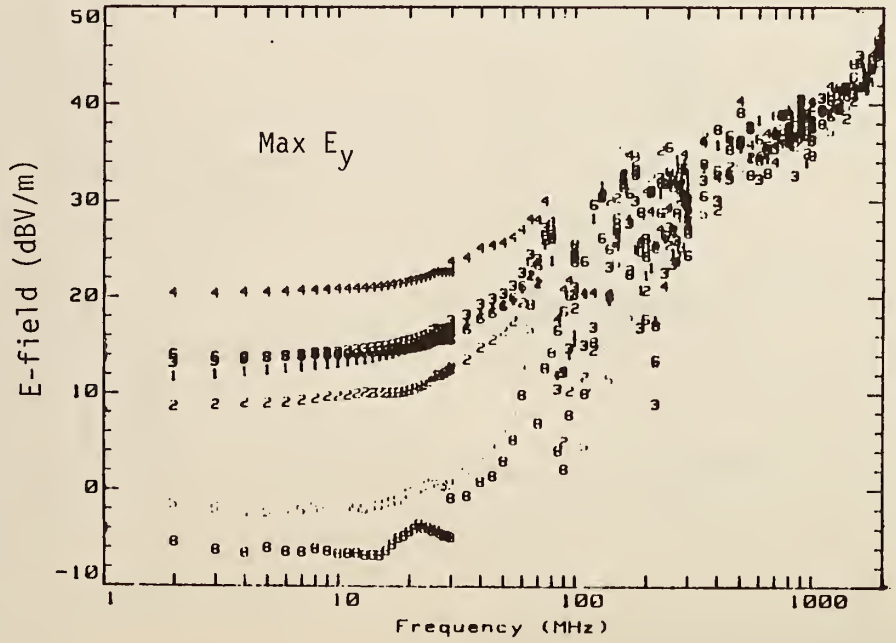
Max E_y
E-field (dBV/m)
Frequency (MHz)

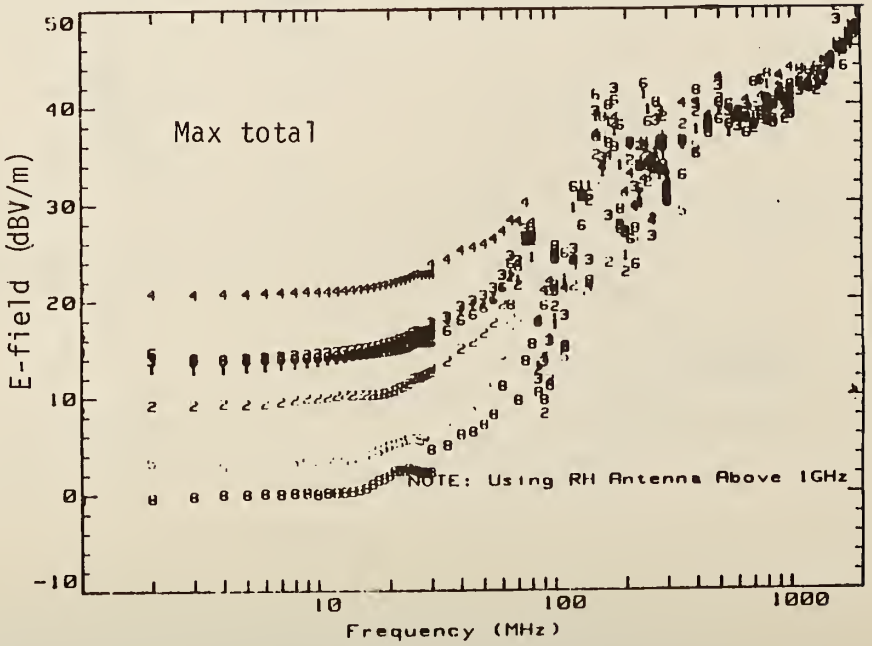
Max total
NOTE: Using RH Antenna Above 1GHz
E-field (dBV/m)
Frequency (MHz)

Figure 4.15 (a)

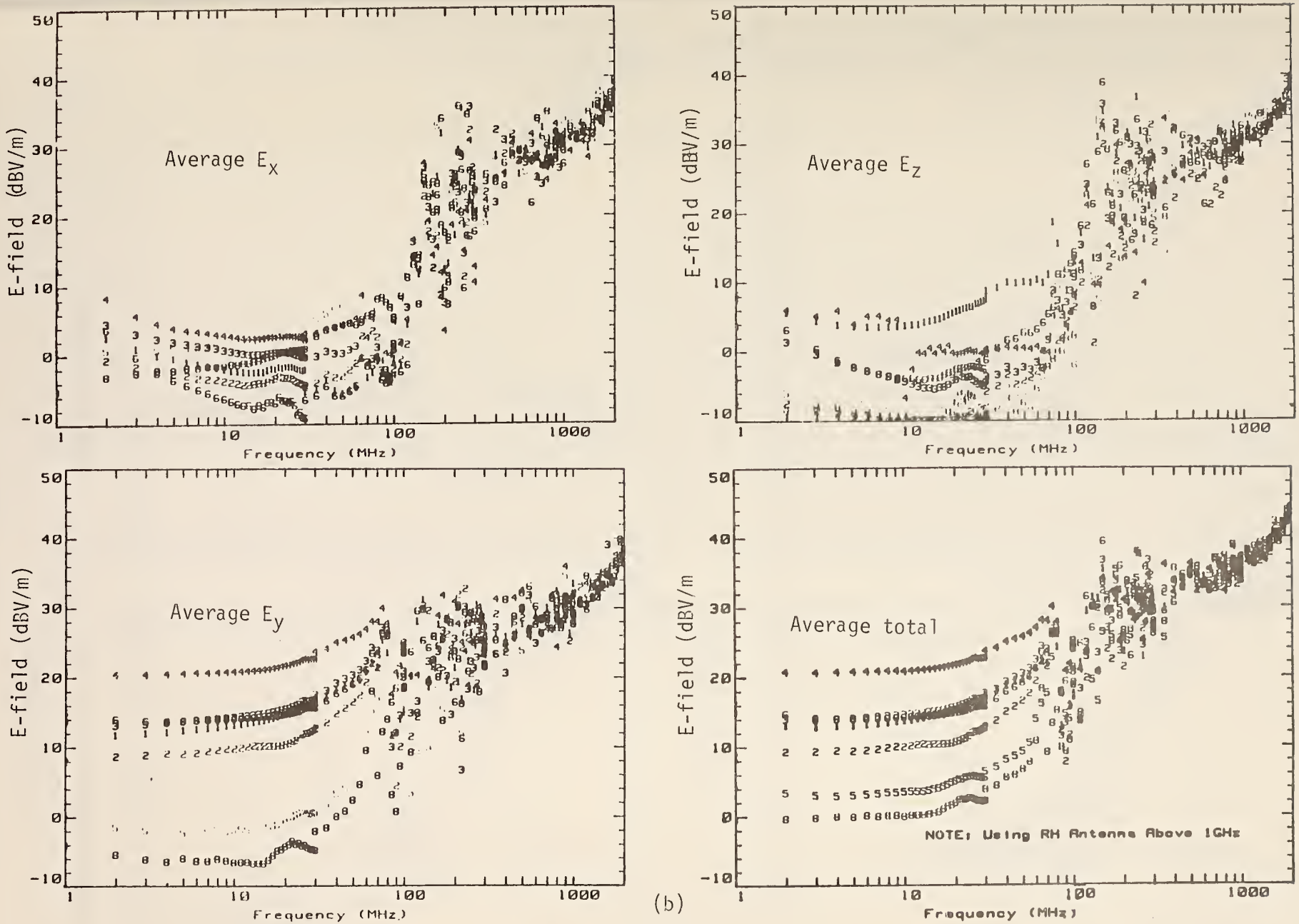

Figure 4.15 Spatial distribution of E-field components in the 1/10 scaled chamber measured with 7 NIST isotropic probes (5 cm dipoles) when transmitting 1 W net input power from top plate: (a) maximum and (b) average values.

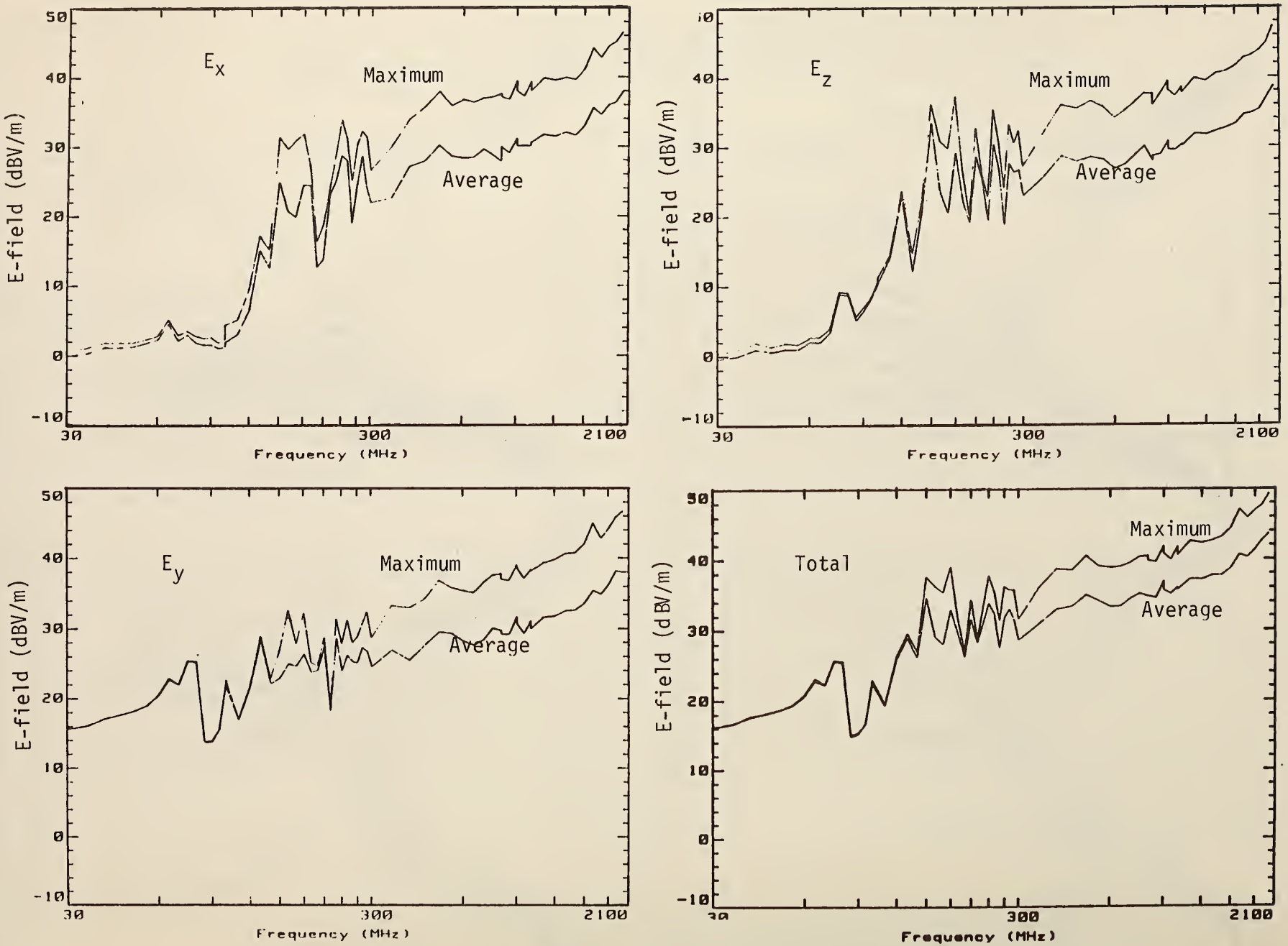

Figure 4.16 Smoothed average and maximum of measured E-field components in the 1/10 scaled chamber generated by the top plate with 1 W net input power, determined from data in figure 4.15.

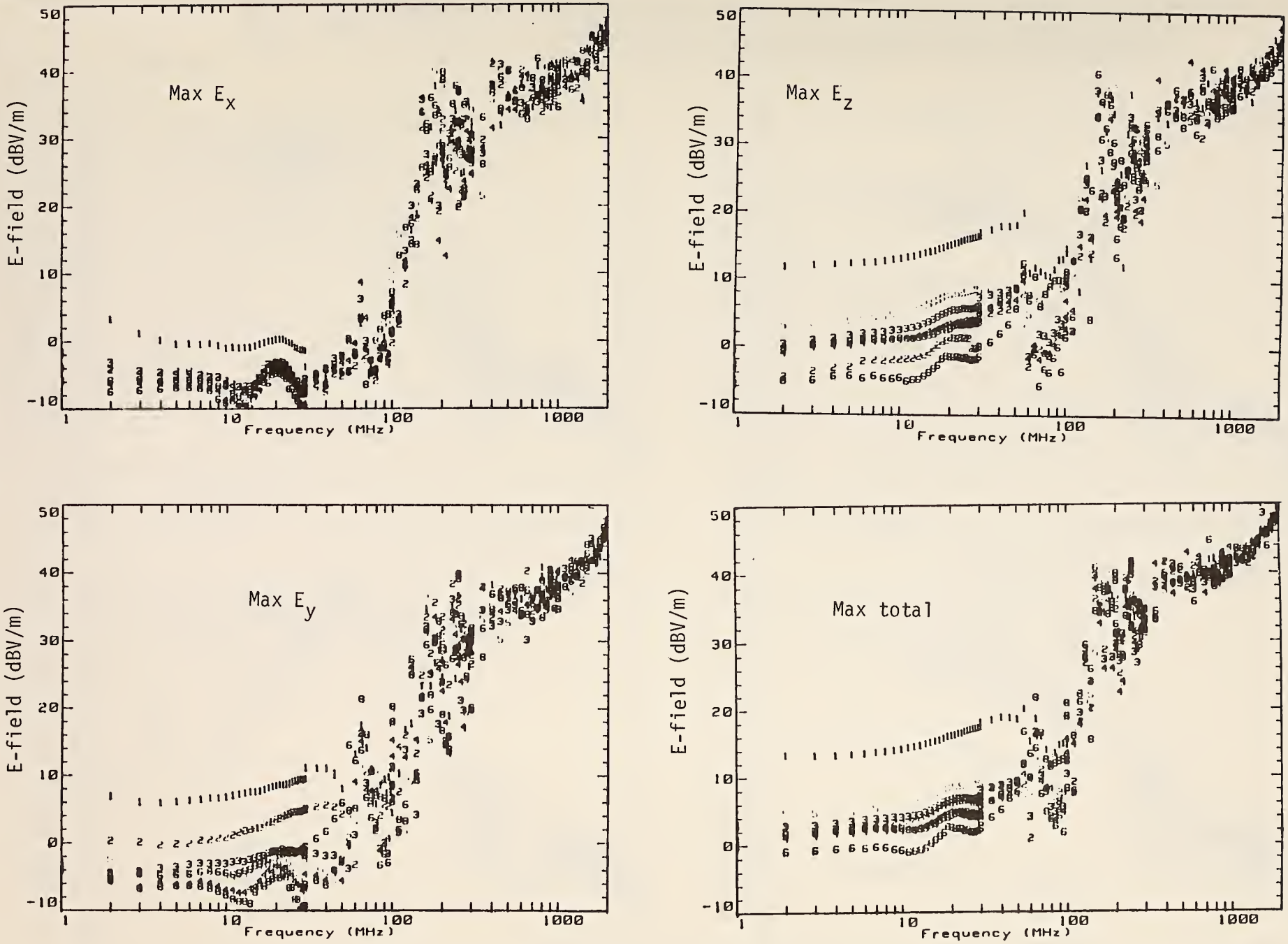
Max E_x
Max E_z
Max E_y
Max total
E-field (dBV/m)
Frequency (MHz)
50
40
30
20
10
0
-10
1
10
100
1000

Figure 4.17 (a)

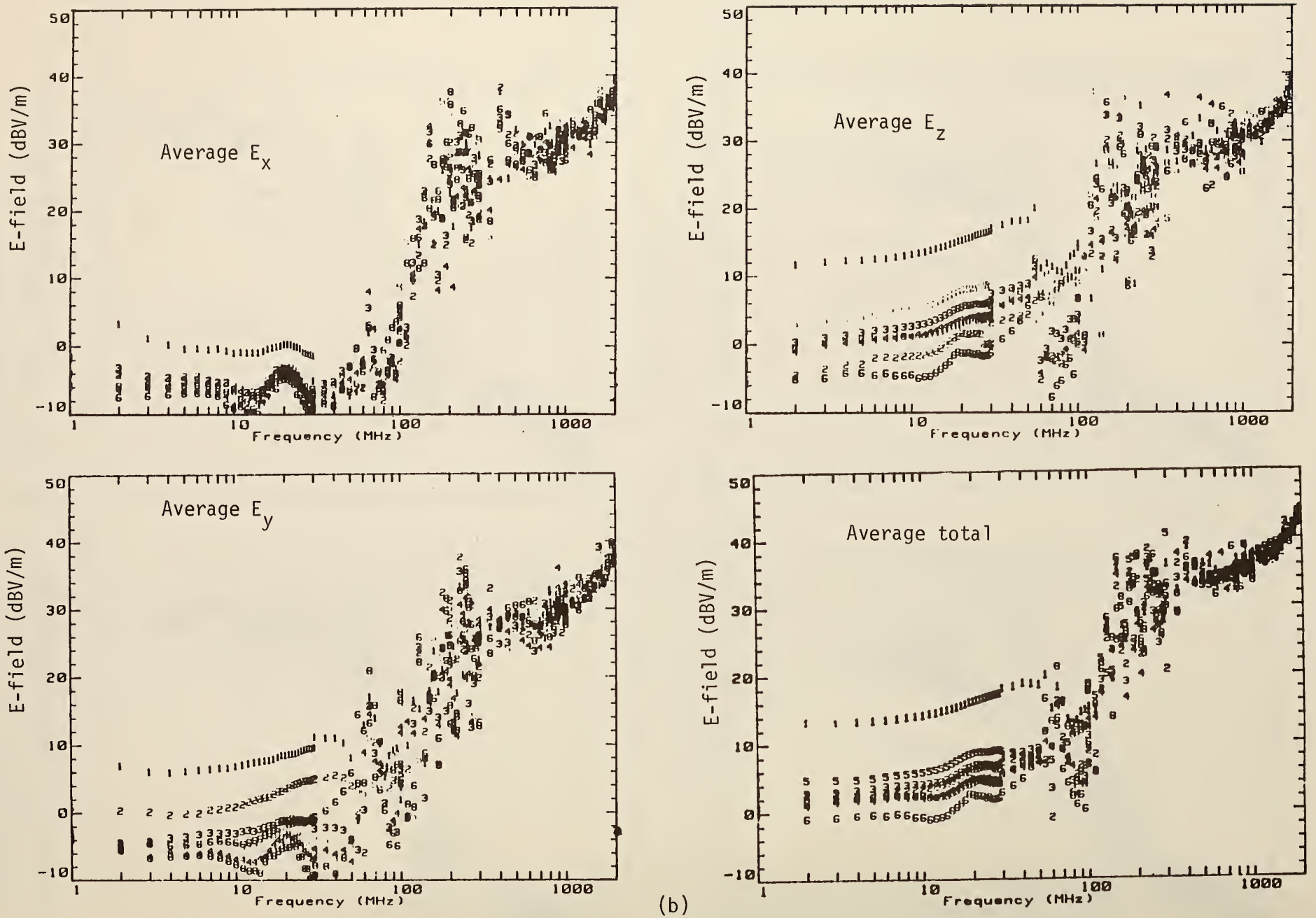

Figure 4.17 Spatial distribution of E-field components in the 1/10 scaled chamber measured with 7 NIST isotropic probes (5 cm dipoles) when transmitting 1 W net input power from back plate: (a) maximum and (b) average values.

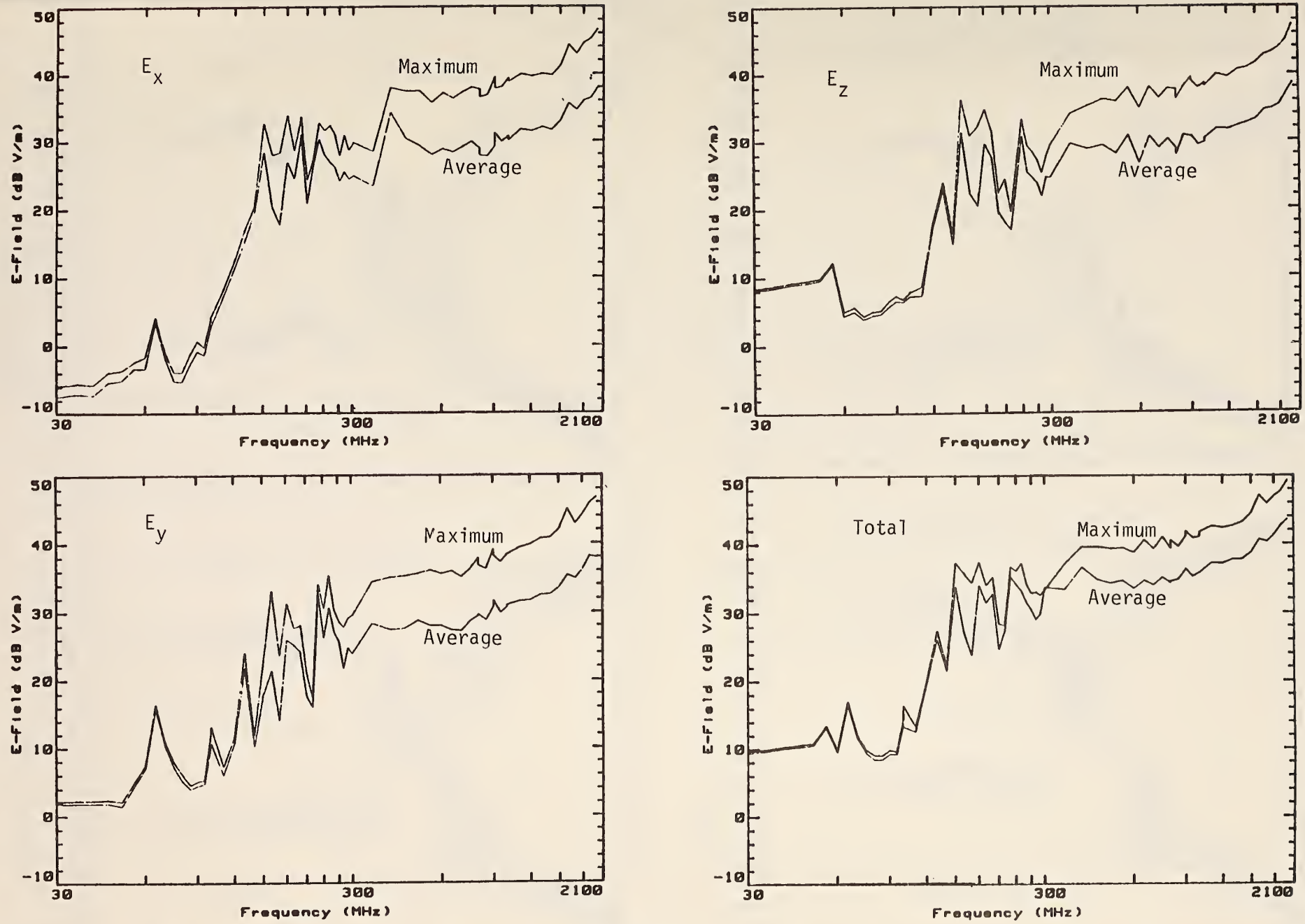

Figure 4.18 Smoothed average and maximum of measured E-field components in the 1/10 scaled chamber generated by the back plate with 1 W net input power, determined from data in figure 4.17.

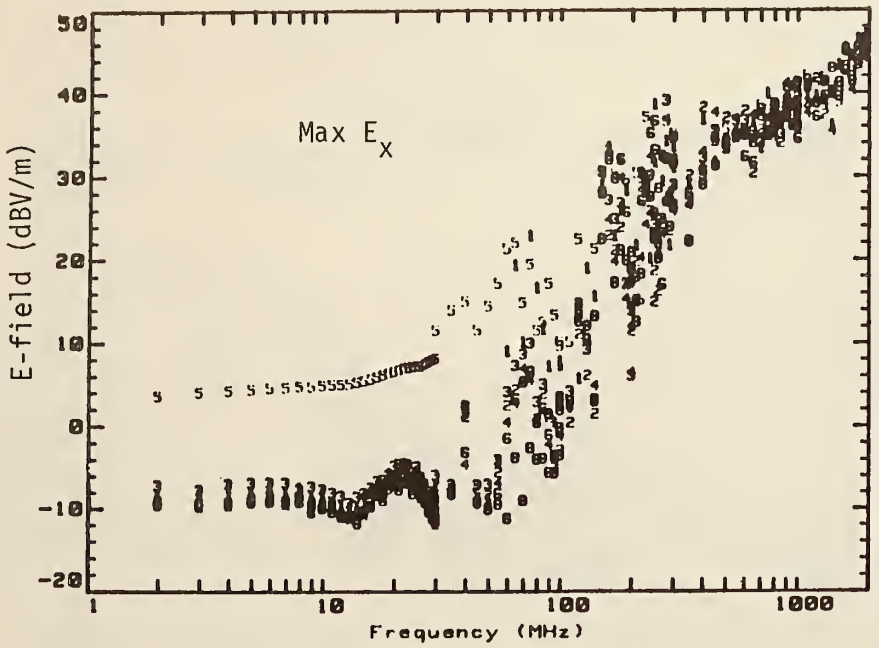

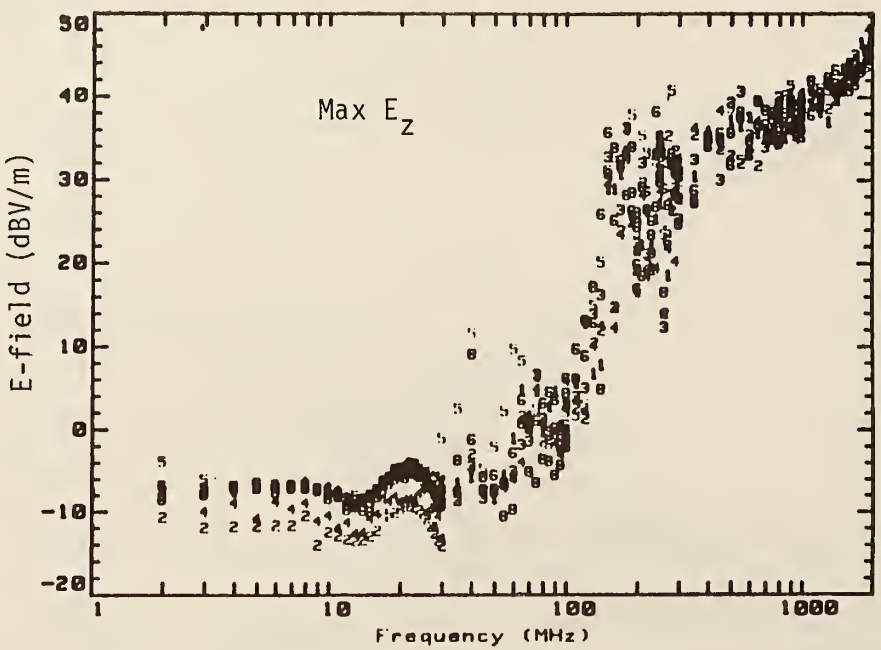

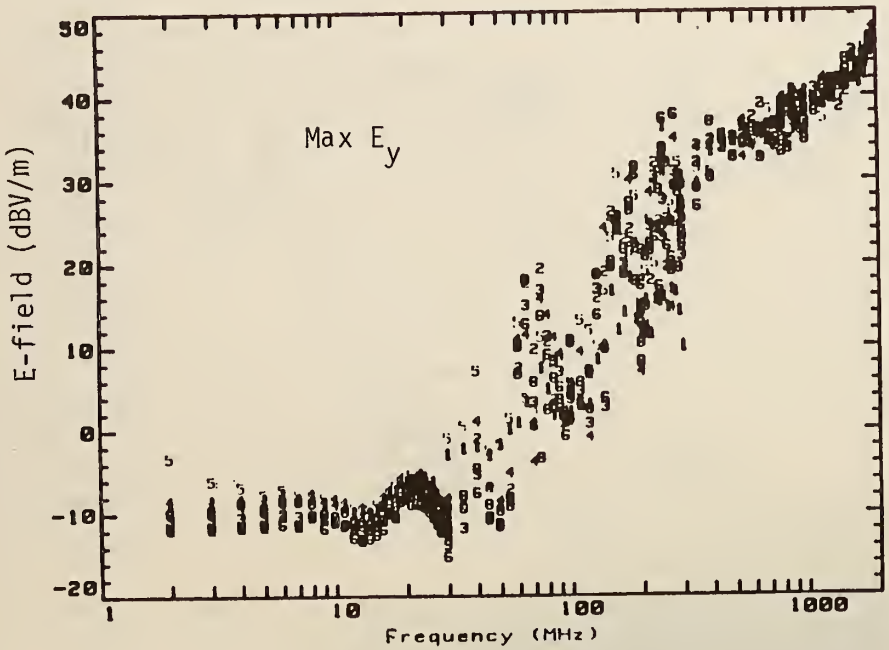

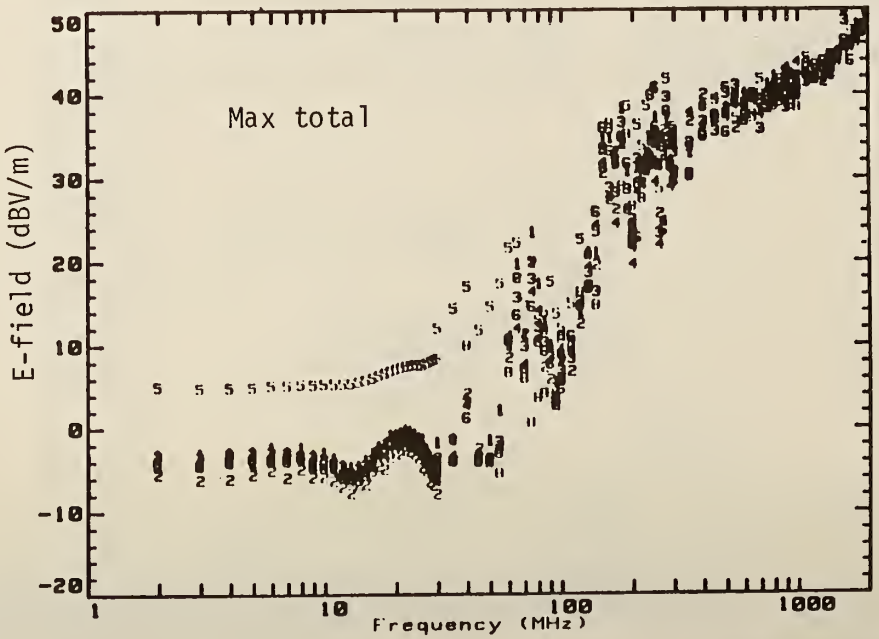

(a)

Figure 4.19 (a)

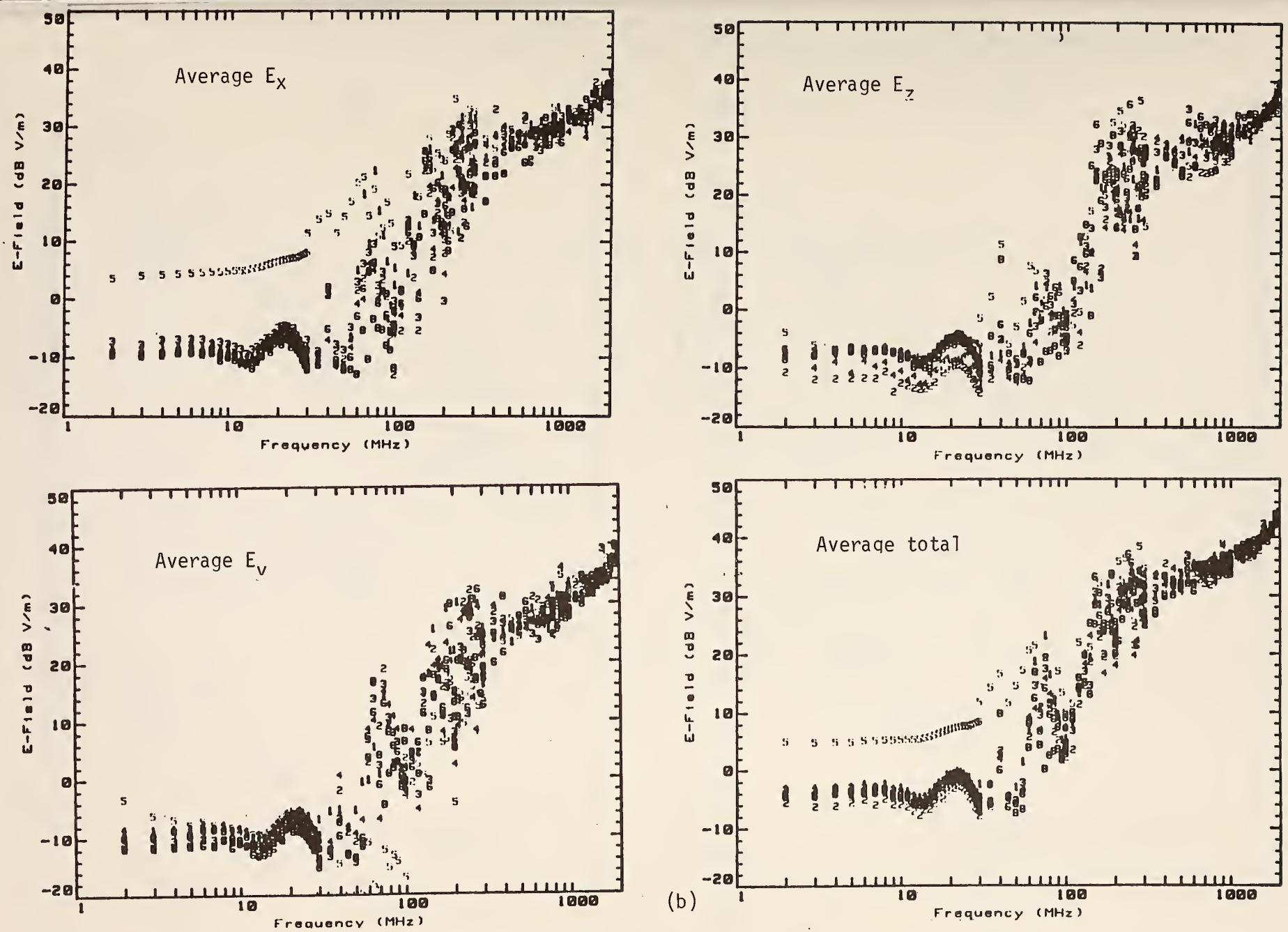

Figure 4.19 Spatial distribution of E-field components in the 1/10 scaled chamber measured with 7 NIST isotropic probes (5 cm dipoles) when transmitting 1 W net input power from side plate: (a) maximum and (b) average values.

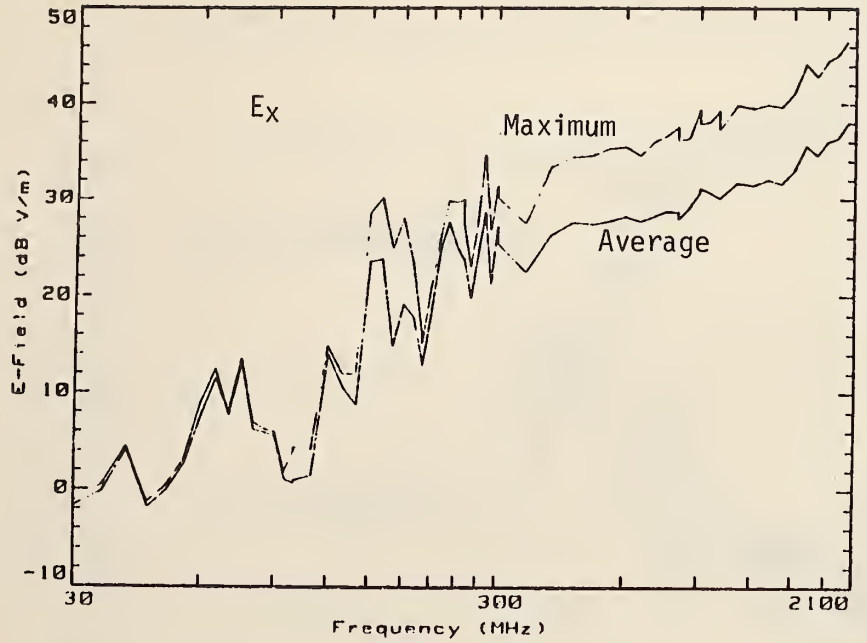

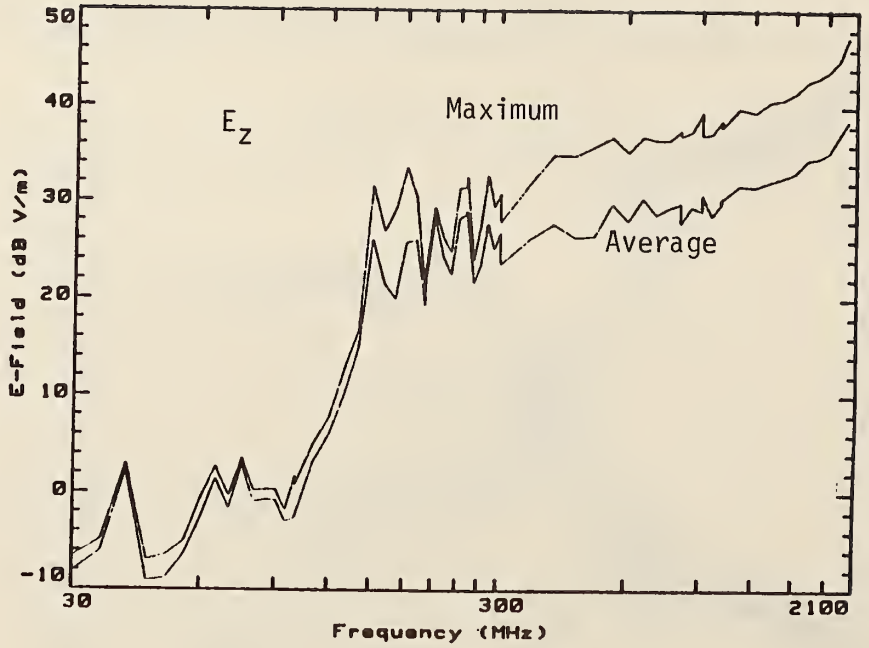

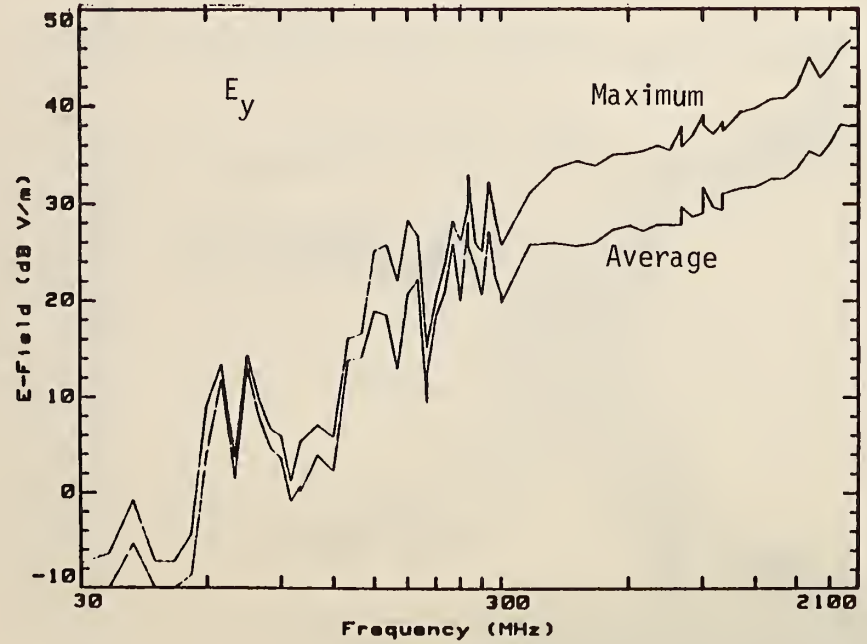

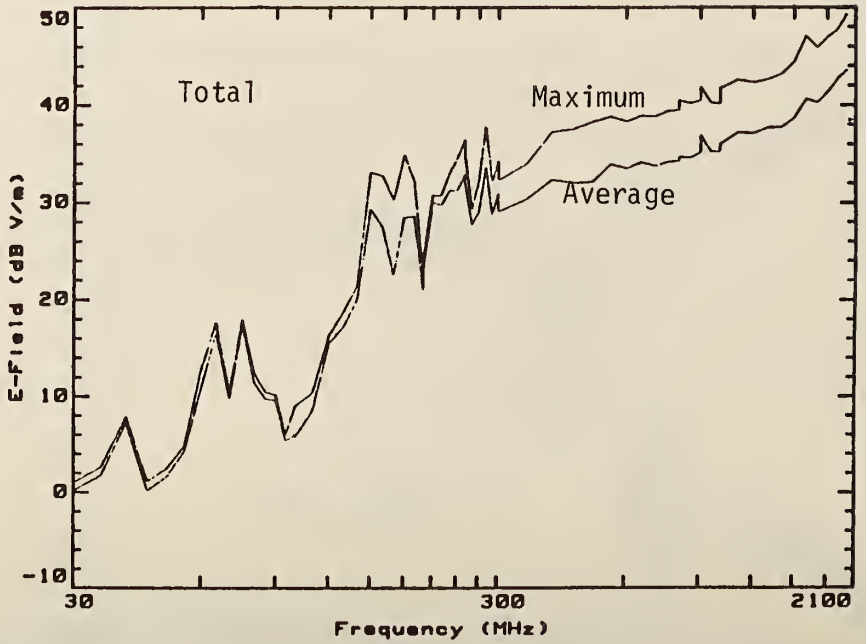

Figure 4.20 Smoothed average and maximum of measured E-field components in the 1/10 scaled chamber generated by the side plate with 1 W net input power, determined from data in figure 4.19.

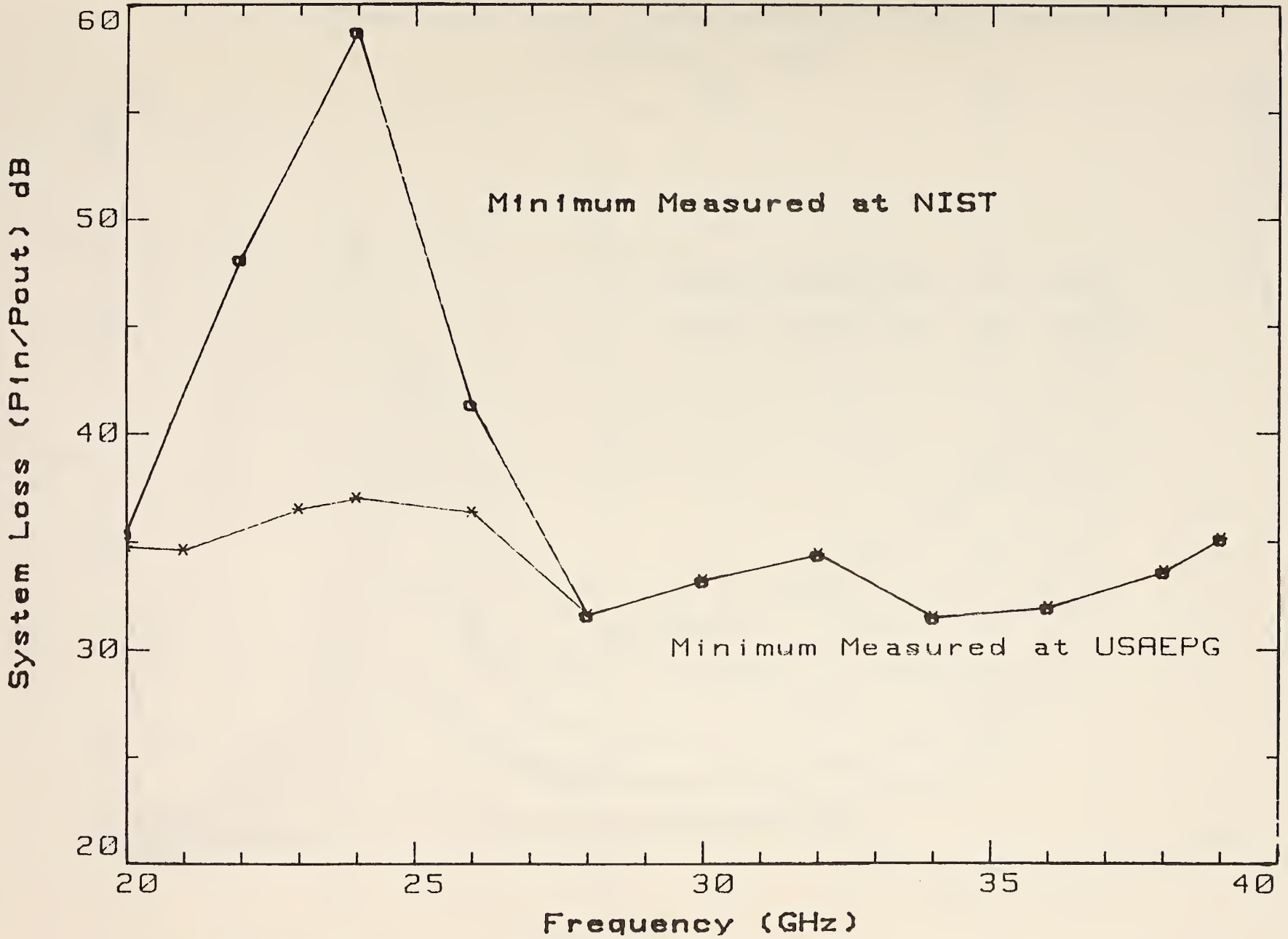

Figure 4.21 Measured coupling efficiency (minimum loss) of the horn antennas (transmitting/receiving) placed inside the 1/10 scaled chamber at 20 to 40 GHz.

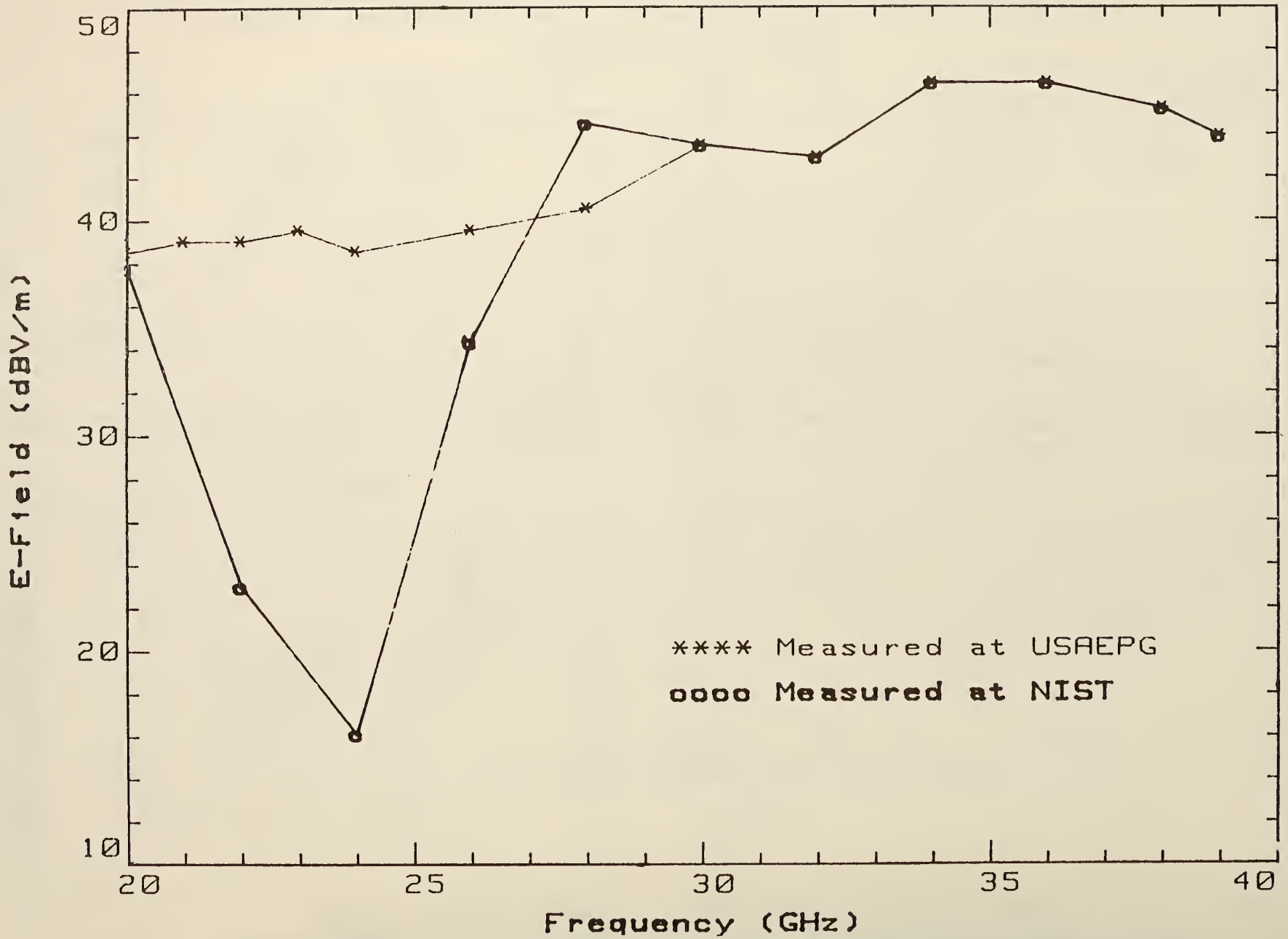

Figure 4.22 Maximum E-fields in the 1/10 scaled chamber determined from power measurements of the receiving antenna, 20 to 40 GHz, with a net input power of 1 W.

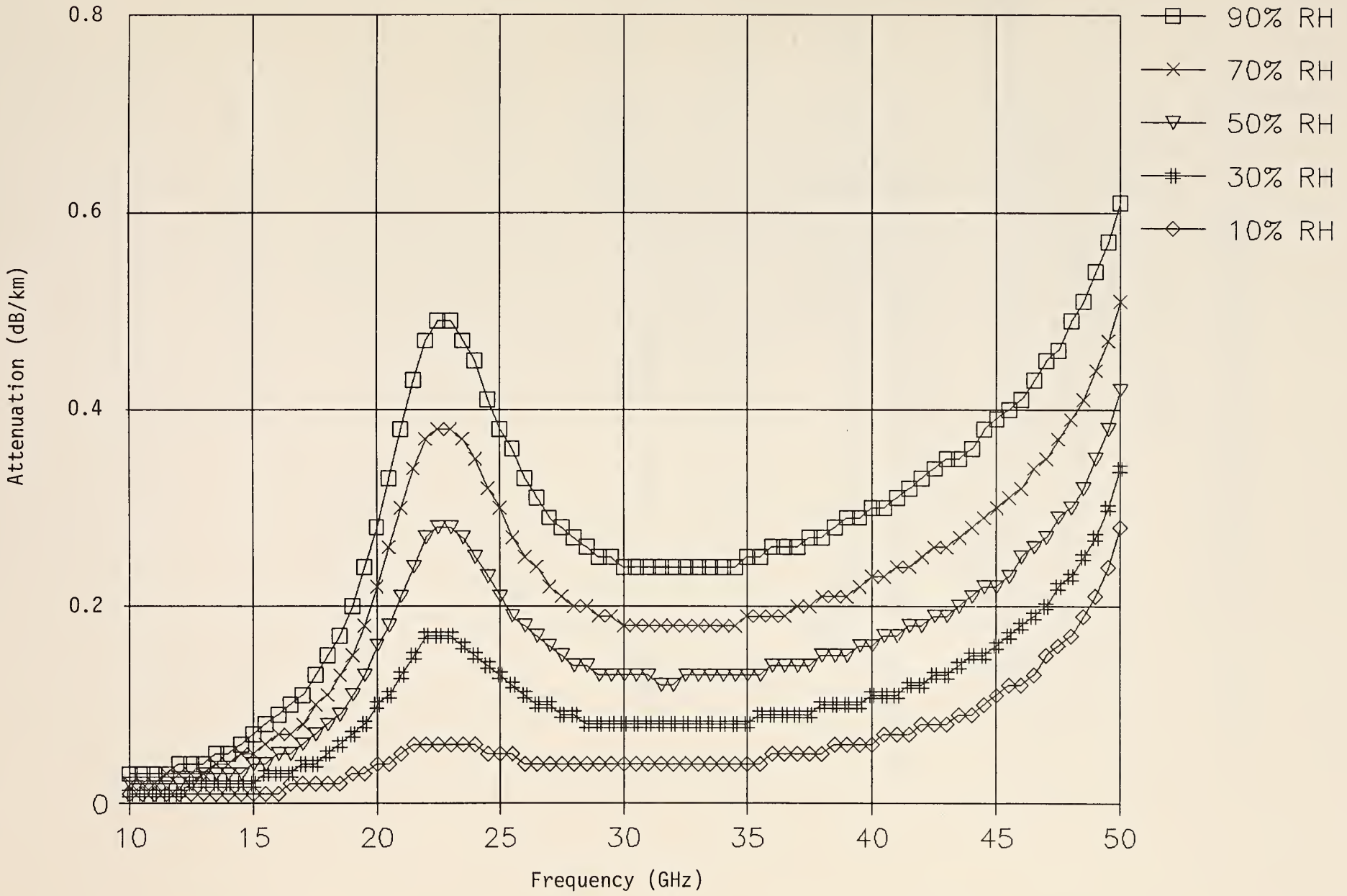

Figure 4.23 Calculated normalized propagation attenuation in air for 5 humidities.

Table 4.1 Spatial variations in E fields measured inside the 1/10 scaled TEM/reverberating chamber over the test volume defined by probes shown in figure 4.14.

Frequency, MHz	E-Fields Variation, dB
0.01 - 200	± 10
300	± 8
500	± 6
700	± 4
1000	± 3
2000	± 2

Table 4.2 Summary of operation characteristics of the 1/10 scaled TEM/reverberating chamber.

1. TEM Region (10 kHz to 70 MHz)

   Planar Field Simulation

   1 kW Input Power Yields Approximately
   250 V/m vertical polarization and 80 V/m horizontal polarization

   Uncertainty < ± 2 to 9 dB

2. Transition Region (70 MHz to 300 MHz)

   TEM Field Plus Limited Higher-Order Modes

   1 kW Input Power Yields Approximately 250 to 1000 V/m

   Polarization Variable

   Uncertainty = ± 10 dB

3. Reverberating Region (300 MHz to 40 GHz or Higher)

   Complex Field Simulation

   10 W Input Power Yields Approximately 100 to 300 V/m

   Uncertainty = ± 4 to 8 dB

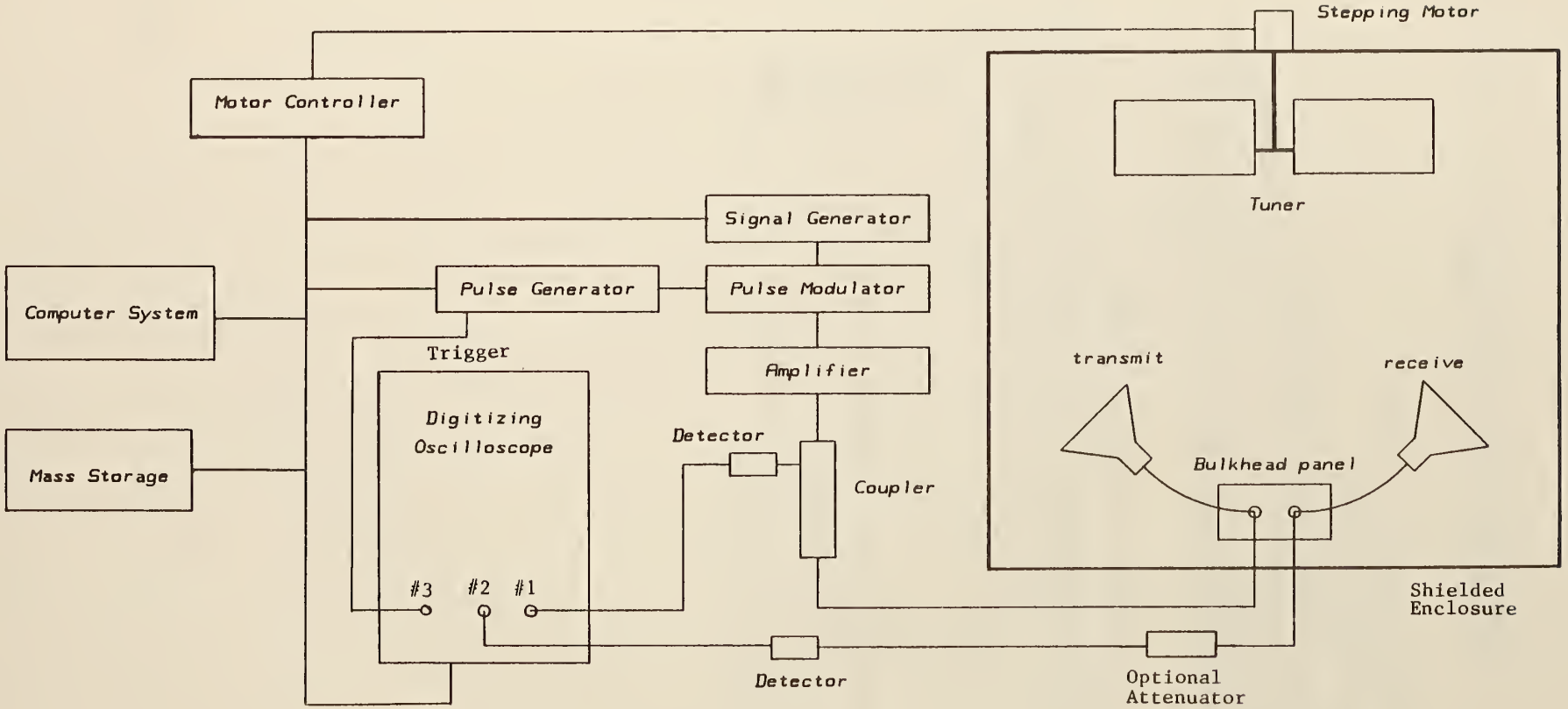

Figure 5.1 Block diagram of instrumentation used in pulsed rf evaluation of the 1/10 scaled TEM/reverberating chamber.

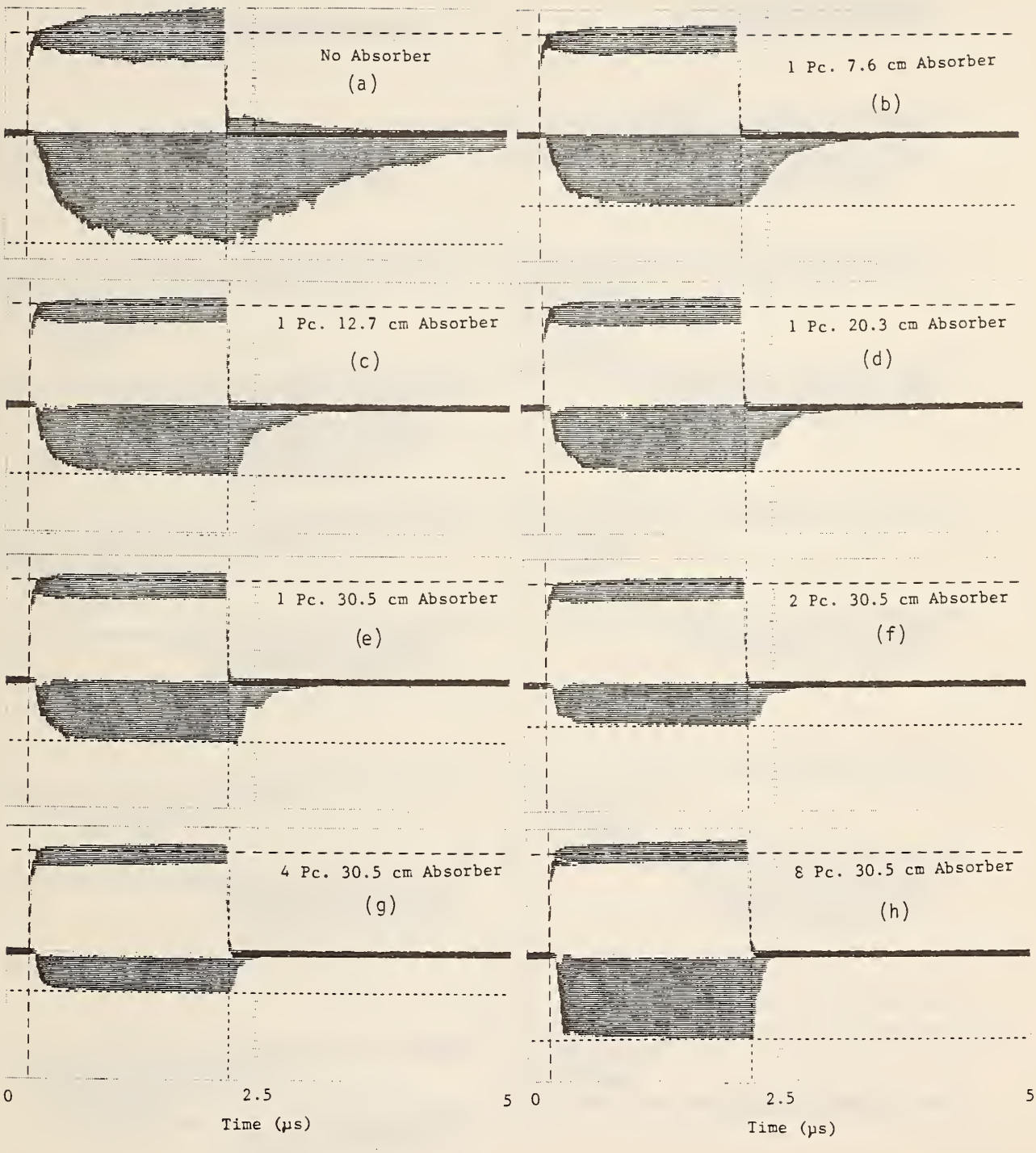

Figure 5.2 Maximum values of transmitted (positive) and received (negative) rf pulse waveforms in the 1/10 scaled TEM/reverberating chamber determined with increasing amounts of rf absorber loading at 0.9 GHz.

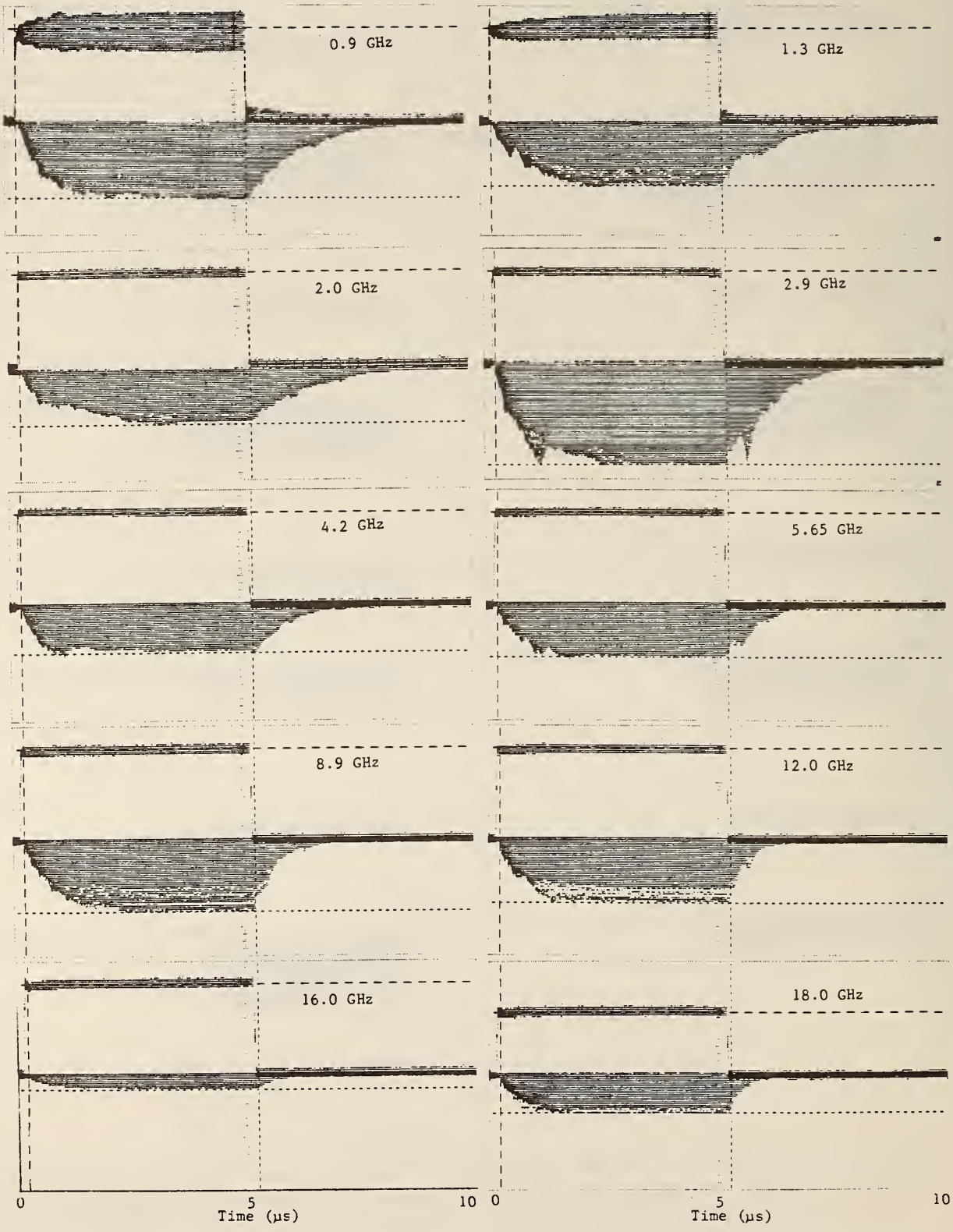

Figure 5.3 Maximum values of transmitted and received rf pulse waveforms inside empty (no absorber) 1/10 scaled TEM/reverberating chamber determined at selected frequencies. Rf input pulse width is 5 μs, duty cycle is 0.001.

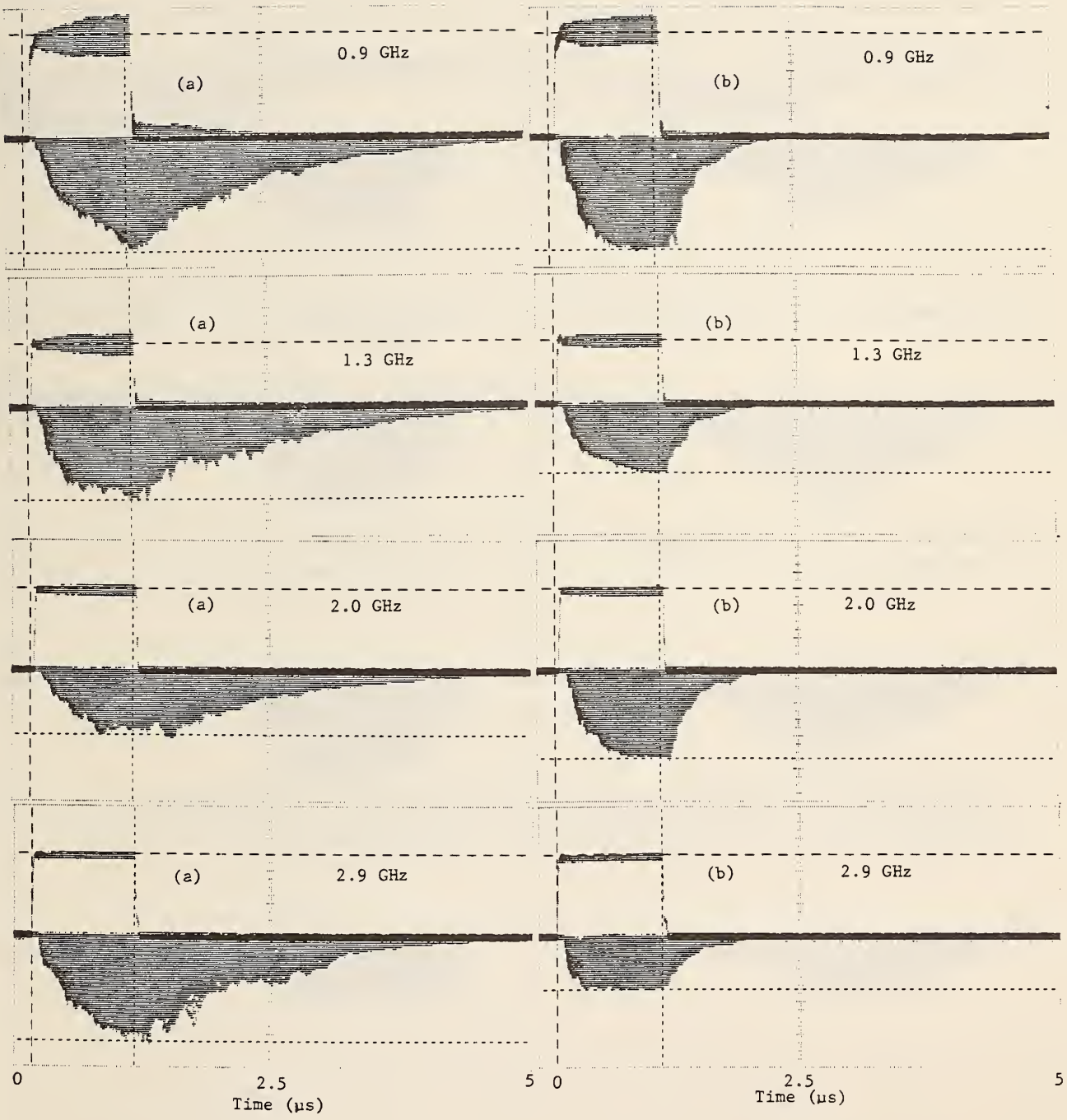

Figure 5.4 Sheet 1 of 3.

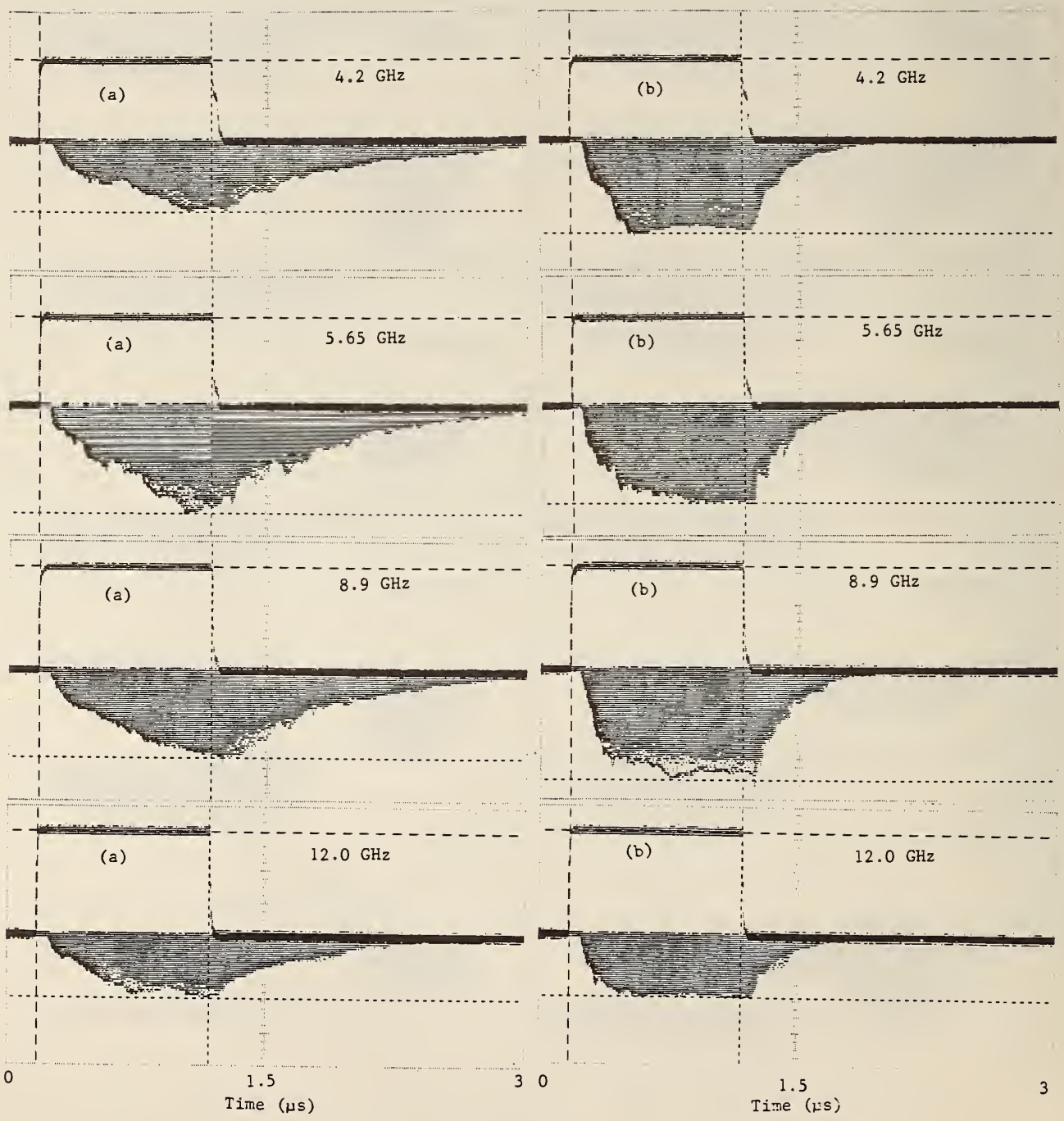

Figure 5.4 Sheet 2 of 3.

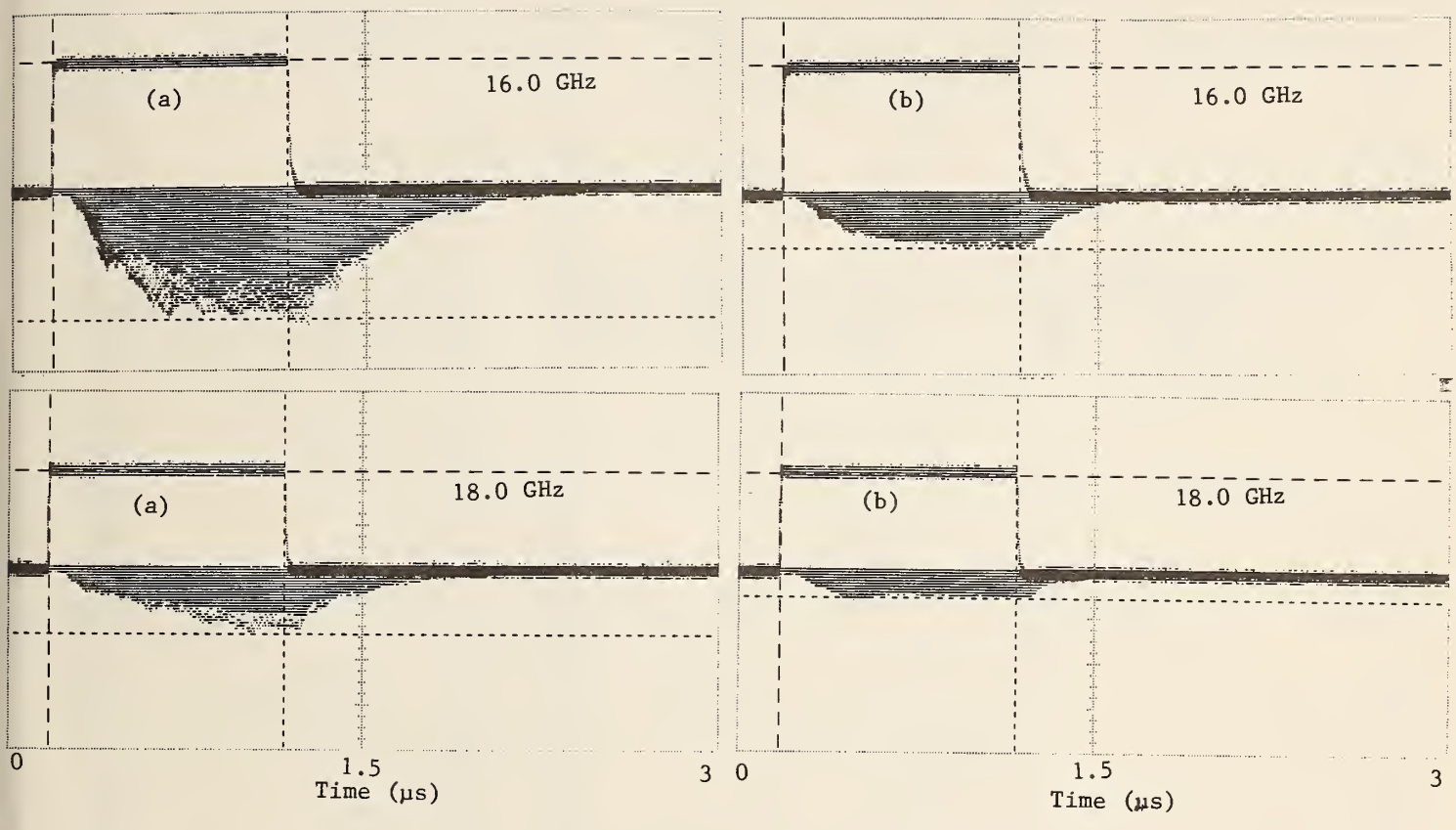

Figure 5.4 Sheet 3 of 3

Figure 5.4 Maximum values of transmitted and received rf pulse waveforms inside 1/10 scaled TEM/reverberating chamber determined with: (a) no absorber, and (b) 1 piece of 20.3 cm X 61 cm X 61 cm (8" X 24" X 24") rf absorber at selected frequencies.

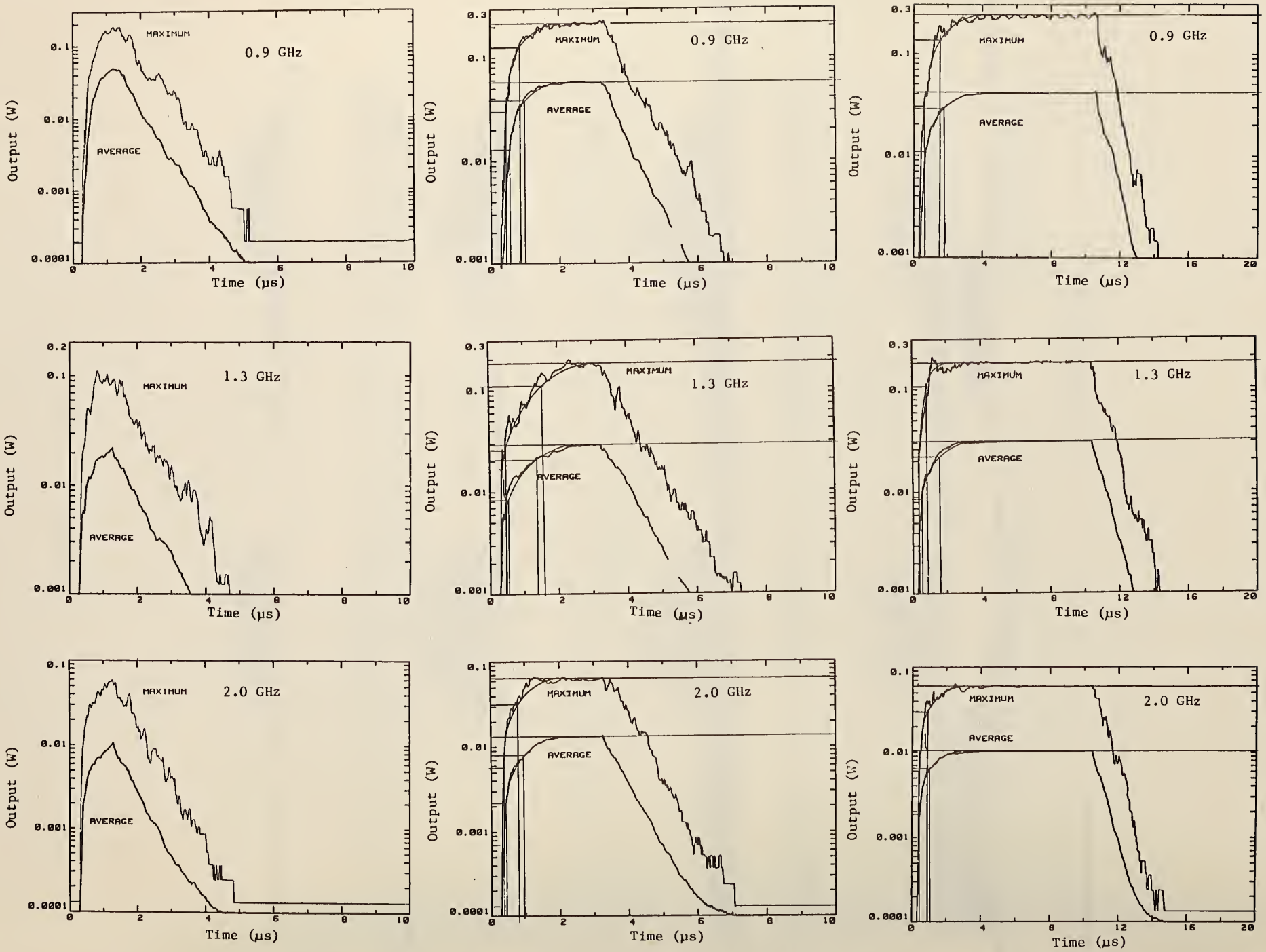

Figure 5.5 Sheet 1 of 4.

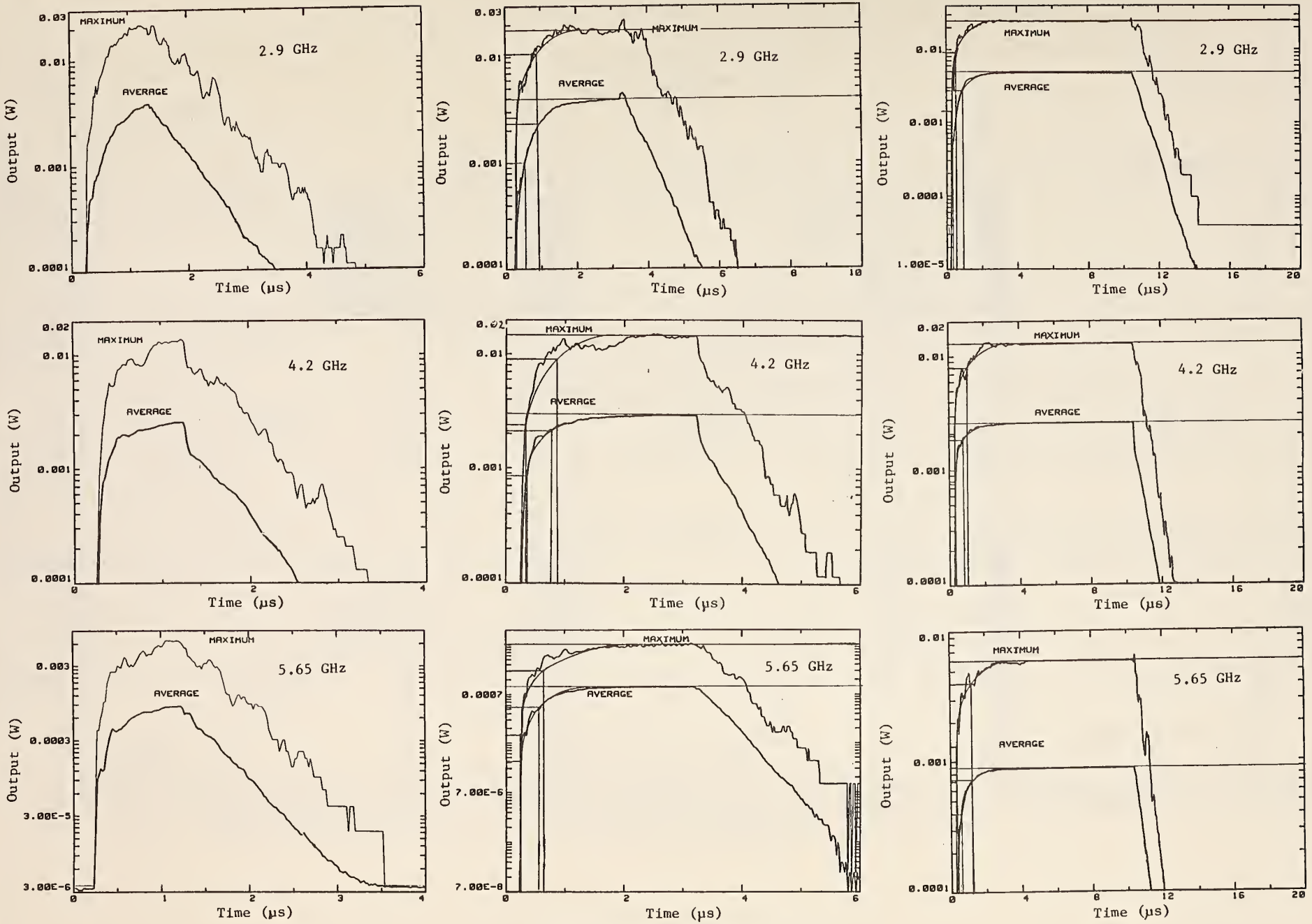

Figure 5.5 Sheet 2 of 4.

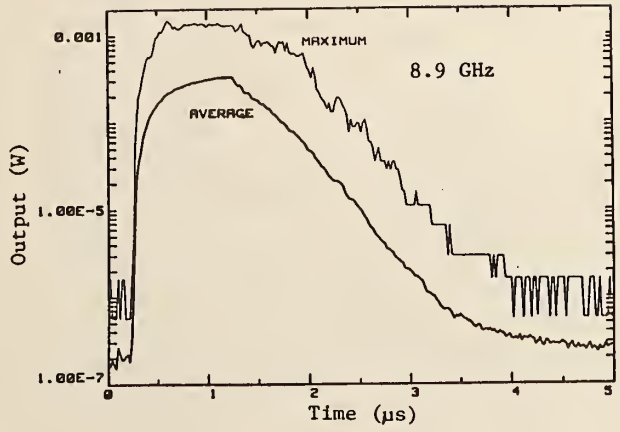

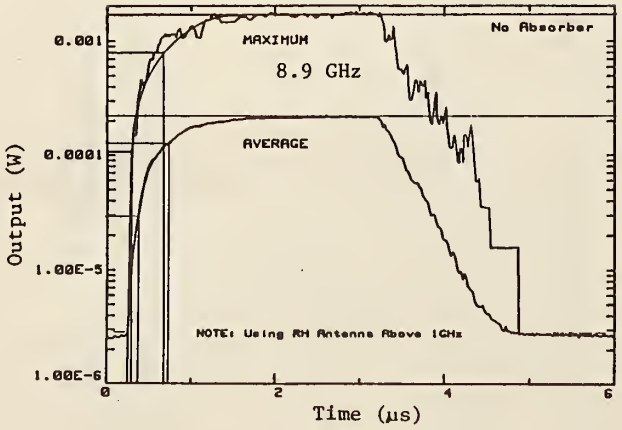

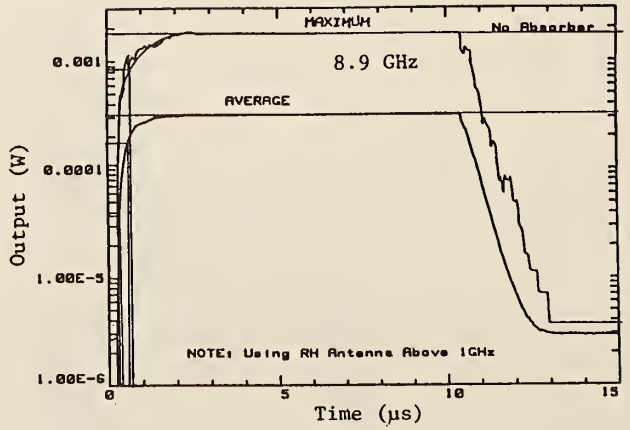

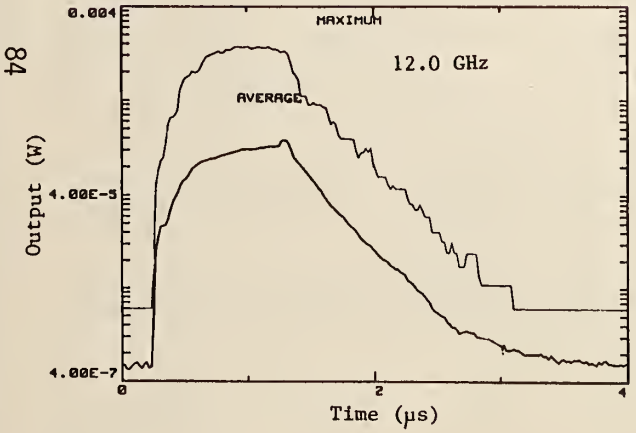

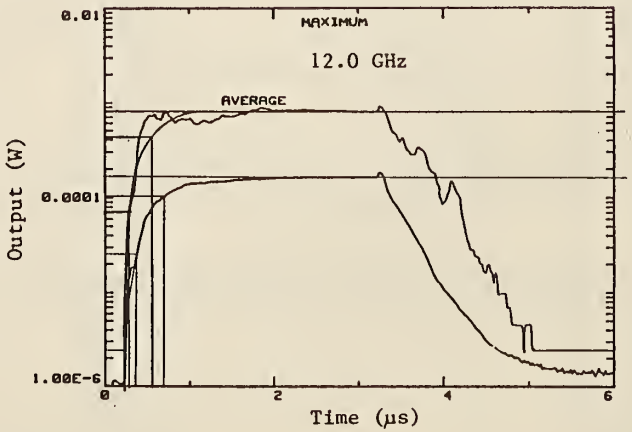

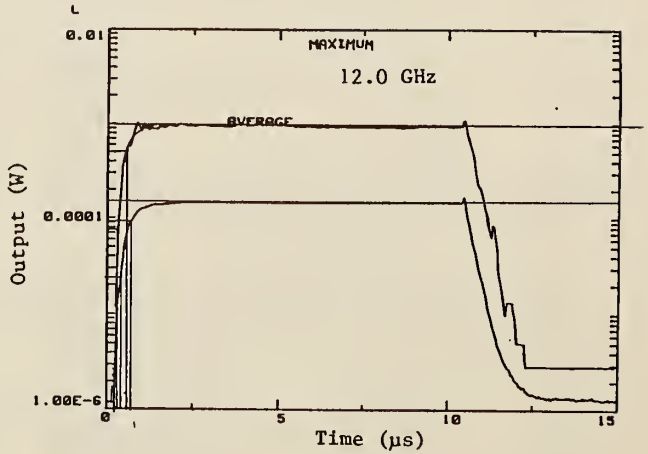

Figure 5.5 Sheet 3 of 4.

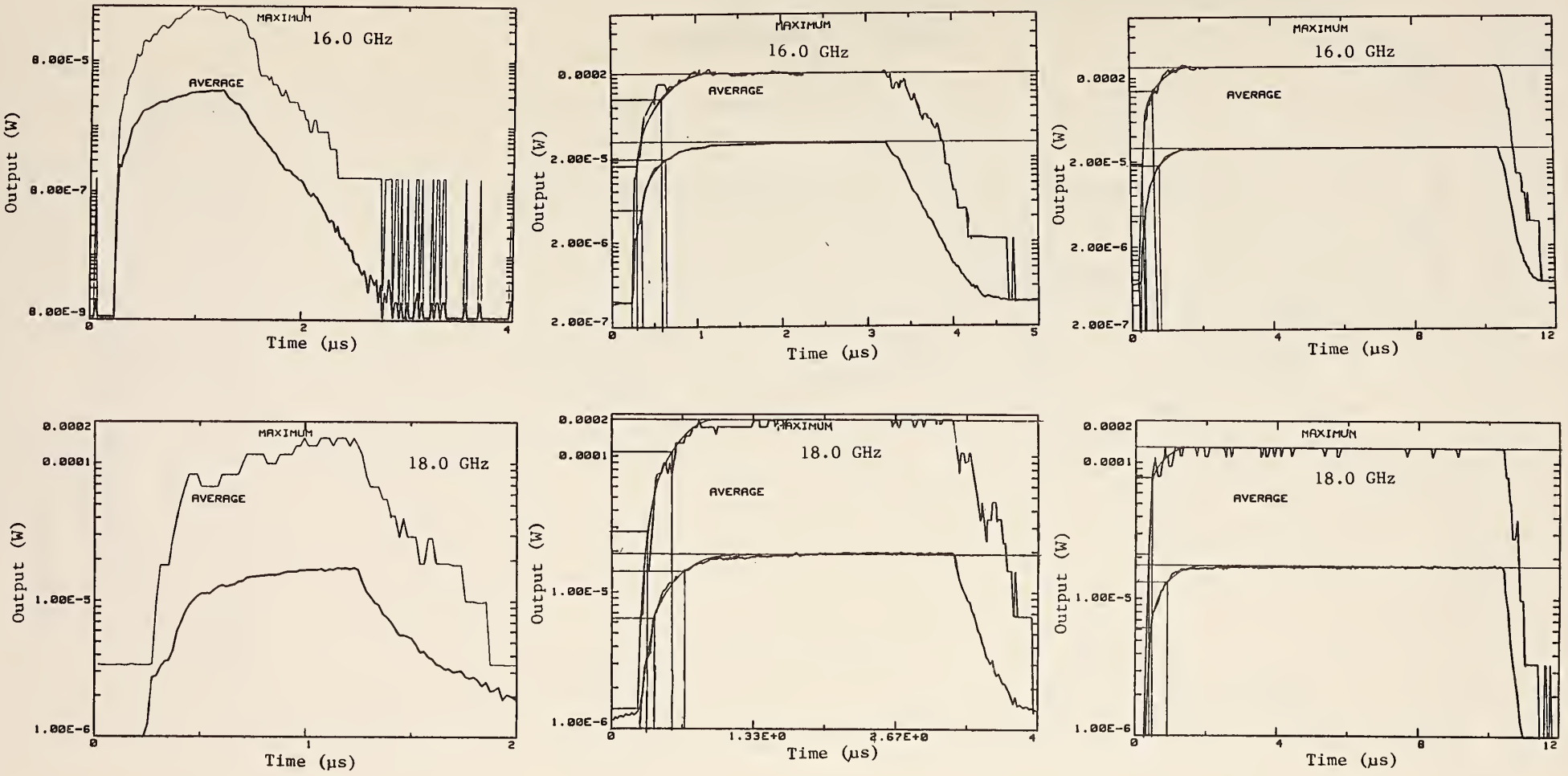

Figure 5.5 Sheet 4 of 4.

Figure 5.5 Maximum and average values of received rf pulse waveforms inside the 1/10 scaled TEM/ reverberating chamber determined by mode-tuned approach. Chamber empty (no absorber). Measurements were taken at 10 selected frequencies and 3 pulse widths.

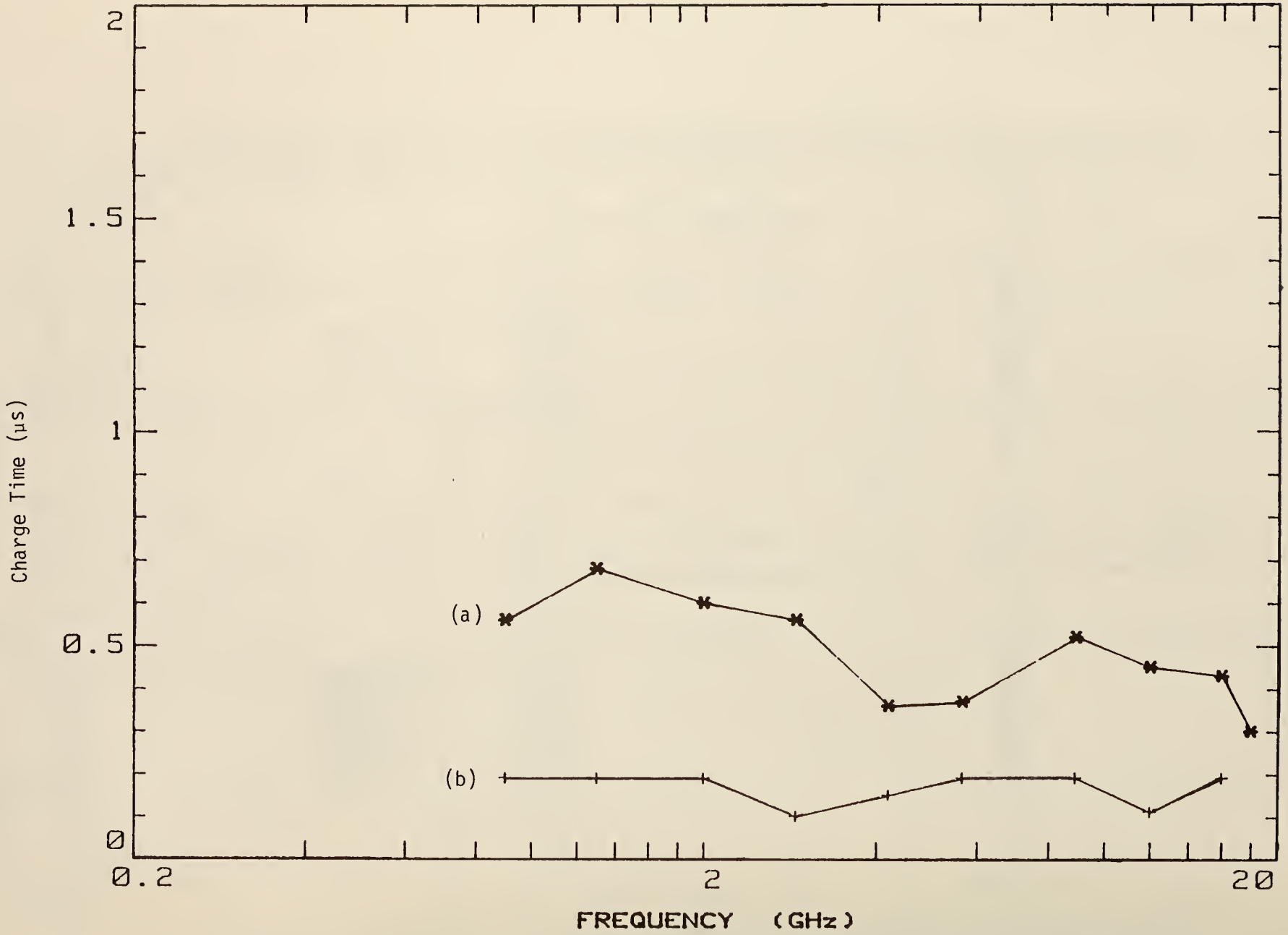

Figure 5.6 Time required for rf signal transmitted into the 1/10 scaled TEM/reverberating chamber to rise 63% of steady-state amplitude using: (a) no absorber, and (b) 1 piece of 20.3 cm X 61 cm X 61 cm rf absorber.

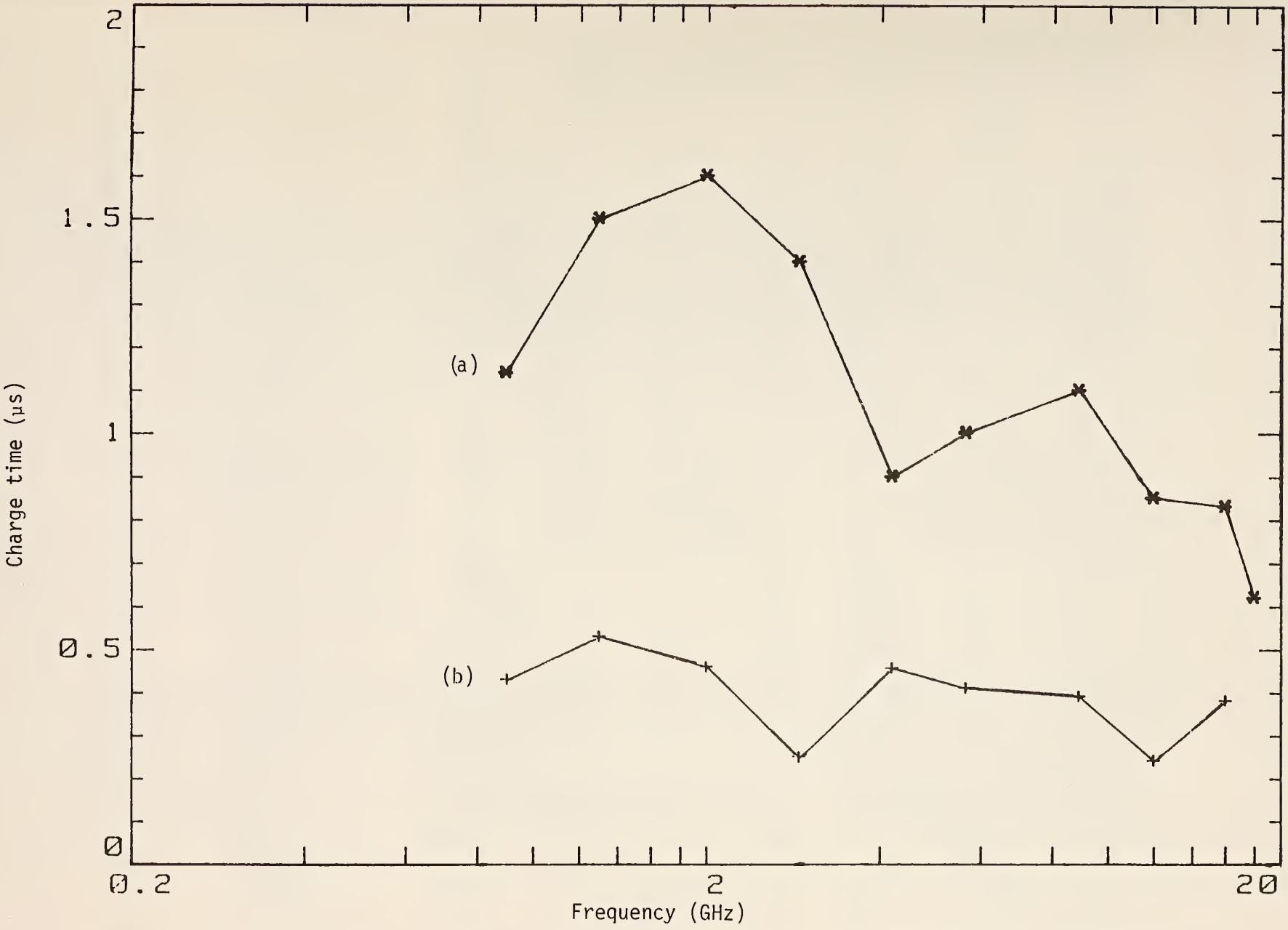

Figure 5.7 Time required for rf signal transmitted into the 1/10 scaled TEM/reverberating chamber to rise 90% of steady-state amplitude using: (a) no absorber, and (b) 1 piece of 20.3 cm X 61 cm X 61 cm rf absorber.

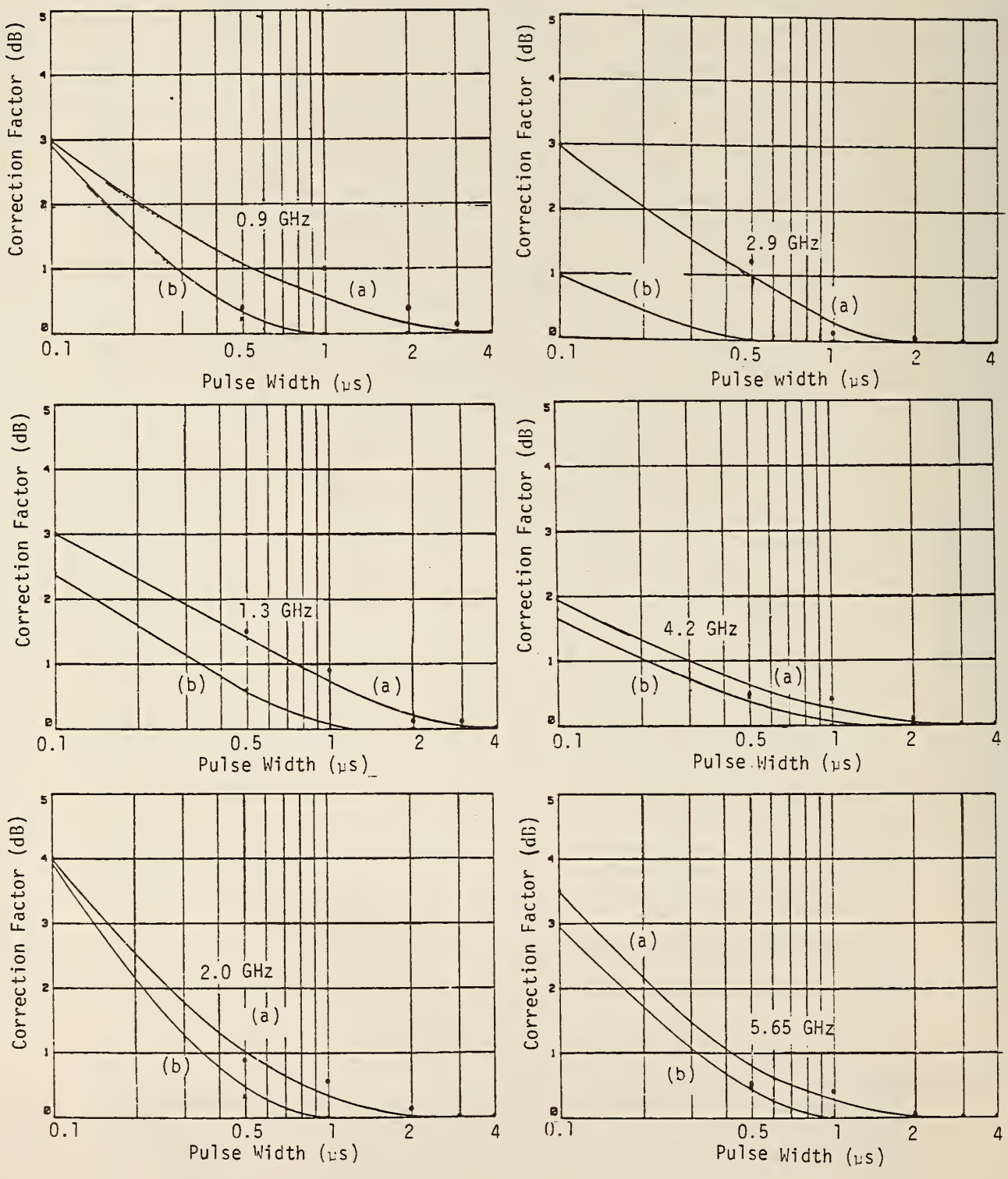

Figure 5.8 Sheet 1 of 2.

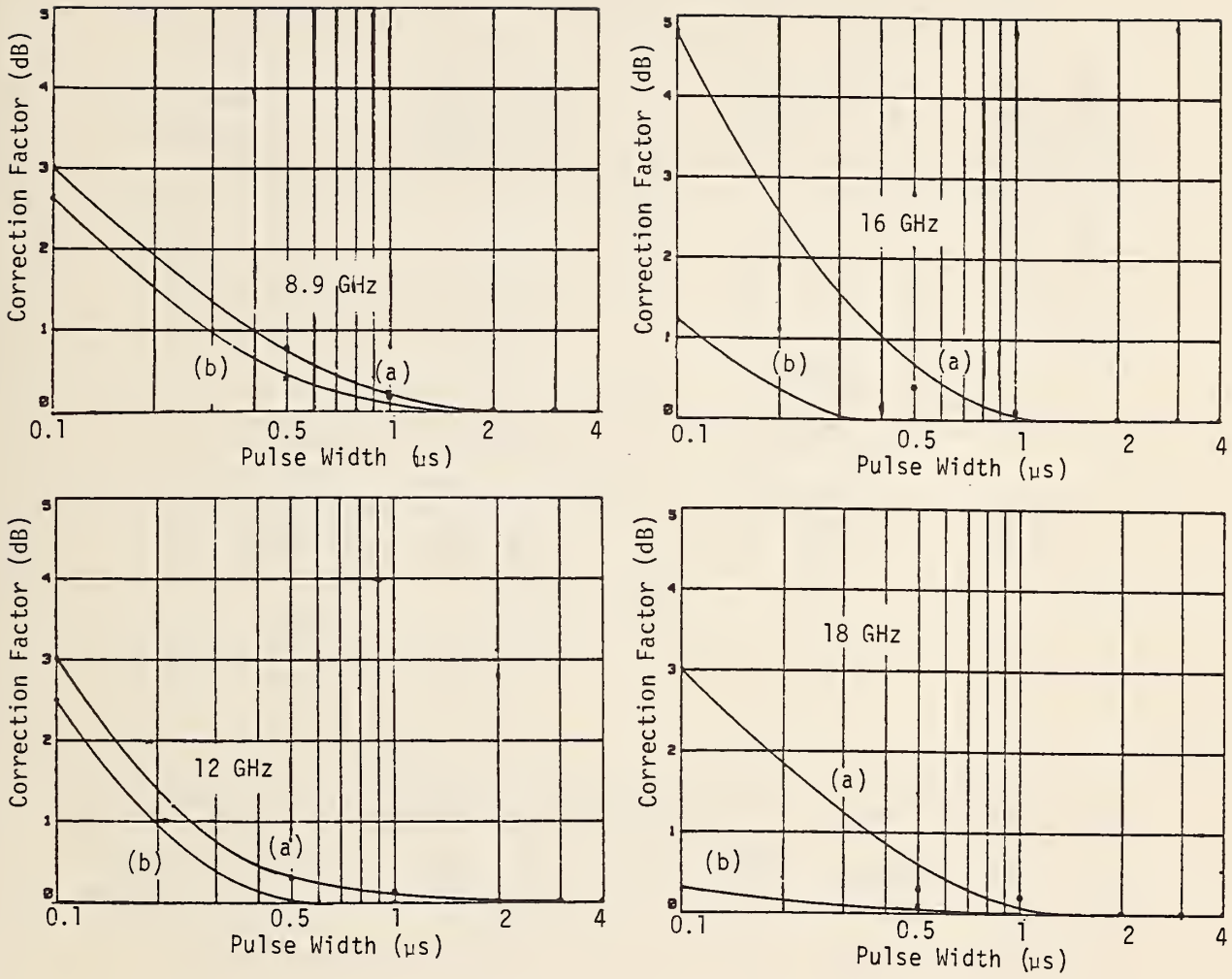

Figure 5.8 Sheet 2 of 2

Figure 5.8 Estimated correction factors for amplitude response of rf test pulses in the 1/10 scaled TEM/reverberating chamber at selected frequencies as a function of input pulse width using (a) no absorber, and (b) 1 piece of 20.3 cm x 61 cm x 61 cm rf absorber.

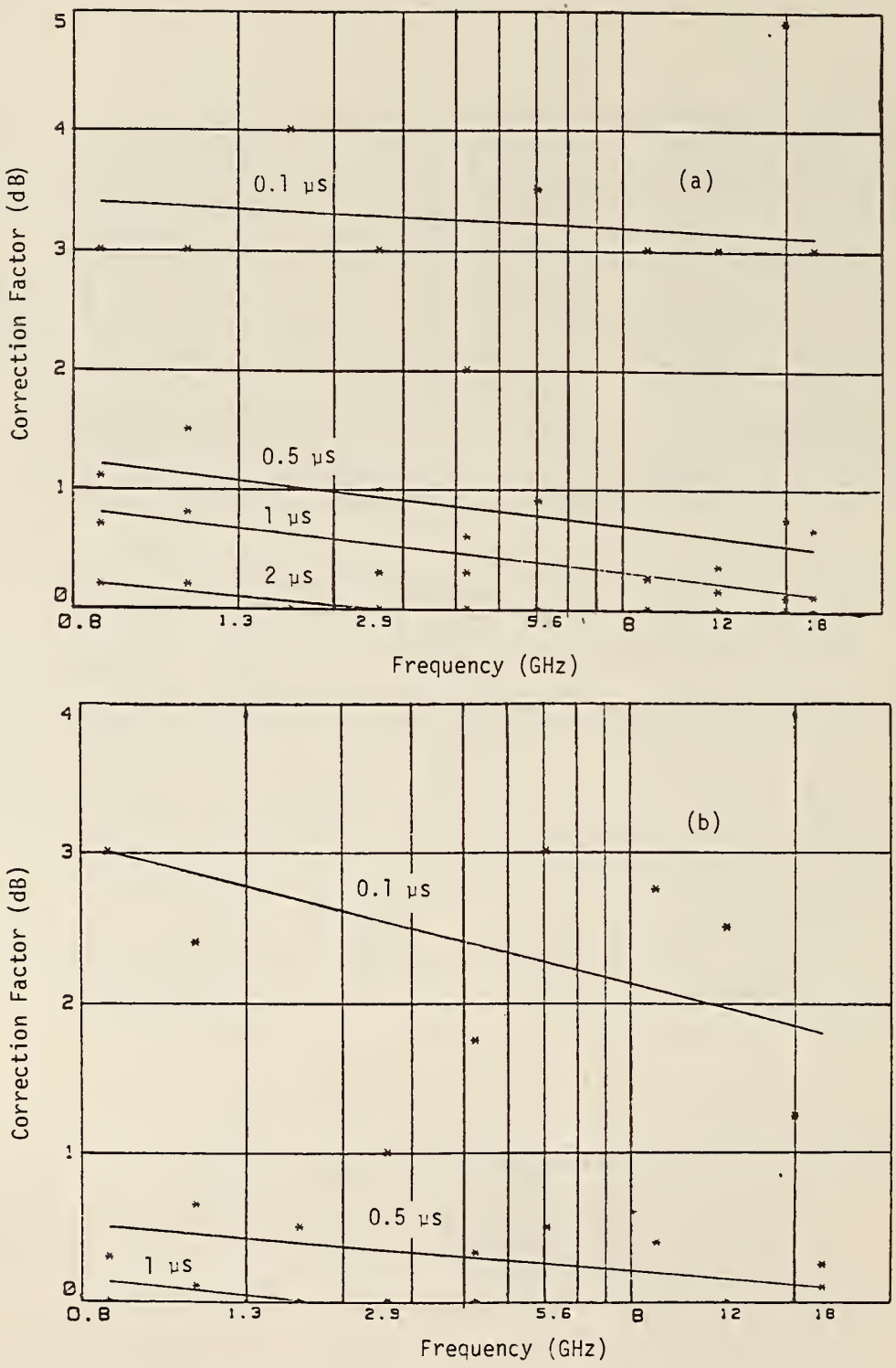

Figure 5.9 Estimated correction factors for amplitude response of rf test pulses in the 1/10 scaled TEM/reverberating chamber at selected input pulse widths as a function of frequency using (a) no absorber, and (b) 1 peice of 20.3 cm x 61 cm x 61 cm rf absorber.

Table 5.1 Summary of influences of rf absorber loading on loss, quality factor, and charge/decay time of the 1/10 scaled TEM/reverberating chamber at 0.9 GHz.

Absorber Loading	Min. Chamber Loss, dB	Max. Quality Factor	Measured* Charge/Decay Time, μs
None	7.0	10 418	0.29
1 pc. 7.6 cm	10.8	4 333	0.22
1 pc. 12.7 cm	11.1	4 043	0.19
1 pc. 20.3 cm	11.7	3 522	0.18
1 pc. 30.5 cm	12.2	3 139	0.14
2 pc. 30.5 cm	15.6	1 435	0.10
4 pc. 30.5 cm	15.9	1 339	0.10
8 pc. 30.5 cm	21.4	377	0.10

*Charge/decay time is measured from figure 5.2, based upon 63% rise to steady-state field amplitude inside chamber after excitation source is turned on, or 63% decay from steady-state amplitude after source is turned off.

Table 5.2 Comparison of measured and calculated charge/decay time of the 1/10 scaled TEM/reverberating chamber, determined from chamber average loss measurements (figure 4.5) and from data shown in figure 5.5.

Frequency GHz	Average Chamber Loss, dB	Average Quality Factor $X(10)^4$	Calculated Charge/Decay Time* μs	Measured Charge/Decay Time μs
0.9	18	0.083	0.29	0.56
1.3	22	0.099	0.24	0.68
2.0	26	0.144	0.23	0.60
2.9	30.5	0.155	0.17	0.56
4.2	35	0.167	0.13	0.36
5.65	37.5	0.229	0.13	0.37
8.9	42	0.318	0.11	0.52
12.0	45	0.391	0.10	0.45
16.0	47	0.584	0.12	0.43
18.0	48	0.661	0.12	0.30

*Calculated charge/decay time is from $2Q/\omega$.

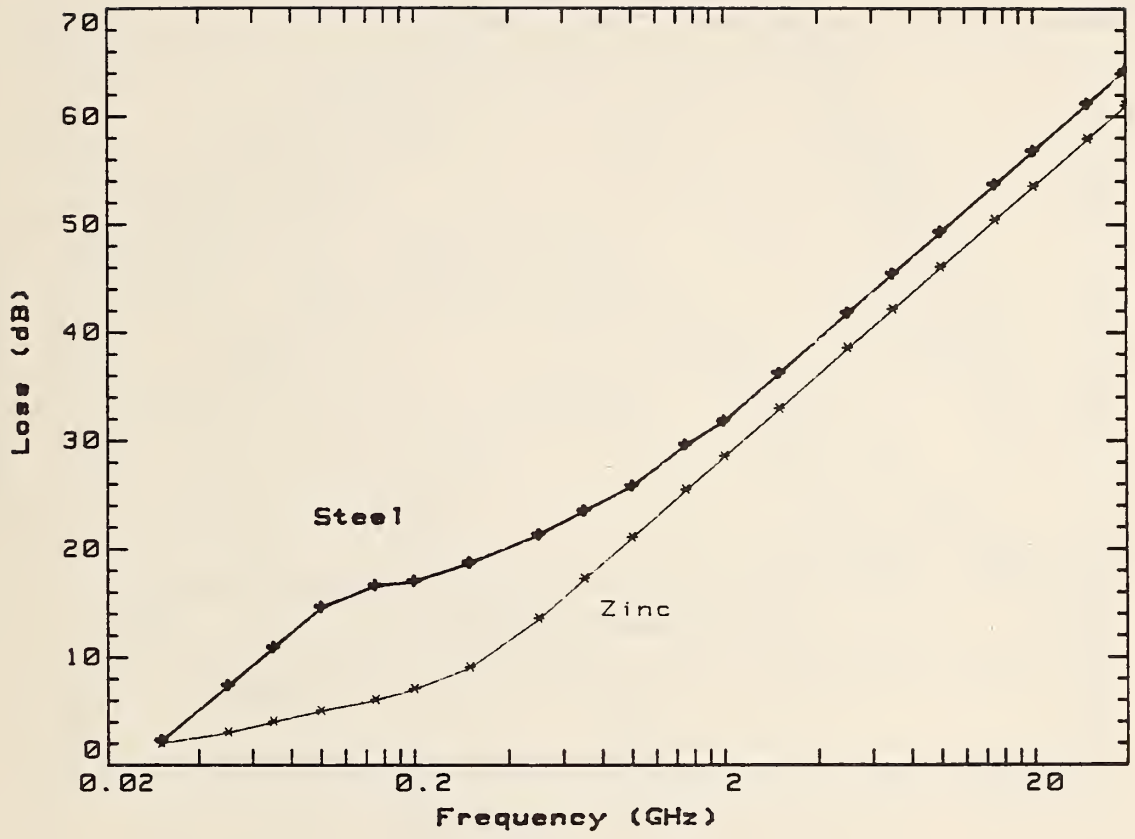

Figure 6.1 Projected coupling efficiency (minimum loss) of 13.1 m x 24.1 m x 38.7 m TEM/reverberating chamber.

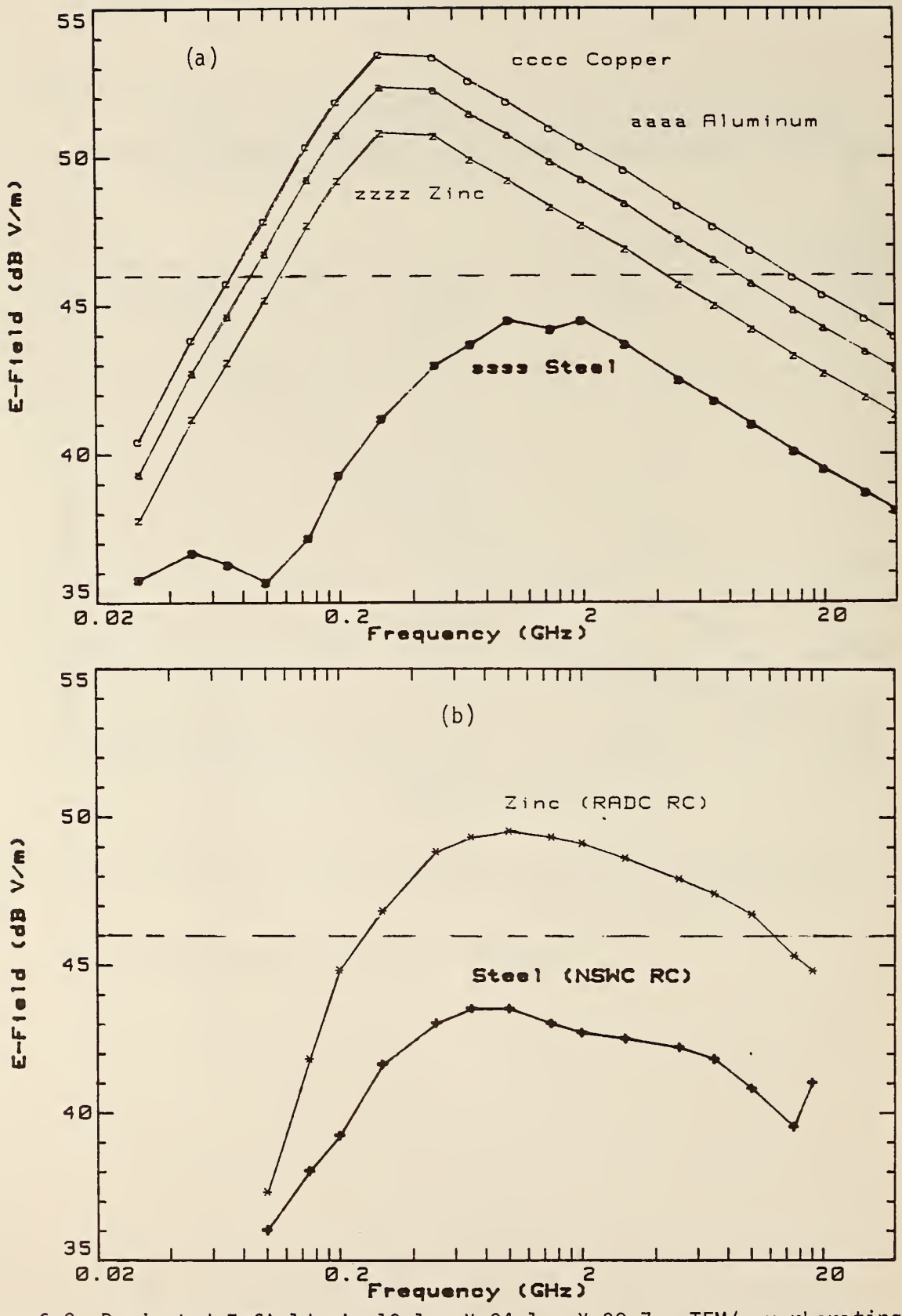

Figure 6.2 Projected E-fields in 13.1 m X 24.1 m X 38.7 m TEM/reverberating chamber for 200 W input power determined from (a) projected chamber losses and Q factors, and (b) measurements made in RADC chamber and NSWC chamber.

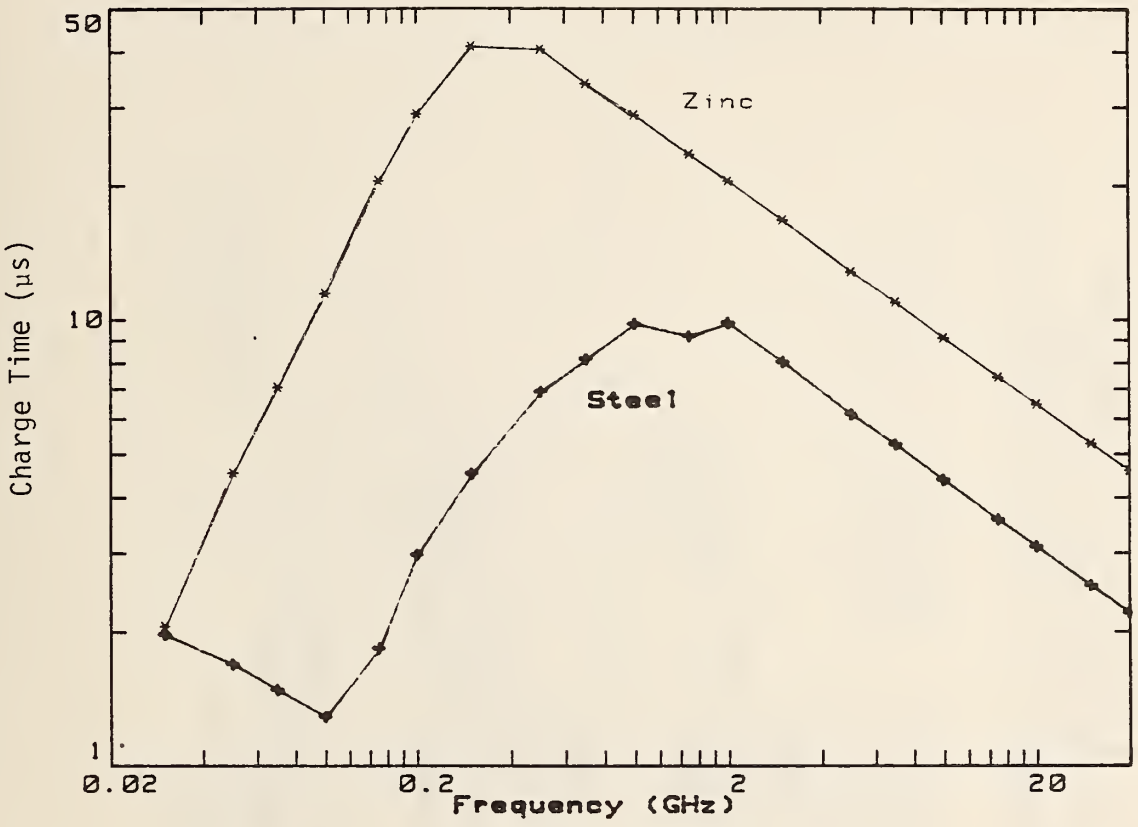

Figure 6.3 Projected charge time for 13.1 m X 24.1 m X 38.7 m TEM/ reverberating chamber.

TABLE 6.1 SUMMARY/CONCLUSIONS - 3 REGIONS OF OPERATION
13.1 m X 24.1 m X 38.7 m TEM/REVERBERATING CHAMBER
(ZINC COATED)

1. TEM (10 kHz - 7 MHz)
   PLANAR FIELD SIMULATION
   10 kW INPUT YIELDS APPROX.
   100 V/m VERT POL. & 50 V/m HOR POL.
   UNCERTAINTY < ± 2 - 10 dB

2. TRANSITION (7 MHz - 30 MHz)
   TEM FIELD PLUS LIMITED MODES
   10 kW INPUT YIELDS APPROX. 50 - 250 V/m
   POLARIZATION & UNCERTAINTY = ± 10 dB

3. REVERBERATING (30 MHz - 40 GHz?)
   COMPLEX NEAR FIELD SIMULATION
   200 W YEILDS APPROX. 200 V/m
   UNCERTAINTY < ± 4 - 8 dB

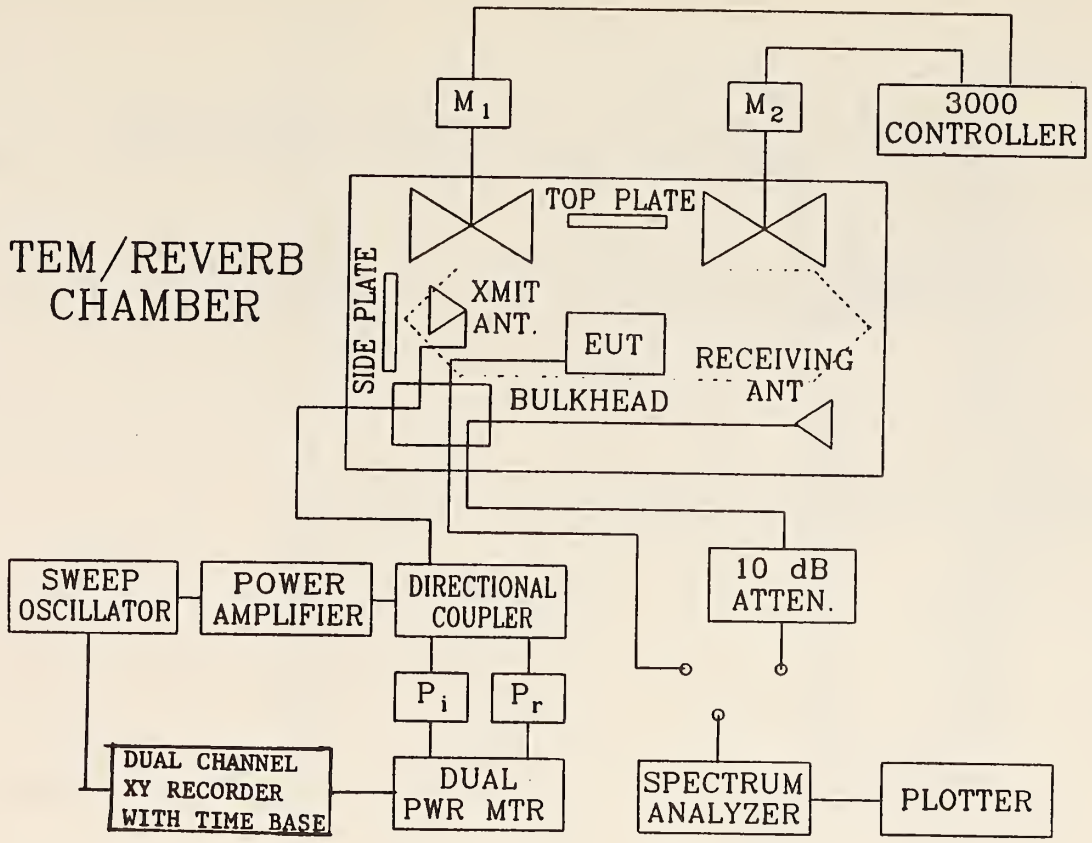

Figure 7.1 Block diagram of swept frequency EM radiated immunity and shielding effectiveness measurement system using TEM/reverberating chamber.

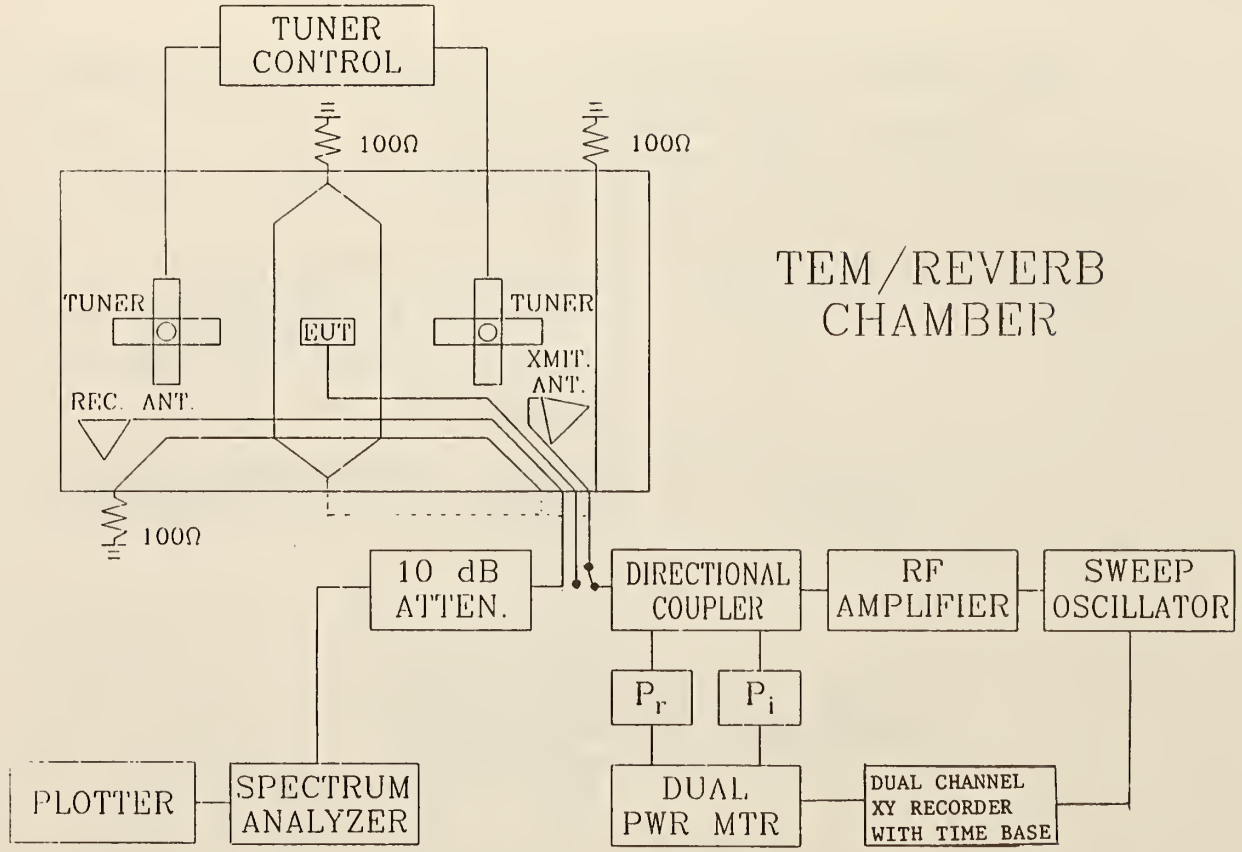

Figure 7.2 · Block diagram of swept frequency EM radiated emissions and shielding effectiveness system using TEM/reverberating chamber.

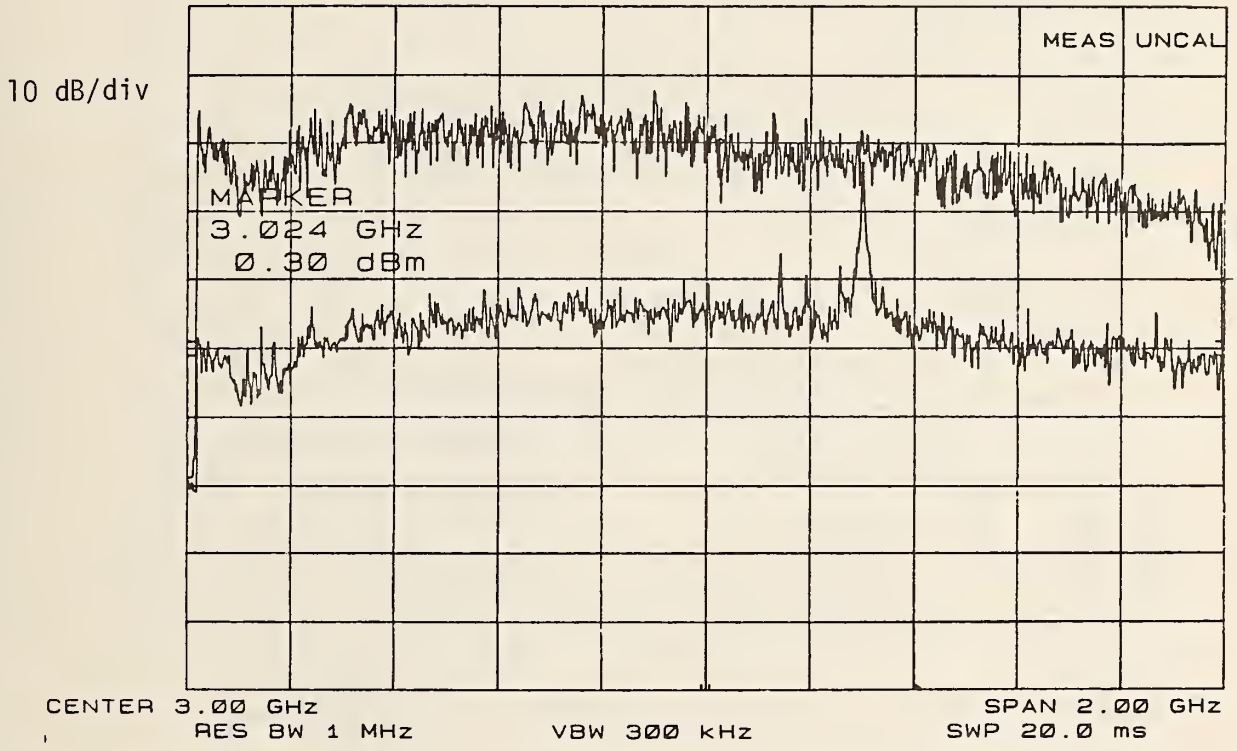

Figure 7.3 Measured SE data of 3 cm X 6 cm TEM cell with 15 mm circular aperture using the 1/10 scaled TEM/reverberating chamber and swept frequency measurement system.

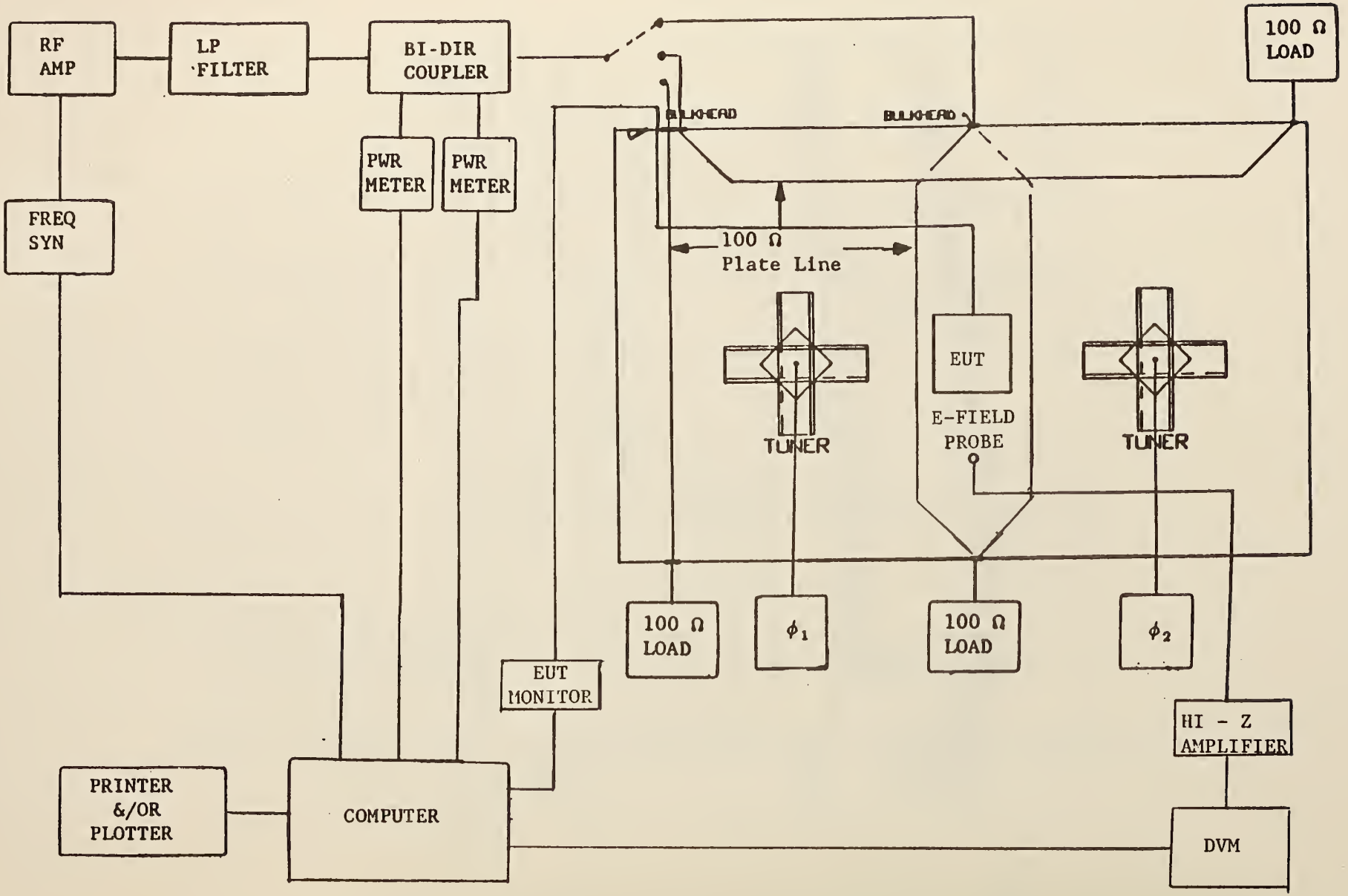

Figure 7.4 Block diagram of automated susceptibility measurement system using the TEM/reverberating chamber in the TEM mode of operation.

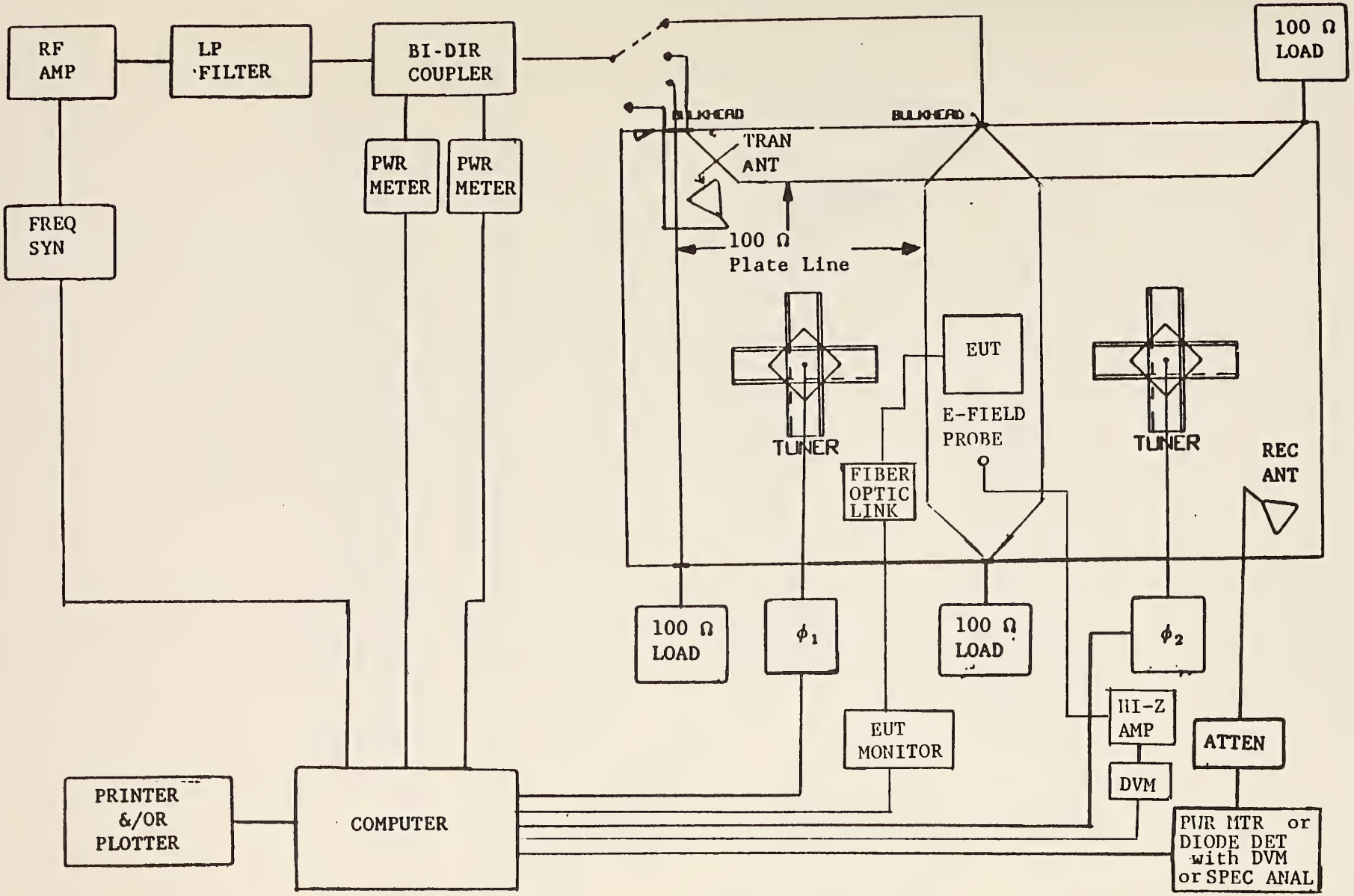

Figure 7.5 Block diagram of automated radiated susceptibility measurement system using the TEM/reverberating chamber in the transistion and the reverberating modes of operation.

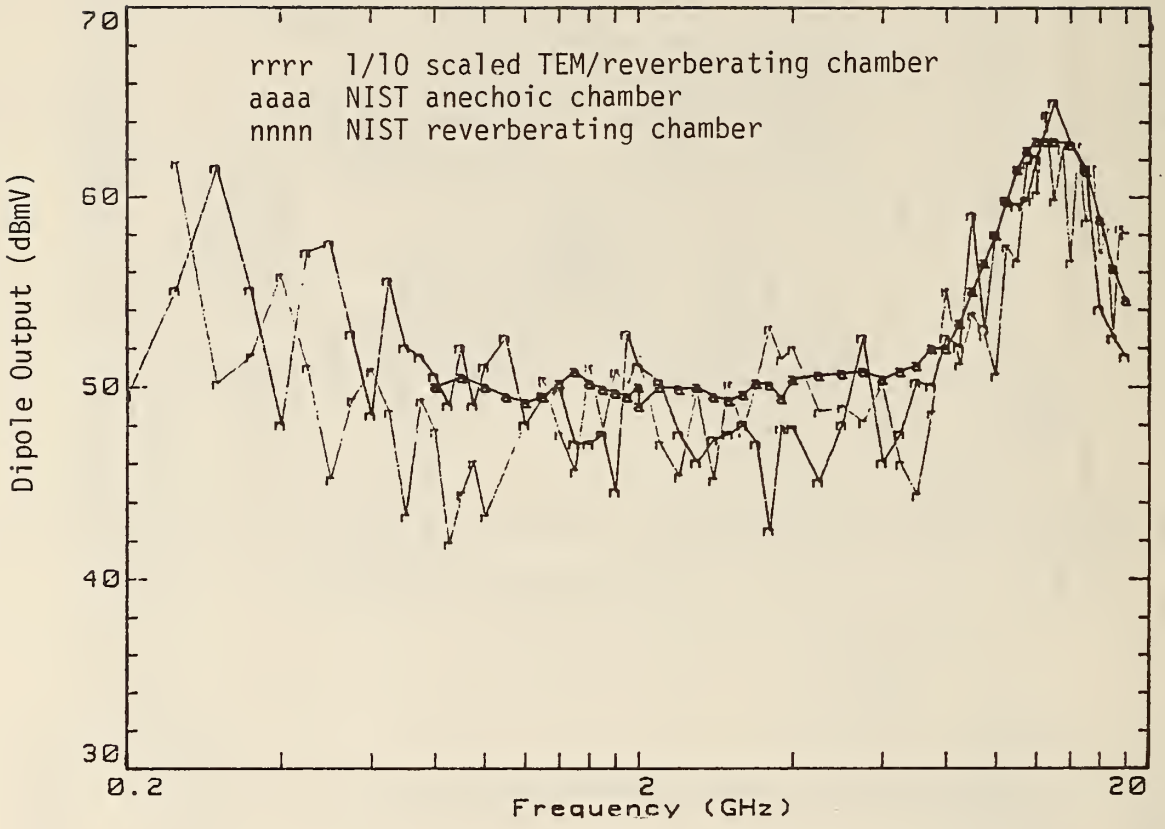

Figure 7.6 Maximum response of NIST 1 cm dipole probe to an E-field of 37 dBV/m generated in (a) the 1/10 scaled TEM/reverberating chamber, (b) NIST 2.74 m X 3.05 m X 4.57 m reverberating chamber, and (c) NIST 4.9 m X 6.7 m X 8.5 m anechoic chamber.

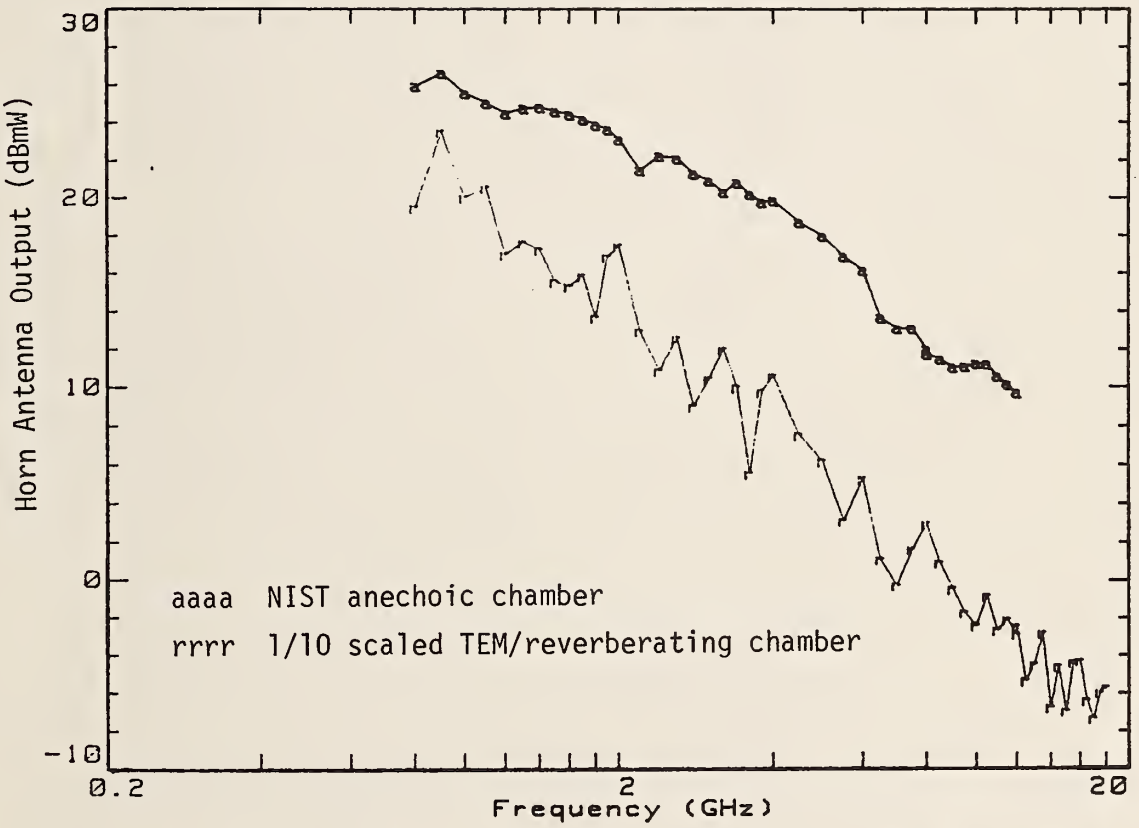

Figure 7.7 Maximum powers received by a broadband (1 to 18 GHz) horn antenna in an E-field of 37 dBV/m using: (a) 1/10 scaled TEM/reverberating chamber, and (b) NIST anechoic chamber.

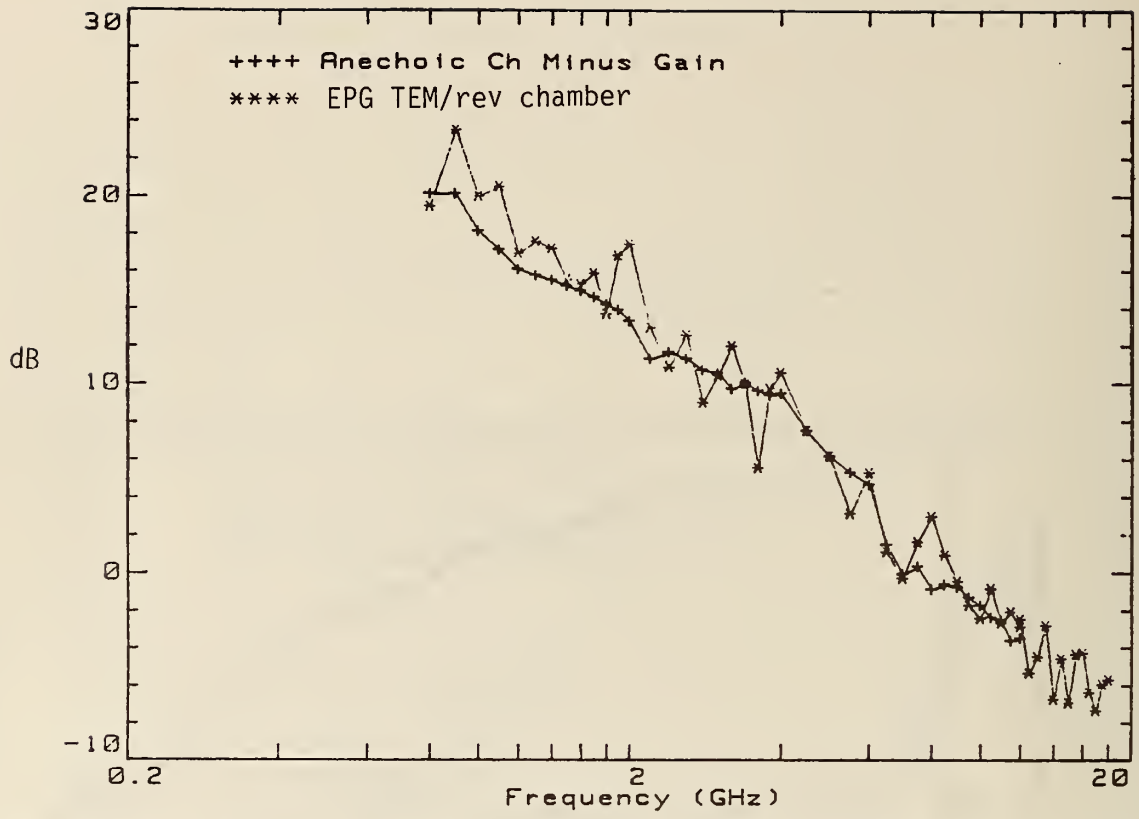

Figure 7.8 Comparison of broadband horn antenna response in 1/10 scaled TEM/reverberating chamber with its response minus free-space gain measured in the NIST anechoic chamber.

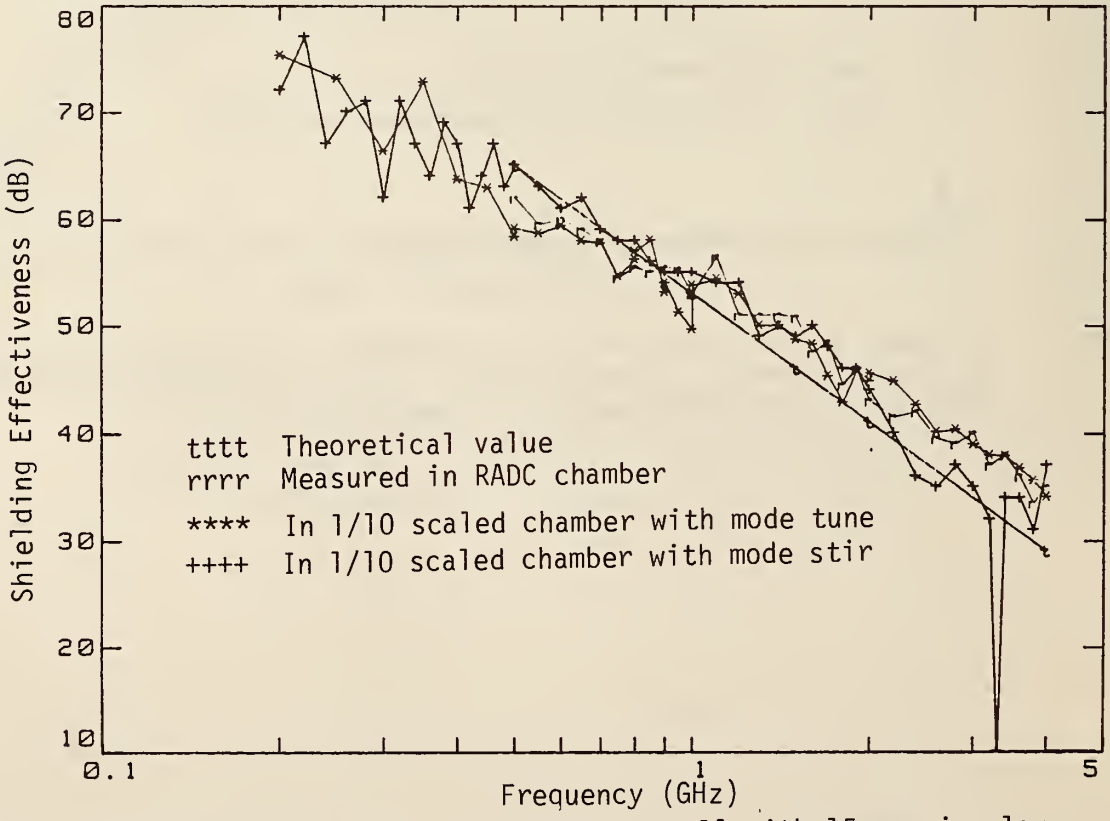

Figure 7.9 Comparison of SE of 3 cm X 6 cm TEM cell with 15 mm circular aperture: (a) theoretical calculations, (b) measured in RADC chamber, (c) measured in 1/10 scaled chamber with mode-tuned approach, and (d) measured in 1/10 scaled chamber with mode-stirred approach.

BL-114A
(5-90)

U.S. DEPARTMENT OF COMMERCE
NATIONAL INSTITUTE OF STANDARDS AND TECHNOLOGY

BIBLIOGRAPHIC DATA SHEET

1. PUBLICATION OR REPORT NUMBER
NIST/TN-1342

2. PERFORMING ORGANIZATION REPORT NUMBER

3. PUBLICATION DATE
July 1990

4. TITLE AND SUBTITLE

Measurement and Evaluation of a TEM/Reverberating Chamber

5. AUTHOR(S)

Myron L. Crawford, Mark T. Ma, John M. Ladbury, and Bill F. Riddle

6. PERFORMING ORGANIZATION (IF JOINT OR OTHER THAN NIST, SEE INSTRUCTIONS)

U.S. DEPARTMENT OF COMMERCE
NATIONAL INSTITUTE OF STANDARDS AND TECHNOLOGY
BOULDER, COLORADO 80303-3328

7. CONTRACT/GRANT NUMBER

8. TYPE OF REPORT AND PERIOD COVERED

9. SPONSORING ORGANIZATION NAME AND COMPLETE ADDRESS (STREET, CITY, STATE, ZIP)

Electromagnetic Environmental Effects Division
U.S. Army Electronic Proving Ground
Fort Huachuca, Arizona 85613-7110

10. SUPPLEMENTARY NOTES

11. ABSTRACT (A 200-WORD OR LESS FACTUAL SUMMARY OF MOST SIGNIFICANT INFORMATION. IF DOCUMENT INCLUDES A SIGNIFICANT BIBLIOGRAPHY OR LITERATURE SURVEY, MENTION IT HERE.)

This report summarizes the measurement and evaluation of a 1/10 scaled model TEM/reverberating chamber developed as a single, integrated facility for testing radiated electromagnetic compatibility/vulnerability (EMC/V) of large systems over the frequency range, 10 kHz to 40 GHz. The facility consists of a large shielded enclosure configured as a transverse electromagnetic (TEM), transmission line-driven, reverberating chamber. TEM mode test fields are generated at frequencies below multimode cutoff, and mode-stirred test fields are generated at frequencies above multimode cutoff. Both the chamber's cw and pulsed rf characteristics are measured and analyzed. The report also discusses the basis for such a development including the theoretical concepts, the advantages and limitations, the experimental approach for evaluating the operational parameters, and the procedures for using the chamber to perform EMC/V measurements. A full-scale chamber that will provide a test volume of 8 m x 16 m x 30 m is proposed. Some projections of the full-scale chamber's estimated characteristics and operational parameters are also given.

12. KEY WORDS (6 TO 12 ENTRIES; ALPHABETICAL ORDER; CAPITALIZE ONLY PROPER NAMES; AND SEPARATE KEY WORDS BY SEMICOLONS)

cw and pulsed rf testing; radiated EM compatibility and vulnerability measurements; reverberating chamber; TEM cell

13. AVAILABILITY

[X] UNLIMITED

[ ] FOR OFFICIAL DISTRIBUTION. DO NOT RELEASE TO NATIONAL TECHNICAL INFORMATION SERVICE (NTIS).

[X] ORDER FROM SUPERINTENDENT OF DOCUMENTS, U.S. GOVERNMENT PRINTING OFFICE, WASHINGTON, DC 20402.

[ ] ORDER FROM NATIONAL TECHNICAL INFORMATION SERVICE (NTIS), SPRINGFIELD, VA 22161.

14. NUMBER OF PRINTED PAGES
116

15. PRICE

ELECTRONIC FORM

NIST Technical Publications

Periodical

Journal of Research of the National Institute of Standards and Technology—Reports NIST research and development in those disciplines of the physical and engineering sciences in which the Institute is active. These include physics, chemistry, engineering, mathematics, and computer sciences. Papers cover a broad range of subjects, with major emphasis on measurement methodology and the basic technology underlying standardization. Also included from time to time are survey articles on topics closely related to the Institute's technical and scientific programs. Issued six times a year.

Nonperiodicals

Monographs—Major contributions to the technical literature on various subjects related to the Institute's scientific and technical activities.

Handbooks—Recommended codes of engineering and industrial practice (including safety codes) developed in cooperation with interested industries, professional organizations, and regulatory bodies.

Special Publications—Include proceedings of conferences sponsored by NIST, NIST annual reports, and other special publications appropriate to this grouping such as wall charts, pocket cards, and bibliographies.

Applied Mathematics Series—Mathematical tables, manuals, and studies of special interest to physicists, engineers, chemists, biologists, mathematicians, computer programmers, and others engaged in scientific and technical work.

National Standard Reference Data Series—Provides quantitative data on the physical and chemical properties of materials, compiled from the world's literature and critically evaluated. Developed under a worldwide program coordinated by NIST under the authority of the National Standard Data Act (Public Law 90-396). NOTE: The Journal of Physical and Chemical Reference Data (JPCRD) is published quarterly for NIST by the American Chemical Society (ACS) and the American Institute of Physics (AIP). Subscriptions, reprints, and supplements are available from ACS, 1155 Sixteenth St., NW., Washington, DC 20056.

Building Science Series—Disseminates technical information developed at the Institute on building materials, components, systems, and whole structures. The series presents research results, test methods, and performance criteria related to the structural and environmental functions and the durability and safety characteristics of building elements and systems.

Technical Notes—Studies or reports which are complete in themselves but restrictive in their treatment of a subject. Analogous to monographs but not so comprehensive in scope or definitive in treatment of the subject area. Often serve as a vehicle for final reports of work performed at NIST under the sponsorship of other government agencies.

Voluntary Product Standards—Developed under procedures published by the Department of Commerce in Part 10, Title 15, of the Code of Federal Regulations. The standards establish nationally recognized requirements for products, and provide all concerned interests with a basis for common understanding of the characteristics of the products. NIST administers this program as a supplement to the activities of the private sector standardizing organizations.

Consumer Information Series—Practical information, based on NIST research and experience, covering areas of interest to the consumer. Easily understandable language and illustrations provide useful background knowledge for shopping in today's technological marketplace.

Order the **above** *NIST publications from: Superintendent of Documents, Government Printing Office, Washington, DC 20402.*

Order the **following** *NIST publications—FIPS and NISTIRs—from the National Technical Information Service, Springfield, VA 22161.*

Federal Information Processing Standards Publications (FIPS PUB)—Publications in this series collectively constitute the Federal Information Processing Standards Register. The Register serves as the official source of information in the Federal Government regarding standards issued by NIST pursuant to the Federal Property and Administrative Services Act of 1949 as amended, Public Law 89-306 (79 Stat. 1127), and as implemented by Executive Order 11717 (38 FR 12315, dated May 11, 1973) and Part 6 of Title 15 CFR (Code of Federal Regulations).

NIST Interagency Reports (NISTIR)—A special series of interim or final reports on work performed by NIST for outside sponsors (both government and non-government). In general, initial distribution is handled by the sponsor; public distribution is by the National Technical Information Service, Springfield, VA 22161, in paper copy or microfiche form.

U.S. DEPARTMENT OF COMMERCE
National Institute of Standards and Technology
(formerly National Bureau of Standards)
325 Broadway
Boulder, Colorado 80303-3328

OFFICIAL BUSINESS
PENALTY FOR PRIVATE USE, $300